The Pennsylvania State University

The Graduate School

Department of Civil and Environmental Engineering

INTEGRATED MODELING OF MULTI-SCALE HYDRODYNAMICS, SEDIMENT AND POLLUTANT TRANSPORT

A Dissertation in

Civil Engineering

by

Shuangcai Li

Submitted in Partial Fulfillment
of the Requirements
for the Degree of

Doctor of Philosophy

December 2008

The thesis of Shuangcai Li was reviewed and approved* by the following:

Christopher J. Duffy
Professor of Civil Engineering
Dissertation Advisor
Chair of Committee

Xiantao Li
Assistant Professor of Mathematics

Patrick M. Reed
Associate Professor of Civil Engineering

Wen Shen
Assistant Professor of Mathematics

Rudy L. Slingerland
Professor of Geology

Thorsten Wagener
Assistant Professor of Civil Engineering

Peggy A. Johnson
Professor of Civil Engineering
Head of the Department of Civil and Environmental Engineering

*Signatures are on file in the Graduate School

ABSTRACT

Modeling hydrodynamics, sediment and pollutant transport over a wide range of spatial scales and hydrological events (e.g., inland flood and storm surges) remains a fundamental impediment to flood risk prediction, water resources management, and environmental protection. In addition, forecasting of extreme hydrologic events caused by severe weather and climate change [Milly et al., 2002] is a growing challenge. The goal of this study is to develop a modeling system appropriate to predict the multiple scale hydrodynamics, sediment and pollutant transport as well as extreme hydrological events for rivers, floodplains, coastal areas and their watersheds.

Two major contributions are made in this dissertation. First, a two-dimensional (2-D) finite volume model (PIHM-Hydro) was developed to fully couple the hydrodynamics, pollutant transport, and sediment transport at the scale of river, floodplain, and coastal area. This is the first 2-D high-order model to fully couple shallow water flow and sediment transport in the successful simulation of a real flow field. The model is based on standard upwind finite volume methods using Roe's and HLL approximate Riemann solvers on unstructured triangular grids. A multidimensional linear reconstruction technique and multidimensional slope limiter were implemented to achieve second-order spatial accuracy. Model efficiency and stability are treated using an explicit-implicit method for temporal discretization with operator splitting.

The advantages of the present model are that (1) it can handle complicated geometry by using the Delaunay triangulation based on Shewchuk's algorithm; (2) it is capable of producing accurate and stable solutions over a wide range of spatial scales and hydrological events such as discontinuous flow and wetting/drying process by using the approximate Riemann solver and the semi-implicit time integration technique based on the CVODE; and (3) it can accurately simulate the interactions of hydrodynamics, sediment transport and pollutant transport by fully coupling these processes physically and numerically. These advantages of PIHM-Hydro have been

illustrated by its successful application on the test cases where multiscale physical processes are dominant over a wide range of spatial scales.

The second contribution of this dissertation is to develop a spatially-distributed physically-based sediment transport modeling component at the watershed scale (PIHM-Sed) which is fully coupled with the hydrological processes within the Penn State Integrated Hydrologic Model system (PIHM) [Qu and Duffy, 2007]. This is the first spatially-distributed physically-based model to "fully-couple" hydrology and sediment transport in terms of physical and numerical coupling. It integrates the hillslope and channel processes, and is capable of predicting major surface/subsurface hydrological processes, sediment yield as well as spatial distribution of erosion/deposition. For the hillslope, the erosion processes of rain splash and sediment transport by overland flow are simulated; for the channel, it simulates the erosion of bed material and sediment transport by channel flow. An algorithm for bed armoring was also implemented in the channel component. In the model system, all hydrological and sediment transport processes are defined on discretized unit elements as a fully-coupled system of ordinary differential equations (ODEs) using a semi-discrete finite volume method (FVM) on unstructured grids. The implementation of the model has been performed on a hypothetical storm event at the Shale Hill watershed for demonstrating the capability of the model in multi-process simulation at watershed scale.

TABLE OF CONTENTS

LIST OF FIGURES

LIST OF TABLES

ACKNOWLEDGEMENTS

First and foremost, I would like to express my sincerest gratitude and appreciation to my advisor, Dr. Christopher J. Duffy for offering me this unique and invaluable opportunity to study at Penn State, for his financial support, constant encouragement, and insightful guidance. The door to Dr. Duffy's office has always been open whenever I need help from him. As his student, I feel extremely lucky to work with him and enjoy the pleasant academic environment he created for me in the past three and a half years. His inspiration and his warm personality have won my highest respect and love.

I would like to extend my gratitude to Dr. Patrick M. Reed and Dr. Thorsten Wagener for their consistent support and encouragement on this research as well as my future career. I am very thankful for Dr. Patrick M. Reed, Dr. Rudy L. Slingerland, and Dr. Thorsten Wagener for their invaluable time and constructive comments on the work contained here. I also want to thank Dr. Xiantao Li and Dr. Wen Shen for serving on my committee.

I would like to thank Dr. Yizhong Qu for building the foundation of this work and for his invaluable help. I am very appreciative for many friends at Penn State for their help, for the fun time we had together, and for the comfort you offered to me, especially Yuexiao Dong and Qing Zhu, Lei Zhang, Xiaoqiang Xiao, Yong Tang, Yaoling Bai, Zhenxing Zhang. In addition, I would like to thank Mukesh Kumar and Gopal Bhatt who has helped me a lot in this research. I also would like to thank all the colleagues in the hydrology group at Penn State for their support.

I am deeply indebted to my parents for giving me life, bringing me up, and giving me the best education they could.

Finally I want to express my deepest gratitude beyond words and dedicate this work to the most important person in my life, my wife, Lifang Luo for her love and support.

Chapter 1

INTRODUCTION

Near surface hydrologic processes, which occur within the water cycle of the lower atmosphere, land surface and subsurface zones, are of great significance to the natural environment and human life. In addition, hydrologically-driven sediment and pollutant transport processes, influencing the hydrodynamics directly and/or indirectly, are critical to water resources management, ecological environment, and engineering infrastructure, and fundamental to understanding the longer time scales of landscape evolution. Modeling these hydrologic processes and their interaction with the natural and human environment will continue to receive more attention given the potential for extreme hydrological events (floods and drought) caused by climate change [Milly et al., 2002].

At the scale of river, floodplain and coastal area, significant advances have been made in modeling hydrodynamics in recent years [e.g., Katopodes and Strelkoff, 1978; Molls and Chardhry, 1995; Hervouet and Petitjean, 1999; Alcrudo and Garcia-Navarro, 1993; Zhao et al., 1994; Anastasiou and Chan, 1997; Sleigh et al., 1998; Toro, 2001], sediment transport [Bennett and Nordin, 1977; Armanini and Di Silvio, 1988; Holly and Rahuel, 1990; Spasojevic and Holly, 1990; Capart and Young, 1998; Wu et al., 2000; Wu and Vieira, 2002; Cao et al., 2002; Fraccarollo and Capart, 2002; Wu, 2004; Wu et al., 2004;Cao et al., 2004;Wu and Wang, 2007], and pollutant transport [Aizinger et al., 2001;Aizinger and Dawson, 2002; Murillo et al., 2005;Benkhaldoun et al., 2007; Ebrahimiet al., 2007]. However, significant computational problems remain in predicting hydrodynamics, sediment and pollutant transport processes over a large range of spatial scales and for extreme events (e.g. drying/wetting, inland flooding, storm surge etc.). In particular, it requires special strategies for reliable solutions to (1) predict real flow fields with wetting/drying process, complex geometry and topography, (2) implement "full coupling" in multi-process simulation in order to faithfully represent the natural processes, and (3) solve very stiff system equations for the resulting fast and very slow processes, and where the model must work over wide range of spatial scales.

At the watershed scale, there has been considerable work modeling hydrologically-driven sediment transport [Horton, 1945; Bennett, 1974; Kirkby, 1978; Wischmeier and Smith, 1978; Beasley et al., 1980; Knisel, 1980; Ross et al, 1980; Park et al., 1982; Simons et al., 1982; Storm et al, 1987; Lane et al., 1988; Woolhiser et al., 1990; Gerits et al., 1990; Wicks and Bathurst, 1996; Morgan et al., 1998; Merritt et al., 2003; Heppner et al., 2005]. It seems clear that the next generation of models must represent hydrologic processes with better physical representations, coupling, and feedbacks before sediment transport codes will produce reasonable results. There have been very few existing physically-based models which can work at the full watershed scale considering both surface and subsurface flow. The effects of subsurface flow on erosion can be very important [Wicks and Bathurst, 1996; Heppner et al., 2006], but few models consider it. With advances in computing technology and deeper understanding in the physics of hydrology, new strategies to characterize hydrologic responses have been put forward, especially integrated hydrologic modeling [Abbot, 1986; VanderKwaak, 1999; Panday and Huyakorn, 2004; Qu and Duffy, 2007]. In the long term we make the assumption that coupling the sediment transport processes with integrated hydrologic models will be necessary to improve the performance of hydrodynamics and sediment transport modeling.

The objectives of this study are:

(1) To develop a fully-coupled model of multi-scale hydrodynamics, sediment transport, and pollutant transport at the scale of river, floodplain, and coastal area using upwind finite volume methods on unstructured grids, and to predict flood damage and

interactions between water flow and sediment/pollutant transport over a range of spatial scales.

(2) To develop a spatially-based physically-based sediment transport modeling component at the watershed scale which will be fully coupled with the hydrological processes in the PIHM system.

Corresponding to the two specific objectives, this dissertation consists of three research papers designated by chapters respectively. Chapter 2 is the first paper and presents a finite volume model (PIHM-Hydro) for micro- and meso-scale shallow water flow and sediment transport. Chapter 3 presents a coupled model of shallow water flow and pollutant transport on unstructured grids which is also a part of PIHM-Hydro. Chapter 4 presents an integrated model of hydrology and sediment transport at the watershed scale (PIHM-Sed).

References

[1] Abbott, M.B., J.A. Bathurst, P.E. and Cunge. 1986. An Introduction to the European Hydrological System-Systeme Hydrologicque Europeen "SHE" 2: Structure of a physically based distributed modeling system, Journal of Hydrology, 87, 61-77.

[2] Aizinger,V. and C. Dawson. 2002. A discontinuous Galerkin method for two-dimensional flow and transport in shallow water. Advances in Water Resources, 25: 67-84.

[3] Aizinger, V., C. Dawson, B. Cockburn, and P. Castillo. 2001. The local discontinuous Galerkin method for contaminant transport. Advances in Water Resources, 24: 73-87.

[4] Alcrudo,F. and P. Garcia-Navarro. 1993. A high-resolution Godunov-type scheme in finite volumes for the 2D shallow-water equations. International Journal for Numerical Methods in Fluids, 16 (6): 489-505.

[5] Anastasiou, K., and C. T. Chan. 1997. Solution of the 2D shallow water equations using the finite volume method on unstructured triangular meshes. International Journal for Numerical Methods in Fluids, 24: 1225-1245.

[6] Armanini, A., and Di Silvio, G. 1988. A one-dimensional model for the transport of a sediment mixture in non-equilibrium conditions. J. Hydraul. Res., 26 (3): 275–292.

[7] Benkhaldoun, F., I.Elmahi,and M.Seaid. 2007. Well-balanced finite volume schemes for pollutant transport by shallow water equations on unstructured meshes. Journal of Computational Physics, 226: 180-203.

[8] Beasley, D.B., Huggins, L.F., Monke E.J. 1980. ANSWERS: a model for watershed planning. Trans Am Soc Agric Eng, 23: 938–44.

[9] Bennett, J.P. 1974. Concepts of mathematical modeling of sediment yield. Water Resources Research, 10(3): 485-492.

[10] Bennett, J.P. and Nordin, C.F. 1977. Simulation of sediment transport and armouring. IAHS Hydrol. Sci. Bull., 22(4): 555-569.

[11] Cao, Z., Day, R., and Egashira, S. 2002. Coupled and decoupled numerical modeling of flow and morphological evolution in alluvial rivers. J. Hydraul. Eng., 128 (3): 306–321.

[12] Cao, Z., G. Pender, S. Wallis, and P. Carling. 2004. Computational dam-break hydraulics over erodible sediment bed. Journal of Hydraulic Engineering, 130 (7): 689-703.

[13] Capart, H. and D.L.Young. 1998. Formation of a jump by the dam-break wave over a granular bed. Journal of Fluid Mechanics, 372: 165-187.

[14] Ebrahimi, E., R.A. Falconer, B. Lin. 2007. Flow and solute fluxes in integrated wetland and coastal systems. EnvironmentalModelling& Software, 22: 1337-1348.

[15] Fraccarollo, L., H. CAPART, and Y. ZECH. 2003. A Godunov method for the computation of erosional shallow water transients.International Journal for Numerical Methods in Fluids, 41 (9): 951-976.

[16] Gerits, J..J.P, de Lima, J.L.M.P., van den Broek, T.M.W. 1990. Overland flow and erosion. In: Anderson, Burt, editors. Process studies in hillslope hydrology. Chichester, West Sussex, England: John Wiley and Sons Ltd.

[17] Heppner, C.S., Ran, Q., VanderKwaak, J.E., Loague, K. 2006. Adding sediment transport to the integrated hydrology model (InHM): Development and testing. Advances in Water Resources, 26: 930-943.

[18] Hervouet, J. M., and A. Petitijean. 1999. Malpasset dam-break revisited with two-dimensional computations. J. Hydraul. Res., 37 (6): 777-788.

[19] Holly, Jr., F. M., and Rahuel, J. L. 1990. New numerical/physical framework for mobile-bed modeling, Part I: Numerical and physical principles. J. Hydraul. Res., 28(4): 401–416.

[20] Horton, R. E. 1945. Erosional development of streams and their drainage basins: hydrophysical approach to quantitative morphology. Bull Geol Soc Am: 275–370.

[21] Katopodes, N. and T. Strelkoff. 1978. Computing two-dimensional dam-break flood waves. Journal of the Hydraulics Division, ASCE 104: 1269-1288.

[22] Kirkby, M. J. 1978. Implications for sediment transport. In: Kirkby, editor. Hillslope hydrology. Chichester, West Sussex, England: John Wiley and Sons Ltd.

[23] Knisel, W. G. 1980. CREAMS: a field scale model for chemicals, runoff and erosion from agricultural management systems. US Department of Agriculture, Conservation Research Report No. 26.

[24] Lane, L.J., Shirley, E.D., Singh, V.P. 1988. Modeling erosion on hillslopes. In: Anderson, editor. Modellinggeomorphological systems. Chichester, West Sussex, England: John Wiley and Sons Ltd.

[25] Merritt, W.S., Letcher, R.A., Jakeman, A.J. 2003. A review of erosion and sediment transport models. Environ Model Software;18: 761–99.

[26] Milly, P., R. Wetherald, K. Dunne, and T. Delworth. 2002. Increasing risk of great floods in a changing climate. Nature (London), 415: 514–517.

[27] Molls, T. and M.H. Chaudhry. 1995. Depth averaged open channel flow model. Journal of Hydraulic Engineering, 121: 453-465.

[28] Morgan, R.P.C., Quinton, J.N., Smith, R.E., Govers, G., Poesen, J.W.A., Auerswald, K., Chisci, G., Torri, D., Styczen, M.E. 1998.The European soil erosion model (EUROSEM): a process-based approach for predicting sediment transport from fields and small catchments. Earth Surface Processes and Landforms 23, 527–544.

[29] Murillo, J., J. Burguete, P. Brufau, abdP. García-Navarro. 2005. Coupling between shallow water and solute flow equations: analysis and management of source terms in 2D. International Journal for Numerical Methods in Fluids, 49 (3): 267-299.

[30] Panday, S., Huyakorn, P.S. 2004. A fully coupled physically-based spatially-distributed model for evaluating surface/subsurface flow. Advances in Water Resources 27, 361-382.

[31] Park, S.W., Mitchell, J.K. and Scarborough, J.N. 1982. Soil erosion simulation on small watersheds: a modified ANSWERS model. Trans. ASAE, 25: 1581-1588.

[32] Qu, Y., and C. J. Duffy. 2007. A semidiscrete finite volume formulation for multiprocess watershed simulation, Water Resources Research, 43, W08419, doi:10.1029/2006WR005752.

[33] Ross, B.B., Shanholtz, V.O. and Contractor, D.N., 1980. A spatially responsive hydrologic model to predict erosion and sediment transport. Water Resour. Bull., 16(3): 538-545.

[34] Simons, D.B., E.V. Richardson, and C.F. Nordin, 1965. Bedload equation for ripples and dunes, U.S. Geol. Surv. Prof. Pap. 462-H, 9 pp.

[35] Sleigh, P.A., M. Berzins, P.H. Gaskell and N.G. Wright. 1998. An unstructured finite-volume algorithm for predicting flow in rivers and estuaries. Computers and Fluids, 27 (4): 479-508.

[36] Spasojevic, M. and Holly Jr, M.. 1990. 2-D evolution in natural watercourses-new simulation approach. Journal of Waterway, Port, Coastal, and Ocean Engineering, 116(4): 425-433.

[37] Storm, B., Jorgensen, G.H. and Styczen, M. 1987. Simulation of water flow and soil erosion processes with a distributed physically-based modelling system. IAHS Publ. 167, pp. 595-608.

[38] Toro, E.F. 2001. Shock-capturing Methods for Free-surface Shallow Flows. John Wiley & Sons: Chichester.

[39] VanderKwaak, J., 1999. Numerical simulation of flow and chemical transport in integrated surface-subsurface hydrologic systems. Ph.D Thesis in Earth Sciences, University of Waterloo, Waterloo, Ontario, Canada, 217pp.

[40] Wicks, J.M. and Bathurst, J.C. 1996. SHESED: a physically based, distributed erosion and sediment yield component for the SHE hydrological modeling system. Journal of Hydrology, 175: 213-238.

[41] Wischmeier, W.H., Smith, D.D., 1978. Predicting Soil Erosion Losses: A Guide to Conservation Planning. USDA Agricultural Handbook No. 537, 58 pp.

[42] Woolhiser, D. A., Smith, R. E. and Goodrich, D. C. 1990. KINEROS: A kinematic runoff and erosion model: documentation and user manual, USDA Agricultural Research Service ARS-77.

[43] Wu, W. 2004. Depth-Averaged Two-Dimensional Numerical Modeling of Unsteady Flow and Nonuniform Sediment Transport in Open Channels. J. Hydraul. Eng., 130(10): 1013-1024.

[44] Wu, W., Rodi, W., and Wenka, T. 2000. 3-D numerical modeling of water flow and sediment transport in open channels. J. Hydraul. Eng., 126 (1): 4–15.

[45] Wu, W., and Vieira, D. A. 2002. One-dimensional channel network model CCHE1D 3.0—Technical manual. Technical Rep. No. NCCHE-TR-2002-1, National Center for Computational Hydroscience and Engineering, The Univ. of Mississippi, University, Miss.

[46] Wu, W., Vieira, D. A., Wang, S.S.Y. 2004. One-Dimensional Numerical Model for Nonuniform Sediment Transport under Unsteady Flows in Channel Networks. J. Hydraul. Eng., 130 (9): 914–923.

[47] Wu, W. and S.Wang. 2007. One-Dimensional Modeling of Dam-Break Flow over Movable Beds. Journal of Hydraulic Engineering, 133(1):48-58.

[48] Zhao, D. H. and H. W. Shen, G. Q. Tabios III, J. S. Lai, andW. Y. Tan. 1994. Finite-volume two-dimensional unsteady-flow model for river basins. Journal of Hydraulic Engineering: 120 (7): 863-883.

Chapter 2

A FINITE VOLUME MODEL FOR MULTI-SCALE SHALLOW WATER FLOW AND SEDIMENT TRANSPORT (PIHM-Hydro)

Abstract

In recent years significant advances have been made in modeling hydrodynamics and sediment transport in rivers, floodplains, and estuaries. For the case of rapidly varying flow and where it is necessary to simulate sediment transport processes over a large range of spatial scales, and for extreme events (dry bed to overbank floods to storm surge), significant computational problems remain. In particular, prediction of real flow fields with wetting/drying process, complex geometry and topography require special strategies for reliable solutions. To overcome this kind of problems this research incorporated a range of recent advances into a fully-coupled model of hydrodynamics, sediment transport, and morphological evolution in rivers and floodplains (PIHM-Hydro). The model is based on a standard upwind finite volume method using Roe's approximate Riemann solver on unstructured triangular grids. A multidimensional linear reconstruction technique and multidimensional slope limiter were implemented to achieve a second-order spatial accuracy. Model efficiency and stability were treated using an explicit-implicit method for temporal discretization with operator splitting. The model has been successfully applied to the hydrodynamics and/or sediment transport and morphological changes in rivers and floodplains including cases where multiscale physical processes are dominant.

Introduction

Water flow and sediment transport are simultaneous and interactive processes in rivers, flood plains, and coastal areas. The balance between these processes is influenced by both human activities and extreme natural events, resulting in aggradation and degradation in channels and harbors, deterioration of water quality and fisheries among other environmental effects and many other forms of ecological disturbance. One example is a dam removal or a flood event which initiates a dam break with rapid varying flow and sediment flushing. The disturbance is complex due to the uneven and changing bottom topography, irregular boundaries, rapid and strong erosion with abrupt bed and flow variations, and even more complicated and uncertain sediment transport mechanisms. These conditions cannot easily be simulated by a one-dimensional model. A two-dimensional model approach should be capable of handling complicated geometry, rapidly varying flow, and treating the processes in a fully-coupled mode is examined here.

The shallow water equations are typically used to represent the hydrodynamics of river floods, storm surges, tidal fluctuations, tsunami waves, forces acting on off-shore structures [Aizinger and Dawson, 2002].There are several challenges to numerical solutions to the shallow water equations in real field conditions with complex domains and irregular bed topography. A range of methods have been developed for solving the shallow water equations, such as method of characteristics [e.g., Katopodes and Strelkoff, 1978], finite difference method [e.g., Molls and Chardhry, 1995], finite element method [e.g., Hervouet, 2000], and finite volume method [e.g., Alcrudo and Garcia-Navarro, 1993; Zhao et al., 1994; Anastasiou and Chan, 1997; Sleigh et al., 1998; Toro, 2001; Bradford and Sanders, 2002; Valianiet al., 2002; Yoon and Kang, 2004; Begnudelli and Sanders, 2006]. Each method has its own limitations. For the method of characteristics, it is found that solutions cannot be found for certain cases of complex natural geometries. The finite difference method is widely used to solve shallow water equations, however, it may not guarantee strict conservation of mass and momentum, and structured (often regular) grids can be a poor representation for natural channels. In practice, the complex domain boundary makes domain decomposition a major issue [Sleigh et al., 1998]. Compared to structured grids, unstructured grids can easily adapt to the complex geometry in real flow fields and are flexible for changing the spatial resolution locally. The finite element method is used for unstructured grids, but it has been found to have problems when both subcritical and supercritical flows are encountered [Akanbi and Katopodes, 1988], and can produce solutions with local mass balance errors [Horrit, 2000]. In contrast, the finite volume method allows for the local and global mass conservation. It can also be applied to irregular domains and unstructured grids, and requires less memory for explicit calcuation [Loukili and Soulaimani, 2007]. There have been a few publications to solve the shallow water equations on unstructured grids using finite volume methods [Zhao et al., 1994; Anastasiou and Chan, 1997; Sleigh et al., 1998; Yoon and Kang, 2004]. No sediment transport, however, was considered in these models. Suspended sediment and bed elevation changes can significantly affect the dynamics of the flow [Capart and Young, 1998].The advantage of handling irregular flow geometries and the mass balance properties led the author to adopt the finite volume method in this research.

Mass conservation equations are used to describe the sediment transport and morphological evolution process. There are two approaches to coupled sediment routing and bed evolution i.e., non-capacity and capacity models (or customarily, non-equilibrium and equilibrium). The non-capacity models represent the sediment in a single mode as the total load. Compared to capacity models, non-capacity models treat entrainment and deposition as independent processes, the difference between which influences the sediment discharge and morphological evolution. The non-capacity models facilitate the numerical formulation since the empirical entrainment and deposition functions can be treated as source terms. Based on this discussion, the non-capacity model is adopted here.

Although there have been a large number of models for hydrodynamics and sediment transport, few of them are capable of predicting the rapid changing flow and the interactions between hydrodynamics and sediment transport over a wide range of spatial scales under extreme events such as heavy floods. Recently, several 1-D models were developed to simulate the dam break-induced sediment transport or high-concentration sediment transport as in hyper-concentrated flow and debris flow [Bellos and Hrissanthou, 1998; Fraccarollo et al., 2003; Cao et al., 2004; Ottevanger, 2005;Rosatti and Fraccarollo, 2006; Wu and Wang, 2007]. Hudson and Sweby [2003] and Castro Diaz et al. [2008] discussed 1-D bed load transport models coupled with shallow water equations by finite volume methods. Only a few studies were found in the 2-D case. Hudson and Sweby [2005] and Simpson and Castelltort [2006] extended the 1-D models of Hudson and Sweby [2003] and Cao et al. [2004] to 2-D on structured grids, although the models were not tested in lab experiments or real flow fields in the field. A major challenge of field applications is complex geometry and topography. Another challenge is the wetting/drying process which is common to most field applications. To the best of the authors' knowledge, the dynamics of sediment with the wetting/drying processes were rarely studied in the existing models.

The objective of this paper is to develop a multi-scale fully-coupled model of hydrodynamics, sediment transport, and morphological evolution of rivers and floodplain (PIHM-Hydro). The model is based on a cell-centered upwind finite volume method using Roe's approximate Riemann solver on unstructured triangular grids. A multidimensional linear reconstruction technique and multidimensional slope limiter [Jawahar and Kamath, 2000] are implemented to achieve a second-order spatial accuracy. In order to make the model efficient and stable, an explicit-implicit method is used in temporal discretization by an operator splitting technique, i.e., the advection part and non-stiff source terms are solved using an explicit scheme while the stiff source terms are handled by a fully implicit scheme. A number of test cases over a range of spatial scales and hydrological events are used to test the model and demonstrate the potential applications.

Methodology

Mathematical Formulation

The mathematical formulation in the model consists of the two-dimensional shallow water equations coupled with equations for sediment mass conservation and bed topography evolution (Figure 2-1). The 2-D shallow water equations are derived from the Navior-Stokes equations by assuming negligible velocity change and hydrostatic pressure distribution in vertical direction, and an incompressible fluid. The shallow water equations are appropriate to describe flow in vertically well-mixed water bodies where the horizontal length scales are much greater than the fluid depth. The shallow water equations in conservative form are written:

$$\frac{\partial(\rho h)}{\partial t}+\frac{\partial(\rho uh)}{\partial x}+\frac{\partial(\rho vh)}{\partial y}=-\frac{\partial(\rho_z z)}{\partial t}+\rho_w S_p \tag{1}$$

$$\frac{\partial(\rho uh)}{\partial t}+\frac{\partial\left(\rho\left(u^2h+\frac{gh^2}{2}\right)\right)}{\partial x}+\frac{\partial(\rho uvh)}{\partial y}=-\rho gh\left(S_{ox}+S_{fx}\right)+\rho f_c vh+\frac{\partial(hT_{xx})}{\partial x}+\frac{\partial(hT_{xy})}{\partial y}+F_x \tag{2}$$

$$\frac{\partial(\rho vh)}{\partial t}+\frac{\partial(\rho uvh)}{\partial x}+\frac{\partial\left(\rho\left(v^2h+\frac{gh^2}{2}\right)\right)}{\partial y}=-\rho gh\left(S_{oy}+S_{fy}\right)-\rho f_c uh+\frac{\partial(hT_{yx})}{\partial x}+\frac{\partial(hT_{yy})}{\partial y}+F_y \tag{3}$$

The conservation of suspended sediment in the water column is given by:

$$\frac{\partial(\psi h)}{\partial t}+\frac{\partial(\psi uh)}{\partial x}+\frac{\partial(\psi vh)}{\partial y}=E-D+S_s+\frac{\partial}{\partial x}\left(hD_x\frac{\partial\psi}{\partial x}\right)+\frac{\partial}{\partial y}\left(hD_y\frac{\partial\psi}{\partial y}\right) \tag{4}$$

The mass balance equation linking the local variation in bed level to the sediment removed or accumulated at the bottom is as follows:

$$(1-p)\frac{\partial z}{\partial t}=D-E \tag{5}$$

In Equations (1) – (5), t = time (T), x and y = horizontal coordinates (L), h = flow depth (L), u and v = depth-averaged flow velocity in x- and y-directions (L/T), z = bed elevation (L), ψ = flux-averaged volumetric sediment concentration (L^3/L^3), g = gravitational acceleration (L/T^2), p = bed sediment porosity, ρ_z = density of saturated bed, ρ = density of water-sediment mixture, S_{0x} and S_{0y}= bed slopes in x-and y-directions (L/L), S_{fx} and S_{fy} = friction slopes in x-and y-directions (L/L), S_p= the additional source/sink including precipitation, infiltration etc., S_s= the additional source/sink for the sediment , D and E = sediment deposition and entrainment fluxes between water flow and river bed (L/T), T_{xx}, T_{xy}, T_{yx}, and T_{yy} = depth-averaged turbulent stresses, D_x and D_y= turbulent diffusion coefficient of sediment particles(L^2/T), F_x and F_y = the additional forces arising from wind stress, tidal potential, atmospheric pressure etc., f_c = the coefficient of the Coriolis force resulting from the earth's rotation (1/T) which is calculated from:

$$f_c=2\Omega\sin\varpi \tag{6}$$

where Ω is the angular rotation rate of the Earth = π/12 radians/hour, and ω is the latitude. ρ and ρ_z = densities of water-sediment mixture and saturated bed respectively:

$$\rho=\rho_w(1-\psi)+\rho_s\psi \tag{7a}$$

$$\rho_z=\rho_w p+\rho_s(1-p) \tag{7b}$$

where ρ_w and ρ_s are densities of water and sediment respectively. In comparison to the effects of other processes in Equation (4), diffusion is normally negligible in sediment transport [Bennett, 1974]. Considering the scales of this model, turbulence effects, Coriolis force, and wind stress are also neglected in Equation (2) and (3).

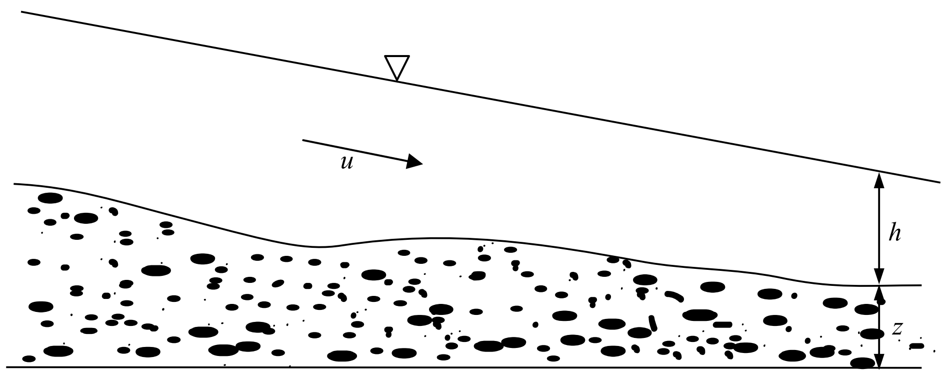

Figure **2-1**: Definition sketch for surface flow and sediment transport with dynamic bed topography. h is water depth, z is bed elevation, and u is flow velocity.

It is noted that Equations (1) – (3) differ from the single-phase clear-water flows because of the interaction between the water flow, sediment transport, and morphological change. Equation (1) describes the mass conservation for the water-sediment mixture. It differs from the traditional mass conservation equation for clear shallow water in the right-hand term which is used to account for the morphological change. It is also important to point out that the fluid density is not constant in Equations (1) – (3) considering that is important where fluvial processes from extreme events can initiate concentrated debris flow.

Following the approach of Cao et al. [2004] we manipulate the system of the equations (1) – (5) such that the mixture density disappears in the left hand side (now treated as a source term) and equations (1) – (3) become:

$$\frac{\partial h}{\partial t}+\frac{\partial(uh)}{\partial x}+\frac{\partial(vh)}{\partial y}=\frac{E-D}{1-p}+S_p \tag{1a}$$

$$\frac{\partial(uh)}{\partial t}+\frac{\partial\left(u^2h+gh^2/2\right)}{\partial x}+\frac{\partial(uvh)}{\partial y}=-gh\left(S_{ox}+S_{fx}\right)-\frac{(\rho_s-\rho_w)gh^2}{2\rho}\frac{\partial\psi}{\partial x}-\frac{(\rho_z-\rho)(E-D)u}{\rho(1-p)} \tag{2a}$$

$$\frac{\partial(vh)}{\partial t}+\frac{\partial(uvh)}{\partial x}+\frac{\partial\left(v^2h+gh^2/2\right)}{\partial y}=-gh\left(S_{oy}+S_{fy}\right)-\frac{(\rho_s-\rho_w)gh^2}{2\rho}\frac{\partial\psi}{\partial y}-\frac{(\rho_z-\rho)(E-D)v}{\rho(1-p)} \tag{3a}$$

In Equation (2a) and (3a), there are two additional source terms. The second and third terms on the right-hand side account for the spatial variations in sediment column concentration and the momentum transfer due to sediment exchange between the water and the erodible bottom boundary.

Auxiliary equations for bottom slope are given by $S_{0x}=\frac{\partial z}{\partial x}$ and $S_{0y}=\frac{\partial z}{\partial y}$. The friction slope is estimated by the Manning equation:

$$S_{fx}=\frac{n^2u\sqrt{u^2+v^2}}{h^{4/3}} \tag{8}$$

$$S_{fy}=\frac{n^2v\sqrt{u^2+v^2}}{h^{4/3}} \tag{9}$$

with n = Manning coefficient.

For the sediment flux, there exist an extensive literature of empirical formulae [e.g., Fagherazzi and Sun, 2003; Capart and Young, 1998; Cao et al., 2004; Wu and Wang, 2007]. A form which captures the empirical physics for entrainment and deposition in a minimum of parameters is proposed by the authors:

$$E=\alpha(\theta-\theta_c)h\sqrt{u^2+v^2} \tag{10}$$

$$D=\beta\omega\psi \tag{11}$$

where $\alpha =$ constant to be calibrated, $\theta = u_*^2 / sgd =$ Shields parameter, $\theta_c =$ critical Shields parameter for initiation of sediment movement, $\beta =$ parameter which depends on the distribution of the sediment in water column, $\omega =$ settling velocity of sediment particles in water, $u_* = \sqrt{gh}\sqrt{S_{fx}^2 + S_{fy}^2} =$ friction velocity, $d =$ sediment diameter, $\nu =$ kinematic viscosity of water, $s = \rho_s/\rho_w - 1$. In this paper, following Cao et al. [2004], β is set as

$$\beta = min[2, (1\text{-}p)/\psi]. \tag{12}$$

And ω is calculated using

$$\omega = \sqrt{\left(13.95\frac{\nu}{d}\right)^2 + 1.09gsd} - 13.95\frac{\nu}{d} \tag{13}$$

Domain Decomposition

Delaunay Triangulation [Delaunay, 1934; Voronoi, 1908] is applied to decompose the 2-D domain (Figure 2-2). A 2-D TIN (triangular irregular network) is formed over the model domain with constraints in order to incorporate domain boundaries, observation points, elevation contours or other features particular to the domain. Another advantage of conditional unstructured grid generation is the flexibility to handle multi-scale, multi-resolution, and/or nested modeling domains [Qu and Duffy, 2007]. Shewchuk [2001] has developed an algorithm for generating quality numerical grids, with constraints. This algorithm has been incorporated in PIHMgis [Bhatt et al., 2008] to facilitate the generation of unstructured meshes using GIS feature objects. In this research, PIHMgis is used to produce the unstructured grids for all the test cases in this paper.

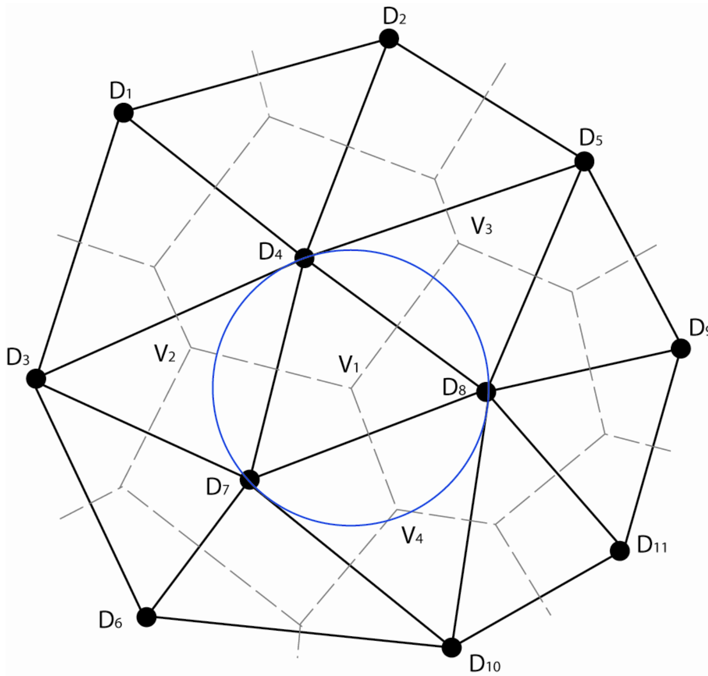

Figure **2-2**: Delaunay triangulation [Delanunay, 1934] and Voronoi diagram [Voronoi, 1908]. The solid lines form Delaunay triangulation, and the dashed lines form Voronoi diagram [Qu, 2004]. This approach is used to insure quality numerical grids.

Numerical Model

The system of equations (1a), (2a), (3a), (4) and (5) is hyperbolic and nonlinear and subject to discontinuities (shocks). Extending the one-dimensional formulation of transportational cyclic steps by Fagherazzi and Sun [2002], Equation (5) is rewritten as:

$$\frac{\partial \varphi}{\partial t} + \frac{\partial(\psi uh)}{\partial x} + \frac{\partial(\psi vh)}{\partial y} = 0 \qquad (5a)$$

with

$$\varphi = (1-p)z + \psi h \qquad (14)$$

The system can thus be reformulated as:

$$\frac{\partial \mathbf{U}}{\partial t} + \frac{\partial \mathbf{E}}{\partial x} + \frac{\partial \mathbf{G}}{\partial y} = \mathbf{S} \qquad (15)$$

where **U** is the vector of the conservative variables, **E** and **G** are the flux vectors in x- and y-direction, and **S** is the vector of source terms.

$$\mathbf{U}=\begin{pmatrix} h \\ uh \\ vh \\ \psi h \\ \varphi \end{pmatrix},\mathbf{E}=\begin{pmatrix} uh \\ u^2h+gh^2/2 \\ uvh \\ \psi uh \\ \psi uh \end{pmatrix},\ \mathbf{G}=\begin{pmatrix} vh \\ uv \\ v^2h+gh^2/2 \\ \psi vh \\ \psi vh \end{pmatrix},\ \mathbf{S}=\begin{pmatrix} (E-D)/(1-p)+S_p \\ S_x \\ S_y \\ D-E+S_s \\ 0 \end{pmatrix} \tag{16}$$

with

$$S_x=-gh\left(S_{ox}+S_{fx}\right)-\frac{(\rho_s-\rho_w)gh^2}{2\rho}\frac{\partial\psi}{\partial x}-\frac{(\rho_z-\rho)(E-D)u}{\rho(1-p)}+f_c vh \tag{17}$$

$$S_y=-gh\left(S_{oy}+S_{fy}\right)-\frac{(\rho_s-\rho_w)gh^2}{2\rho}\frac{\partial\psi}{\partial y}-\frac{(\rho_z-\rho)(E-D)v}{\rho(1-p)}-f_c uh \tag{18}$$

The source term vector is split into five parts: bed slope $\mathbf{S_0}$, friction slope $\mathbf{S_f}$, sediment concentration variations $\mathbf{S_c}$, sediment exchange $\mathbf{S_e}$, and the additional source/sink term $\mathbf{S_p}$ respectively:

$$\mathbf{S_0}=\begin{pmatrix} 0 & -ghS_{0x} & -ghS_{0y} & 0 & 0 \end{pmatrix}^T$$

$$\mathbf{S_f}=\begin{pmatrix} 0 & -ghS_{fx} & -ghS_{fy} & 0 & 0 \end{pmatrix}^T$$

$$\mathbf{S_c}=\begin{pmatrix} 0 & -\frac{(\rho_s-\rho_w)gh^2}{2\rho}\frac{\partial\psi}{\partial x} & -\frac{(\rho_s-\rho_w)gh^2}{2\rho}\frac{\partial\psi}{\partial y} & 0 & 0 \end{pmatrix}^T$$

$$\mathbf{S_e}=\begin{pmatrix} \frac{E_S}{1-p} & -\frac{(\rho_z-\rho)(E-D)u}{\rho(1-p)} & -\frac{(\rho_z-\rho)(E-D)v}{\rho(1-p)} & E-D & 0 \end{pmatrix}^T$$

$$\mathbf{S_p}=\begin{pmatrix} S_p & f_c vh & -f_c uh & S_s & 0 \end{pmatrix}^T$$

It is now convenient to write the system as:

$$\frac{\partial\mathbf{U}}{\partial t}+\nabla\cdot\mathbf{F}=\mathbf{S} \tag{19}$$

with $\mathbf{F} = (\mathbf{E},\ \mathbf{G})^T$. The system can be integrated over an arbitrary control volume V_i:

$$\int_{V_i} \frac{\partial \mathbf{U}}{\partial t} dV + \int_{V_i} \nabla \cdot \mathbf{F} dV = \int_{V_i} \mathbf{S} dV \tag{20}$$

and applying the Gauss theorem, the second integral on the left-hand side is replaced by a line integral around the control volume, which changes Equation (19) into:

$$\int_{V_i} \frac{\partial \mathbf{U}}{\partial t} dV + \oint_{\Gamma_i} \mathbf{F} \cdot \mathbf{n} d\Gamma = \int_{V_i} \mathbf{S} dV \tag{21}$$

where Γ =boundary of the control volume and $\mathbf{n} = (n_x\ n_y)^T$ = the unit outward vector normal to the boundary.

A cell-centered finite volume method is formulated for Equation (21) over a Delaunay-type triangle-shaped control volume, where the dependent variables of the system are stored at the center of the control volume and represented as piecewise constant. The association of these variables with the centers enables the implementation of a high-order interpolation scheme [Sleigh et al., 1998]. Using the mid-point rule to Equation (20), it can be rewritten as:

$$\frac{\partial \mathbf{U}_i}{\partial t} = -\frac{1}{V_i} \sum_{j=1}^{3} (\mathbf{F}_{ij} \cdot \mathbf{n}_{ij}) \Gamma_j + \mathbf{S}_i \tag{22}$$

with $\mathbf{U}_i$ being the average values over the control volume V_i, $\mathbf{S}_i = \frac{1}{V_i} \int_{V_i} \mathbf{S} dV$ being the numerical approximation of the source term, $\mathbf{n}_{ij}$ being the unit outward normal vector to the edge j, and $\mathbf{F}_{ij}$ is the numerical flux vector through the edge j, which is calculated using an approximate Riemann solver.

To evaluate the flux using approximate Riemann solver, the Jacobian of the normal flux ($\mathbf{F} \cdot \mathbf{n}$) is calculated:

$$\mathbf{J}_n = \begin{pmatrix} 0 & n_x & n_y & 0 & 0 \\ \left(c^2 - u^2\right)n_x - uvn_y & 2un_x + vn_y & un_y & 0 & 0 \\ -uvn_x + \left(c^2 - v^2\right)n_y & vn_x & un_x + 2vn_y & 0 & 0 \\ -\left(un_x + vn_y\right)\psi & \psi n_x & \psi n_y & un_x + vn_y & 0 \\ -\left(un_x + vn_y\right)\psi & \psi n_x & \psi n_y & un_x + vn_y & 0 \end{pmatrix} \tag{23}$$

where $\mathbf{J}_n = \dfrac{\partial(\mathbf{F} \cdot \mathbf{n})}{\partial \mathbf{U}} = \dfrac{\partial(\mathbf{E})}{\partial \mathbf{U}} n_x + \dfrac{\partial(\mathbf{G})}{\partial \mathbf{U}} n_y$. Its eigenvalues are:

$$\lambda_1 = un_x + vn_y + c\,,\ \lambda_2 = un_x + vn_y\,,\ \lambda_3 = un_x + vn_y - c\,,\ \lambda_4 = un_x + vn_y\,,\ \lambda_5 = 0 \tag{24}$$

with $c = \sqrt{gh}$ being the celerity of small amplitude gravitational waves. The corresponding eigenvectors are:

$$\mathbf{e}_1 = \begin{pmatrix} 1 \\ u + n_x c \\ v + n_y c \\ c \\ c \end{pmatrix},\ \mathbf{e}_2 = \begin{pmatrix} 0 \\ -n_y \\ n_x \\ 0 \\ 0 \end{pmatrix},\ \mathbf{e}_3 = \begin{pmatrix} 1 \\ u - n_x c \\ v - n_y c \\ c \\ c \end{pmatrix},\ \mathbf{e}_4 = \begin{pmatrix} 0 \\ 0 \\ 0 \\ 1 \\ 1 \end{pmatrix},\ \mathbf{e}_5 = \begin{pmatrix} 0 \\ 0 \\ 0 \\ 0 \\ 1 \end{pmatrix} \tag{25}$$

This hyperbolic system is degenerate since one eigenvalue is zero. The system consists of two shocks, two rarefaction waves, or a shock plus a rarefaction wave in addition to a contact discontinuity. The contact discontinuity is produced based on the assumption of negligible flow turbulence and sediment diffusion. For more detailed analysis, see Toro [2001] or Fagherazzi and Sun [2003].

There are many formulations for the numerical flux on the solution of a Riemann problem at the boundary of two elements [Toro, 2001]. Most of them proved satisfactory, but the Roe's formulation was consistently more stable, producing solutions at extreme conditions where others fail [Sleigh et al, 1997], and it is more flexible, working for quite a few hyperbolic systems.

The Roe's method is a Godunov scheme. The numerical flux is calculated as

$$\mathbf{F}_n = \frac{1}{2}\left(\mathbf{F}(\mathbf{U}_L)\cdot\mathbf{n} + \mathbf{F}(\mathbf{U}_R)\cdot\mathbf{n} - \left|\widetilde{\mathbf{J}}_n\right|(\mathbf{U}_R - \mathbf{U}_L)\right) \tag{26}$$

where $\mathbf{U}_L$ and $\mathbf{U}_R$ are the left and right conserved variables, $\widetilde{\mathbf{J}}_n$ is the modified Jacobian of the similar form as $\mathbf{J}_n$ and must meet the following requirements [Roe, 1981]:

(1) $\widetilde{\mathbf{J}}_n$ depends on the left and right states;

(2) $\widetilde{\mathbf{J}}_n$ is diagonalizable with real eigenvalues and a set of eigenvectors;

(3) $(\mathbf{F}\cdot\mathbf{n})_R - (\mathbf{F}\cdot\mathbf{n})_L = \widetilde{\mathbf{J}}_n(\mathbf{U}_R - \mathbf{U}_L)$;

(4) $\widetilde{\mathbf{J}}_n \to \mathbf{J}_n(\widetilde{\mathbf{U}})$ as $\mathbf{U}_L, \mathbf{U}_R \to \widetilde{\mathbf{U}}$.

$\widetilde{\mathbf{J}}_n$ can be evaluated as $\widetilde{\mathbf{J}}_n = \mathbf{J}_n(\widetilde{\mathbf{U}})$ with $\widetilde{\mathbf{U}}$ being some average values based on the left and right states. A change of variable approach is used to find the Jacobian matrix meeting the requirement [Roe, 1981; Leveque, 2002]. The detailed derivation is given in the supplement. It is noted that the bottom elevation is always continuous at the shock and contact discontinuity locations according to the Rankine-Hugoniot conditions [Fagherazzi and Sun, 2003]. The intermediate states are calculated as:

$$\widetilde{h} = \frac{h_L + h_R}{2},\ \widetilde{u} = \frac{u_L\sqrt{h_L} + u_R\sqrt{h_R}}{\sqrt{h_L} + \sqrt{h_R}},\ \widetilde{v} = \frac{v_L\sqrt{h_L} + v_R\sqrt{h_R}}{\sqrt{h_L} + \sqrt{h_R}},\ \widetilde{\psi} = \frac{\psi_L\sqrt{h_L} + \psi_R\sqrt{h_R}}{\sqrt{h_L} + \sqrt{h_R}} \tag{27}$$

The eigenvalues of $\widetilde{\mathbf{J}}_n$ are

$$\widetilde{\lambda}_1 = \widetilde{u}n_x + \widetilde{v}n_y + \widetilde{c}\,,\ \widetilde{\lambda}_2 = \widetilde{u}n_x + \widetilde{v}n_y,\ \widetilde{\lambda}_3 = \widetilde{u}n_x + \widetilde{v}n_y - \widetilde{c}\,,\ \widetilde{\lambda}_4 = \widetilde{u}n_x + \widetilde{v}n_y,\ \widetilde{\lambda}_5 = 0 \tag{28}$$

with $\widetilde{c} = \sqrt{g\widetilde{h}}$ and the corresponding eigenvectors

$$\tilde{\mathbf{e}}_1 = \begin{pmatrix} 1 \\ \tilde{u} + n_x \tilde{c} \\ \tilde{v} + n_y \tilde{c} \\ \tilde{\psi} \\ \tilde{\psi} \end{pmatrix}, \quad \tilde{\mathbf{e}}_2 = \begin{pmatrix} 0 \\ -n_y \\ n_x \\ 0 \\ 0 \end{pmatrix}, \quad \tilde{\mathbf{e}}_3 = \begin{pmatrix} 1 \\ \tilde{u} - n_x \tilde{c} \\ \tilde{v} - n_y \tilde{c} \\ \tilde{\psi} \\ \tilde{\psi} \end{pmatrix}, \quad \tilde{\mathbf{e}}_4 = \begin{pmatrix} 0 \\ 0 \\ 0 \\ 1 \\ 1 \end{pmatrix}, \quad \tilde{\mathbf{e}}_5 = \begin{pmatrix} 0 \\ 0 \\ 0 \\ 0 \\ 1 \end{pmatrix} \tag{29}$$

The difference in the left and right conserved variables can be expressed as the Jacobian eigenvectors as

$$d\mathbf{U} = \mathbf{U}_R - \mathbf{U}_L = \sum_{k=1}^{5} \alpha_k \tilde{\mathbf{e}}_k \tag{30}$$

with

$$\begin{aligned}
\alpha_1 &= \frac{(h_R - h_L)}{2} + \frac{\left(\left((hu)_R - (hu)_L\right)n_x + \left((hv)_R - (hv)_L\right)n_y - (h_R - h_L)(\tilde{u} n_x + \tilde{v} n_y)\right)}{2\tilde{c}} \\
\alpha_2 &= \left((hv)_R - (hv)_L - (h_R - h_L)\tilde{v}\right)n_x - \left((hu)_R - (hu)_L - (h_R - h_L)\tilde{u}\right)n_y \\
\alpha_3 &= \frac{(h_R - h_L)}{2} - \frac{\left(\left((hu)_R - (hu)_L\right)n_x + \left((hv)_R - (hv)_L\right)n_y - (h_R - h_L)(\tilde{u} n_x + \tilde{v} n_y)\right)}{2\tilde{c}} \\
\alpha_4 &= (h\psi)_R - (h\psi)_L - (h_R - h_L)\tilde{\psi} \\
\alpha_5 &= (\varphi_R - \varphi_L) - \left((h\psi)_R - (h\psi)_L\right)
\end{aligned} \tag{31}$$

Therefore $\left|\tilde{\mathbf{J}}_n\right|(\mathbf{U}_R - \mathbf{U}_L) = \sum_{k=1}^{5} \left|\tilde{\lambda}_k\right| \alpha_k \tilde{\mathbf{e}}_k$ and the numerical flux is calculated as:

$$\mathbf{F}_n = \frac{1}{2}\left(\mathbf{F}(\mathbf{U}_L) \cdot \mathbf{n} + \mathbf{F}(\mathbf{U}_R) \cdot \mathbf{n} - \sum_{k=1}^{5} \left|\tilde{\lambda}_k\right| \alpha_k \tilde{\mathbf{e}}_k \right) \tag{32}$$

To avoid entropy violation at the sonic point or the critical flow condition, the fix proposed by Harten and Hyman [1983] is incorporated

$$\left|\tilde{\lambda}_k\right| = \begin{cases} \left|\tilde{\lambda}_k\right| & \text{if } \left|\tilde{\lambda}_k\right| \geq \delta \\ \delta & \text{if } \left|\tilde{\lambda}_k\right| < \delta \end{cases} \tag{33}$$

Delis et al. [2000] suggest the following formula for δ

$$\delta = \max\left(0, \tilde{\lambda}_k - (\lambda_k)_L, (\lambda_k)_R - \tilde{\lambda}_k\right) \tag{34}$$

Linear Reconstruction

To preserve a high spatial accuracy in the flow simulation, a second order or higher piecewise linear reconstruction is necessary. Many second-order numerical schemes have been implemented in shallow water equations on unstructured triangular grids [e.g., Anastasiou and Chan, 1997; Sleigh et al., 1998; Hubbard, 1999; Wang and Liu, 2000; Yoon and Kang, 2004] and other types of grids [e,g., Alcrudo and Garcia-Navarro, 1993; Ambrosi, 1995; Valiani et al., 2002; Caleffi et al., 2003]. Extension of structured techniques, such as the MUSCL approach, to unstructured grids have achieved only partial success due to the pronounced grid sensitivity [Jawahar and Kamath, 2000] and therefore poor results are obtained on highly distorted grids. The reconstruction techniques proposed by Jawahar and Kamath [2000] has been successfully applied with HLL approximate Riemann solve in shallow water equation [Yoon and Kang, 2004]. Compared to other multidimensional linear reconstruction techniques, it uses a wide computational stencil and does not strongly depend on vertex values. This reconstruction technique is adopted here.

For a given cell with center *i*, the values of a variable can be calculated

$$U(x, y) = U_i + \nabla U_i \cdot \mathbf{r} \tag{35}$$

where **r** is the vector extending from the cell center *i* to any point (*x, y*) within the cell, U_i is the cell-averaged values stored at the centroid, and ∇U_i is the cell-centered gradient which is described as below.

Applying the Green-Gauss theorem, the gradient based on a certain closed path, say the boundary of the cell *i*, can be calculated as

$$\nabla U_i = \frac{1}{A_i} \oint_{\Gamma} U\mathbf{n} d\Gamma \tag{36}$$

where Γ is the boundary of the cell, and A_i is the area.

The stencil used to calculate the gradient is shown in Figure 2-3. The first step is to calculate the gradients for two triangles on either side of an edge. For example, the two triangles Δ1a2 and Δ12i for edge j = 1. The above-described method is used to calculate $(\nabla U)_{1a2}$ and $(\nabla U)_{12i}$. The next step is to obtain the face gradient using the area-weighted average of these two gradients.

$$(\nabla U)_1 = \frac{A_{1a2}(\nabla U)_{1a2} + A_{12i}(\nabla U)_{12i}}{A_{1a2} + A_{12i}} \tag{37}$$

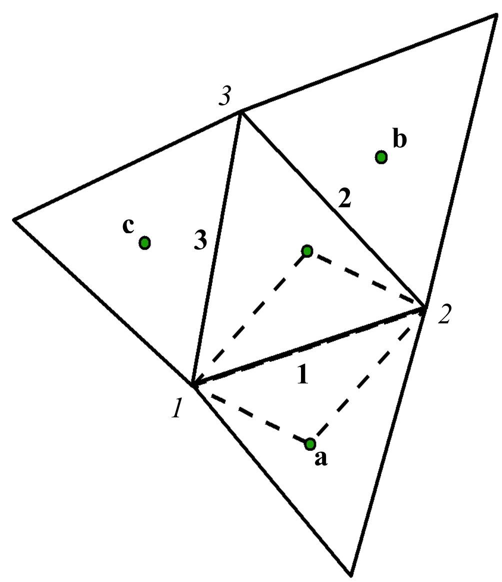

Figure **2-3**: The stencil used to calculate the gradients of the state variables.

The same approach can be used to compute the face gradients $(\nabla U)_2$ and $(\nabla U)_3$ at edges j= 2 and 3 respectively. Finally the gradient for the cell is then constructed using the area-weighted average of the three face gradients as follows

$$\nabla U_i = \frac{A_{1a2i}\left(\nabla U\right)_1 + A_{2b3i}\left(\nabla U\right)_2 + A_{3c1i}\left(\nabla U\right)_3}{A_{1a2i} + A_{2b3i} + A_{3c1i}} \tag{38}$$

It is noted that the values of the conserved variables at the vertexes are needed in the first step. A pseudo-Laplacian procedure is used to obtain the vertex values from the corresponding centroid values to assure second-order accuracy [Frink, 1994], as proposed by Holmes and Connell [1989].

Multidimensional Slope Limiter

High order schemes may lead to a nonphysical oscillatory solution near discontinuities without suitable adjustment [Toro, 1999]. Therefore, it is necessary to limit the solution slope during the linear reconstruction in order to avoid oscillations. The multidimensional slope limiter proposed by Jawahar and Kamath [2000] has the advantages that: (1) the limiter is inherently multidimensional in construction which fits unstructured grids, and (2) it is continuously differentiable. Based on these properties, it is adopted in the paper. The limited gradient is constructed as follows:

$$\nabla U_i^L = \omega_a \nabla U_a + \omega_b \nabla U_b + \omega_c \nabla U_c \tag{39}$$

where ∇U_i^L is the limited gradient for cell *i*, and ω_a, ω_b, ω_c are the weights given by the multidimensional limiter function. ∇U_a, ∇U_b, and ∇U_c are the unlimited gradient for three neighboring triangles. The three weights are computed as:

$$\omega_a = \frac{g_b g_c + \varepsilon^2}{g_a^2 + g_b^2 + g_c^2 + 3\varepsilon^2}$$

$$\omega_b = \frac{g_c g_a + \varepsilon^2}{g_a^2 + g_b^2 + g_c^2 + 3\varepsilon^2} \tag{40}$$

$$\omega_c = \frac{g_b g_a + \varepsilon^2}{g_a^2 + g_b^2 + g_c^2 + 3\varepsilon^2}$$

where $g_a = \|\nabla U_a\|_2^2$, $g_b = \|\nabla U_b\|_2^2$, $g_c = \|\nabla U_c\|_2^2$ and $\varepsilon << 1$ prevents zero in the denominator.

Source Terms

It is of great importance to correctly treat the source terms in (18). Friction slope $\mathbf{S_f}$ and sediment exchange $\mathbf{S_e}$ can be discretized in a point-wise manner, say, evaluated at the centroid. The sediment concentration $\mathbf{S_c}$ terms are also discretized at the centroid, and the linear reconstruction procedure readily provides the sediment concentration (*ψ)* spatial gradients:

$$\nabla \psi_i = \frac{\nabla(h\psi)_i - \psi\nabla h_i}{h} \tag{41}$$

For discretization of the bed slope term, a surface gradient method is used, where the water surface elevation (*H*=*h*+*z*) instead of the water depth (*h*) is reconstructed. The water depth values at left and right sides of an edge are calculated by subtracting the corresponding bed elevation from water surface elevation. This can prevent the strong depth fluctuations due to the arbitrary bed geometry [Farshi and Komaei, 2004].

Time Integration

In order to reduce the numerical instabilities related to the friction slope and the sediment exchange for shallow depths, a semi-implicit method is used. The system (Eqs (1) – (5)) is split into two ordinary differential equations:

$$\frac{\partial \mathbf{U}_i}{\partial t} = -\frac{1}{V_i}\sum_{j=1}^{3}\left(\mathbf{F}_{ij} \cdot \mathbf{n}_{ij}\right)\Gamma_j + \mathbf{S}_{\mathbf{0}i} + \mathbf{S}_{\mathbf{c}i} + \mathbf{S}_{pi} \tag{43}$$

$$\frac{\partial \mathbf{U}_i}{\partial t} = \mathbf{S}_{\mathbf{f}i} + \mathbf{S}_{\mathbf{e}i} \tag{44}$$

In the first step, advection (48) with source terms for bed slope and sediment concentration is solved by an explicit method. Next, the values obtained from the first step define initial conditions for (49) and the system is solved using an implicit method (BDF). Here we use the advanced ODE solver CVODE [Hindmarsh and Serban, 2005].

The explicit time integration is performed by the first-order Euler method, or a total variation diminishing (TVD) Runge-Kutta method [Shu and Osher, 1988] which have been shown to improve stability and have high-order accuracy (third):

$$\begin{aligned} \mathbf{U}_1 &= \mathbf{U}^n + \Delta t \mathrm{f}\left(\mathbf{U}^n\right) \\ \mathbf{U}_2 &= \frac{3}{4}\mathbf{U}^n + \frac{1}{4}\mathbf{U}_1 + \frac{1}{4}\Delta t \mathrm{f}\left(\mathbf{U}_1\right) \\ \mathbf{U}^{n+1} &= \frac{1}{3}\mathbf{U}^n + \frac{1}{3}\mathbf{U}_2 + \frac{2}{3}\Delta t \mathrm{f}\left(\mathbf{U}_2\right) \end{aligned} \tag{45}$$

where f is the right hand side of Equation (49).

It is well known that the explicit scheme has a stability restriction on the Courant–Friedrichs-Lewy (CFL) condition. An adaptive Δt is used in the model according to the following formula:

$$\Delta t \le \frac{\min\left(d_i\right)}{2\max\left(\left(\sqrt{u^2 + v^2} + c\right)_i\right)} \tag{46}$$

Where i is the cell index, and d_i represents the whole set of distances between the ith centroid and those of its neighboring cells.

Boundary Conditions

Open and solid wall boundary conditions have been implemented. The (slip) solid wall boundary condition is given by:

$$\begin{pmatrix} h_* \\ \mathbf{u}_* \cdot \mathbf{n} \\ \mathbf{u}_* \cdot \mathbf{t} \\ \psi_* \\ z_* \end{pmatrix} = \begin{pmatrix} h_L \\ -\mathbf{u_L} \cdot \mathbf{n} \\ \mathbf{u_L} \cdot \mathbf{t} \\ \psi_L \\ z_L \end{pmatrix} \tag{47}$$

where **u** denotes $(u, v)^T$, and the subscripts L and * are the variables at the left side and boundary respectively. From Equation (47), the velocity components can be calculated

$$\begin{pmatrix} u_* \\ v_* \end{pmatrix} = \begin{pmatrix} n_x & -n_y \\ n_y & n_x \end{pmatrix} \begin{pmatrix} \mathbf{u}_L \cdot \mathbf{n} \\ \mathbf{u}_L \cdot \mathbf{t} \end{pmatrix} \tag{48}$$

The open boundary conditions are more complicated. A simple one is the free outfall condition, where the waves pass the boundary without reflection. It can be describes as $\mathbf{U}_* = \mathbf{U}_L$. For other cases, sometimes the physical boundary condition(s) is not enough for the model, therefore is combined with equations obtained from theory of characteristics to derive sufficient information at the boundaries.

A flow chart shown in Figure 2-4 is used to illustrate the numerical algorithm.

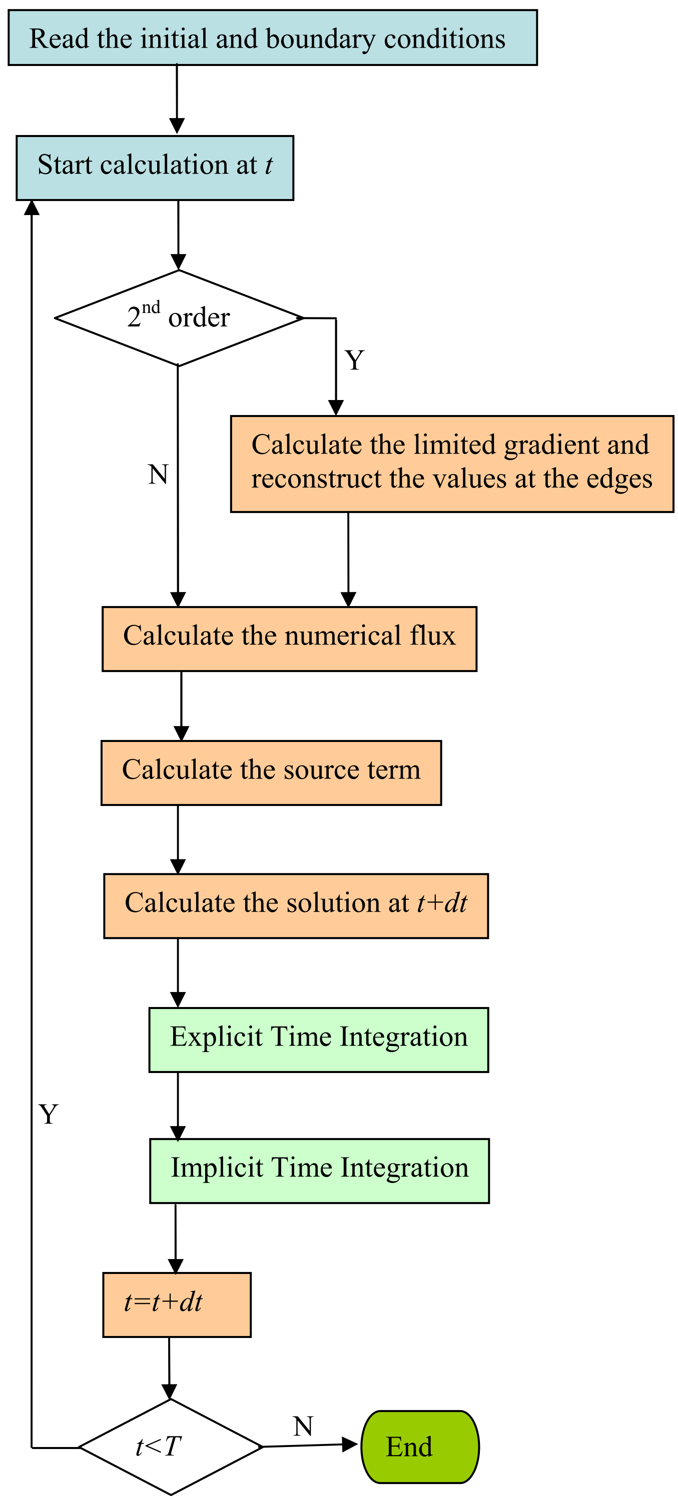

Figure **2-4**: Flow chart for the numerical algorithm of PIHM-Hydro.

Results and Discussion

In order to demonstrate the accuracy and flexibility of PIHM-Hydro, a number of test cases over a range of spatial scales are examined. The first three examples are used to test the capability of the model to predict microscale hydrodynamics and sediment transport, while the other two examples are used to study the performance of the model in mesoscale applications.

Small-scale applications

A 2-D microscale dam-break with dry-wet and converging-diverging channel

This experiment is used to test the capability of PIHM-Hydro to predict flow dynamics in an irregular flow domain, an initially dry bed, with non-zero bed slope and roughness. Bellos et al. [1992] performed several simulations of an instantaneous dam failure and a range of initial conditions. The 21.2 m long by 1.4 m wide experimental flume had a rectangular, converging-diverging cross-section as shown in Figure 2-5. A movable gate (x=0 m) was used to simulate the instantaneous dam break. Eight probes were installed along the center line of the channel to measure the flow depths. More details can be found in Bellos et al. [1992].

The initial water level is 0.15 m upstream of the dam and zero downstream of the dam with the bed slope of 0.002. The solid wall boundary condition was applied at the upstream end and side walls, and a free out-fall condition was applied at the downstream boundary. The domain was discretized into 3,886 triangles (Figure 2-5). The Nash-Sutcliffe model efficiency coefficient (NSE) [Nash and Sutcliffe, 1970] was used to quantitatively evaluate the predictive accuracy of the model:

$$NSE = \frac{\sum_{t=1}^{N}\left(q_o - q_p\right)}{\sum_{t=1}^{N}\left(q_o - \tilde{q}_o\right)} \qquad [49]$$

where q_o and q_p are the observed and predicted values respectively. $\tilde{q}_o$ denote the observed mean value, and N is the total number of time steps. The data from t=0 to 60 seconds were used in the calculation of NSEs. Table 2-1 shows the predictions with n = 0.010 are the best especially downstream of the dam. Therefore n = 0.010 was used. The predicted and measured flow depths at the different positions are shown in Figure 2-6.

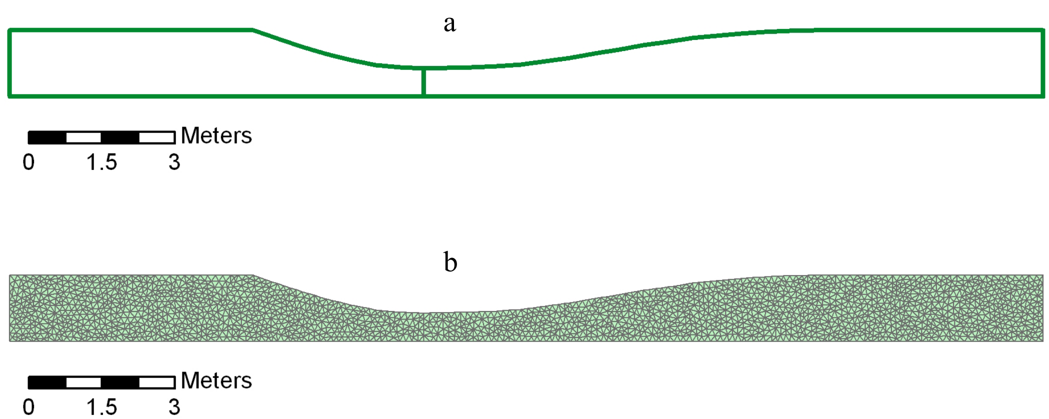

Figure **2-5**: Plan view (a) and computational mesh (b) of the converging-diverging channel in Bellos et al. [1992] experiment.

Table **2-1**: NSEs (Nash-Sutcliffe model efficiency coefficient) for different Manning's n at the Bellos experiment.

n	-8.5 m	-4.0 m	-0.0 m	+5.0 m	+10.0 m
0.009	0.99	0.999	0.968	0.68	0.83
0.01	**0.99**	**0.999**	**0.96**	**0.77**	**0.91**
0.011	0.99	0.998	0.95	0.70	0.84
0.012	0.99	0.997	0.93	0.52	0.82
0.013	0.98	0.996	0.91	0.17	0.75
0.014	0.98	0.99	0.89	-0.34	0.64

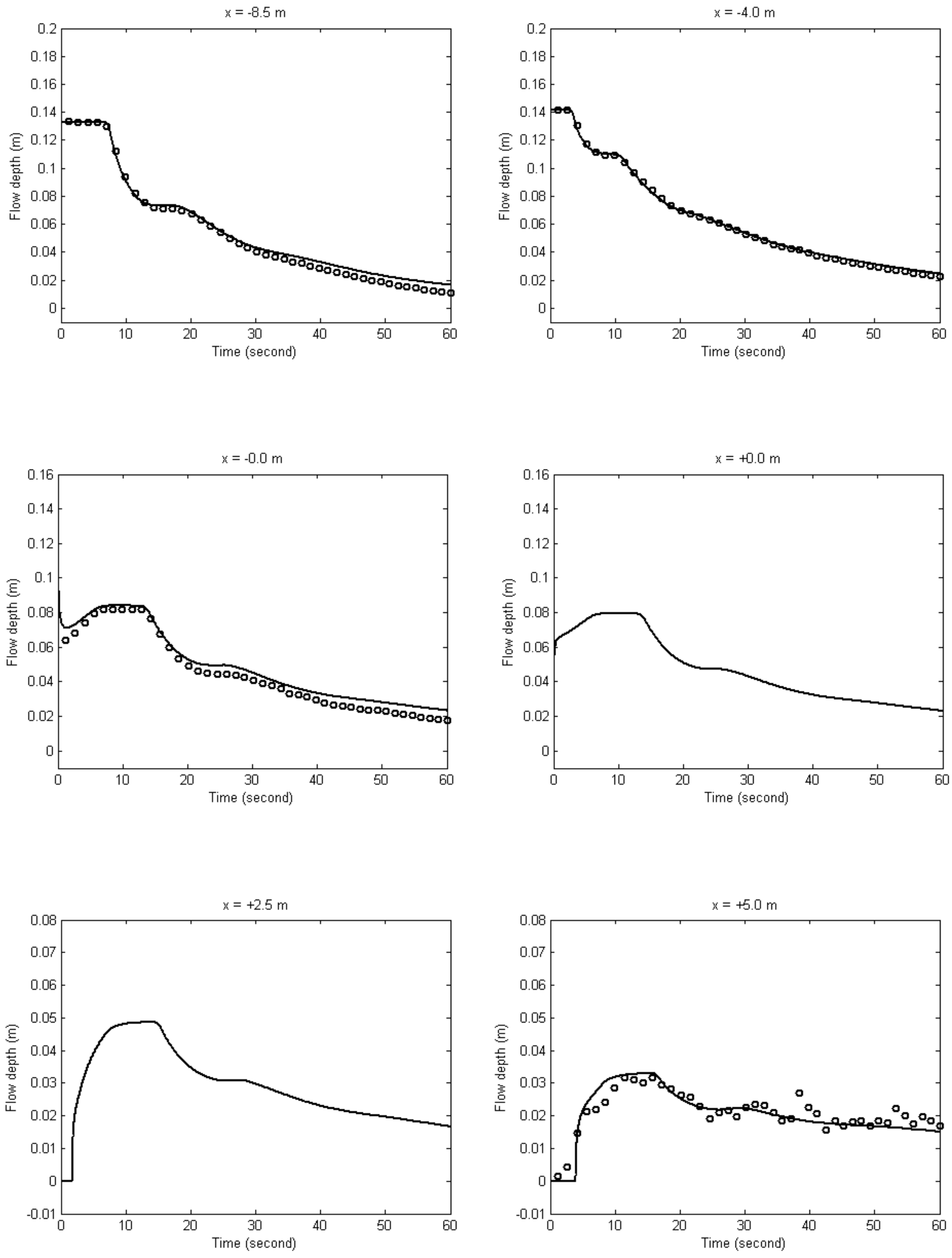
x = -8.5 m
x = -4.0 m
x = -0.0 m
x = +0.0 m
x = +2.5 m
x = +5.0 m
Flow depth (m)
Time (second)

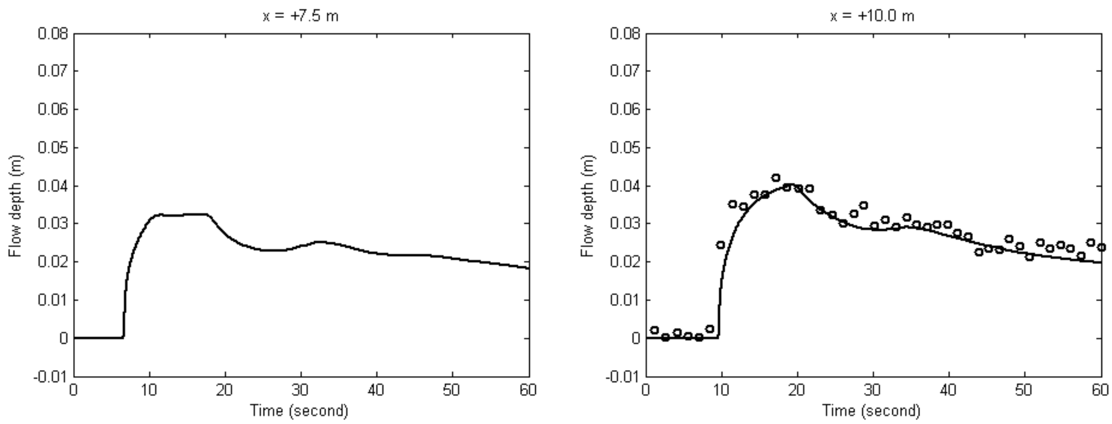

Figure **2-6**: 2-D microscale dam-break with dry-wet and converging-diverging channel: measured (circle) and predicted (solid line) temporal variations of flow depth at different locations as indicated, i.e., upstream of the dam, at the dam, and downstream of the dam.

Upstream of the dam the predictions match the measurement very well with NSEs larger than 0.96. Even at the downstream locations characterized by the critical to supercritical flow and the wetting process, the flow depths are well reproduced. However, the predictions are not as good as upstream of the dam. In addition, Table 2-1 displays that the downstream locations especially at x = +5.0 m are very sensitive to the Manning's roughness coefficient. That is due to the depth averaging the model neglects the vertical velocity information which is important in the transition from subcritical to supercritical flow [Martin and Gorelick, 2005]. Additionally, a close look at Figure 2-6 reveals that the arrival times of the wave front are also accurately predicted. Overall, PIHM-Hydro is accurate and stable to simulate the wetting/drying process and the supercritical flow.

2D Rainfall-runoff wetting/drying numerical experiment

A rainfall and runoff example [diGiammarco, 1996] is adapted here to test the capability of PIHM-Hydro in simulating the rainfall-driven surface flow with intensive wetting/drying processes. In this example, the surface flow from a tilted V-shape catchment (Figure 2-7) is generated by one 90-minute duration, 10.8 mm/hr intensity rainfall event. The catchment is composed of two 100 meters by 800 meters planes connected to a 1000 m-long and 20 m-wide channels. In this test case the channel depth is set to 0 which means the planes and channel are smoothly connected so that the backwater effect can be considered. The bed slopes are 0.05 and 0.02, perpendicular to and parallel to the channel respectively. Manning roughness coefficients are 0.015 for the plane and 0.15 for the channel. The simulation was run for 180 minutes with free fall boundary condition at the channel outlet and no flow boundary conditions elsewhere. Initially the water depth is zero over the entire domain. Only half of the domain was simulated and the discharge was multiplied by two to obtain the one for the entire domain thanks to symmetry.

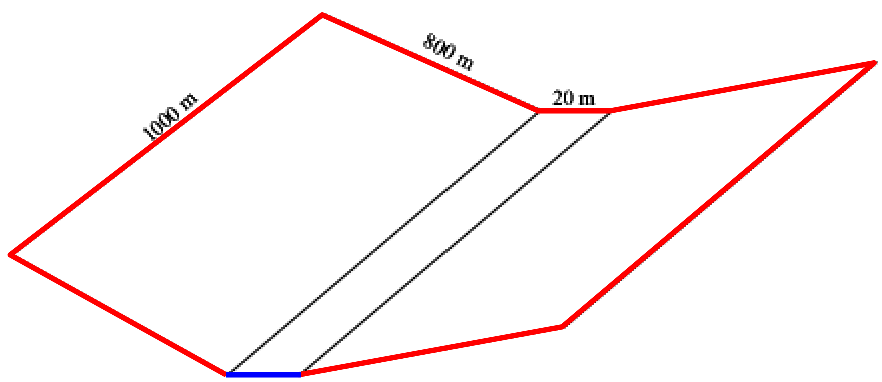

Figure **2-7**: 2D Rainfall-runoff dry to wet numerical experiment: tilted V-shape catchment (not to scale). The red lines represent the no-flow boundaries. The blue line denotes the channel outlet, where the free outfall boundary is applied. The black lines are for the interfaces between planes and the channel.

The relatively steep slope in this test case is expected to produce close results for this model and the kinematic or diffusive wave approximations [Tayfur et al., 1993]. So the simulation on the decomposed domain of 740 triangles was compared with those from IFD (integrated finite difference) [diGiammarco, 1996], MIKE-SHE [Abbot et al., 1986], IHM

[VanderKwaak, 1999], and MODHMS [Panday and Huyakorn, 2004] which use kinematic or diffusive approximations. In these models, IFD, MIKE-SHE, and MODHMS weakly couple the 2-D flow on the plane with the 1-D flow in the channel while IHM fully couples the 2-D flows on the plane and in the channel. The hydrograph predicted by PIHM-Hydro is first compared with the multi-model average in Figure 2-8 (a). The multi-model average is derived from weighted averaging of all model outputs. Here we assume the weight is the same for each model. PIHM-Hydro is also compared individually with IFD, MIKE-SHE, IHM, and MODHMS in Figure 2-8 (a). The simulation data from these models were obtained by digitalizing the figures from the publications.

Excellent agreement is illustrated between PIHM-Hydro and the multi-model average (NSE = 0.996) as well as the other models, especially for the peak discharge and receding limb. Although there is a slight discrepancy in the rising limb for these models, the times to peak discharge are almost equal. According to Figure 2-8 (a), PIHM-Hydro predicts a constant and stable plateau of the peak discharge (4.86 m^3/s), which is analytically correct and shows this model is very stable. Among these simulations, PIHM-Hydro has the best agreement with IHM (NSE = 0.999) as compared to MODHMS (NSE = 0.991), MIKE-SHE (NSE = 0.982), and IFD (NSE = 0.990). This might be expected since only PIHM-Hydro and IHM fully couple the 2-D overland and channel flow to consider the backwater effect. Figure 2-8 (b) shows the accumulative mass balance errors calculated using the equation:

$$err_h = \frac{(precipitaion - discharge - storage)}{precipitaion} \quad [50]$$

The mass balance error is very small with the maximum value less than 0.8% at t=45 minutes and almost zero at t=180 minutes. For this benchmark test case, the results indicate that PIHM-Hydro is very stable, robust and mass-conservative for cases of rainfall-driven overland-channel flow with intensive wetting/drying processes.

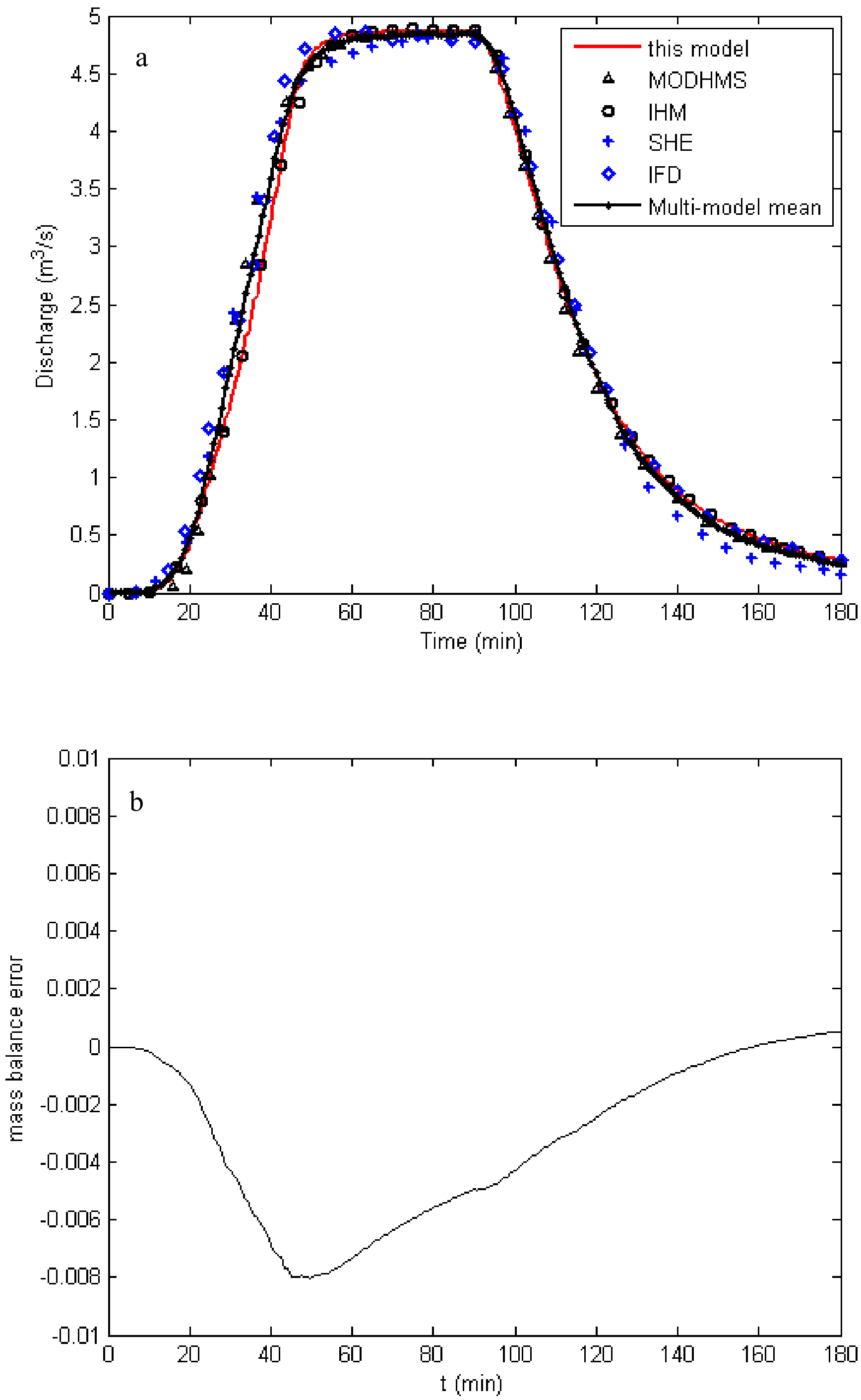

Figure **2-8**: Evaluation of model performance for the 2D rainfall-runoff dry to wet numerical experiment: (a) Comparison of simulated hydrograph with the ones modeled by MODHMS [Panday and Huyakorn, 2004], IHM [VanderKwaak, 1999], MIKE-SHE [Abbot et al., 1986], and IFD [diGiammarco et al., 1996]; (b) mass balance errors.

2D Microscale flow and sediment transport following dam break

To demonstrate the ability to predict the flow dynamics with fully coupled sediment transport, PIHM-Hydro is applied to two microscale dam break experiments with flow over movable beds, the Taipei experiment [Capart and Young, 1998] and the Louvain experiment [Fraccarollo and Capart, 2002]. In the Taipei experiment, artificial spherical pearls of uniform size were used as the sediment particles with diameter of 6.1 mm, specific gravity of 1.048, and settling velocity in water of 7.6 cm/s. In the Louvain experiment, the sediment particles were replaced by cylindrical PVC pellets with equivalent spherical diameter of 3.5 mm, specific gravity of 1.54, and settling velocity in water of 18 cm/s. Horizontal prismatic flumes were used in both experiments. The test reach was 1.2 m long, 70 cm high, and 20 cm wide for the Taipei experiment, and 2.5 m long, 25 cm high, and 10 cm wide for the Louvain experiment. The sluice gates were place in the middle of flumes in both test cases to represent the idealized dam break. The initial water depth was 10 cm upstream and 0 cm downstream for both experiments.

The 2D model was used in the numerical simulation of both cases. The computational meshes are shown in Figure 2-9, with 745 and 764 triangles for the Taipei and Louvain experiments respectively. In this model, several parameters need to be determined. The sediment porosity (p) and Manning's roughness coefficient (n) were obtained from the publications [Wu and Wang, 2007]. p the was given as 0.28 and 0.3 for the Taipei and Louvain experiments respectively while n was set as 0.025 for both experiments. For the parameters α and θ_c, calibration was done to obtain the best values. In this study, the measured data at $5t_0$ and $3t_0$ (t_0 = 0.101s) were used in the Taipei and Louvain experiments respectively to calibrate these two parameters which were then used to predict the flow and sediment dynamics in the other two times. α and θ_c were calibrated to 2.2 and 0.15 for the Taipei case, and 5.0 and 0.05 for the Louvain case.

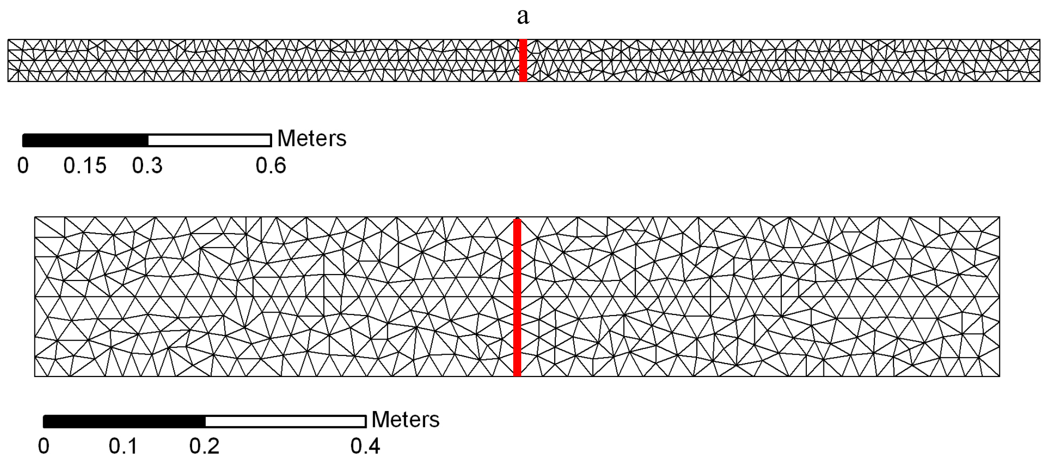

Figure **2-9**: Computational mesh of the Louvain experiment (a) and the Taipei experiment (b). The red lines denote the dams.

In Figures 2-10 and 2-11, the predicted water (*H*) and bed (*z*) surface elevations along the center line of the channel are compared with the measured ones. Table 2-2 lists the NSEs of the water (NSE_H) and bed (NSE_z) surface elevations for the two experiments. In the Louvain experiment, the measured data at $5t_0$ were used to calibrate the model ($NSE_H = 0.99$ and $NSE_z = 0.73$). The results show the model reproduced the flow dynamics over movable beds very well ($NSE_H >= 0.96$ and $NSE_z >= 0.56$). Although the prediction of bed surface elevations is not as good as the water surface, it can be considered satisfactory considering the complexity of the bed evolution, the small time scale, the small magnitude of the bed elevation change, and the measurement uncertainty. According to Figure 2-10, the model accurately predicted the wave front locations and the erosion magnitude in this experiment. The hydraulic jump was formed near the initial dam sites due to rapid bed erosion. In the Louvain experiment, the locations of the hydraulic jump were well predicted by PIHM-Hydro. It can be observed from both the predictions and measurements that the hydraulic jump propagated upstream in Louvain experiment.

In the Taipei experiment, the measured data at $3t_0$ were used to calibrate the model ($NSE_H = 0.7$ and $NSE_z = 0.3$). It is evident that the calibration is not as good as that in the Louvain experiment. By using the calibrated parameters, Figure 2-11 shows PIHM-Hydro predicted the wave front locations and the erosion magnitude very well. However, Figure 2-11 and Table 2-2 shows the agreement between the prediction and measurement was not as good with respect to the magnitude and the locations of the hydraulic jump. The hydraulic jump moved upstream in the prediction but remains stationary in the experiment. This might be partly due to the very light bed material with large diameter used in this experiment, which is very different from the bed materials in natural rivers. Further lab experiment need to be done to examine this phenomenon.

The mass balance errors of sediment transport are also calculated to evaluate the model using the following equation:

$$err_z = \frac{\sum_i (\Delta z)_i \cdot A_i \cdot (1-p) + \sum_i \Delta(hc)_i \cdot A_i}{\sum_i (\Delta z)_i \cdot A_i} \qquad [51]$$

where $(\Delta z)_i$ and $\Delta(hc)_i$ are the change of bed elevation and sediment load per area at each grid i. In the Louvain experiment, the err_z values are 0.05%, 0.007%, and 0.05% at $5t_0$, $7t_0$, and $10t_0$ respectively. In the Taipei experiment, the err_z values are 0.02%, 0.005%, and 0.001% at $3t_0$, $4t_0$, and $5t_0$ respectively. It is evident that the mass balance errors are very small and the model preserves the mass very well.

Table **2-2**: NSEs (Nash-Sutcliffe model efficiency coefficient) at different times for the Louvain and Taipei experiments (unit: m).

	Louvain			Taipei		
	t	H	z	t	H	z
Calibration	$5t_0$	0.99	0.73	$3t_0$	0.70	0.30
Validation	$7t_0$	0.97	0.79	$4t_0$	0.75	0.48
	$10t_0$	0.96	0.56	$5t_0$	0.80	0.54

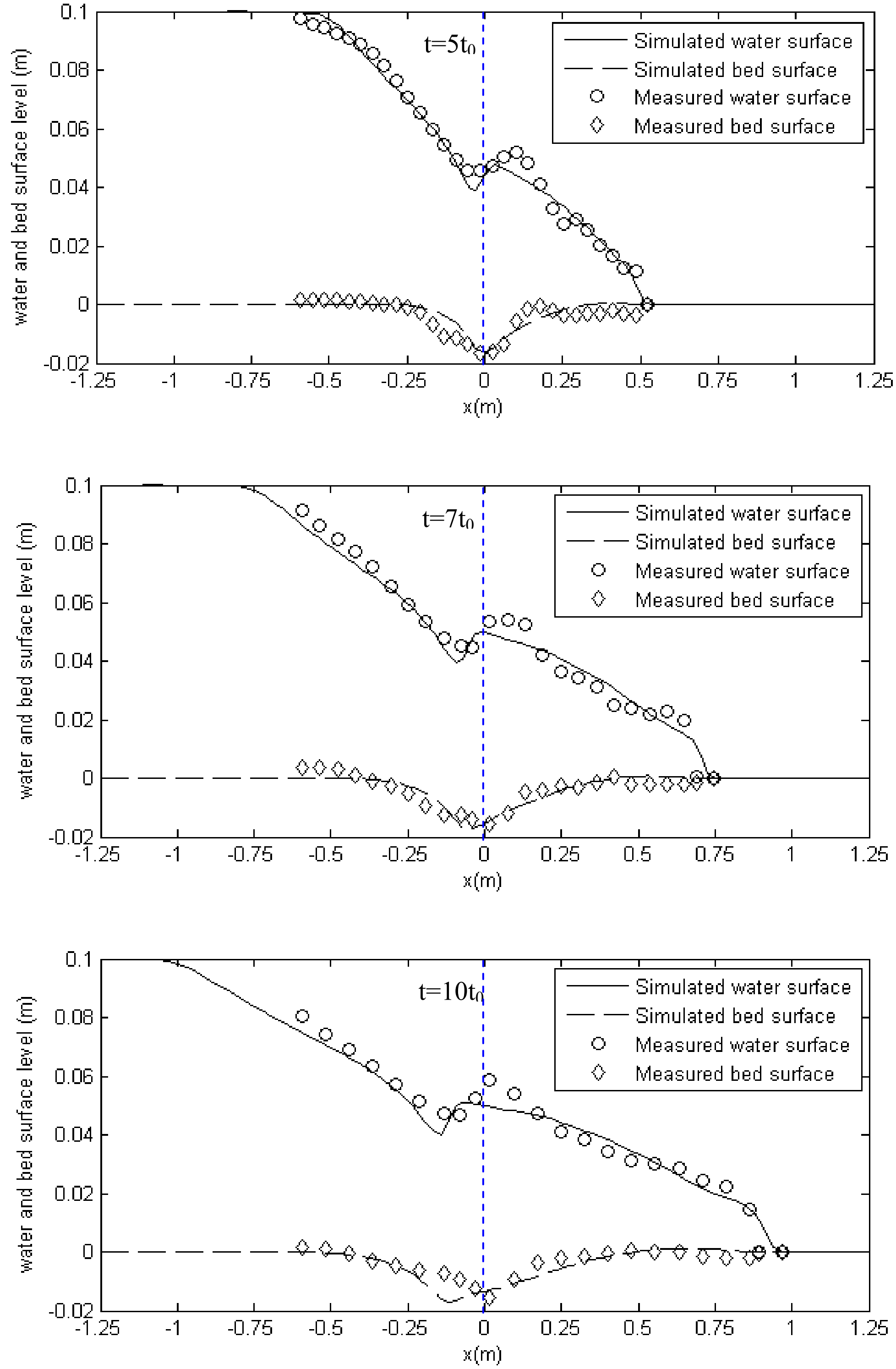

Figure **2-10**: Water and bed surface levels along the center line in the Louvain experiment (t_0 = 0.101 s). The blue dash line is the dam site.

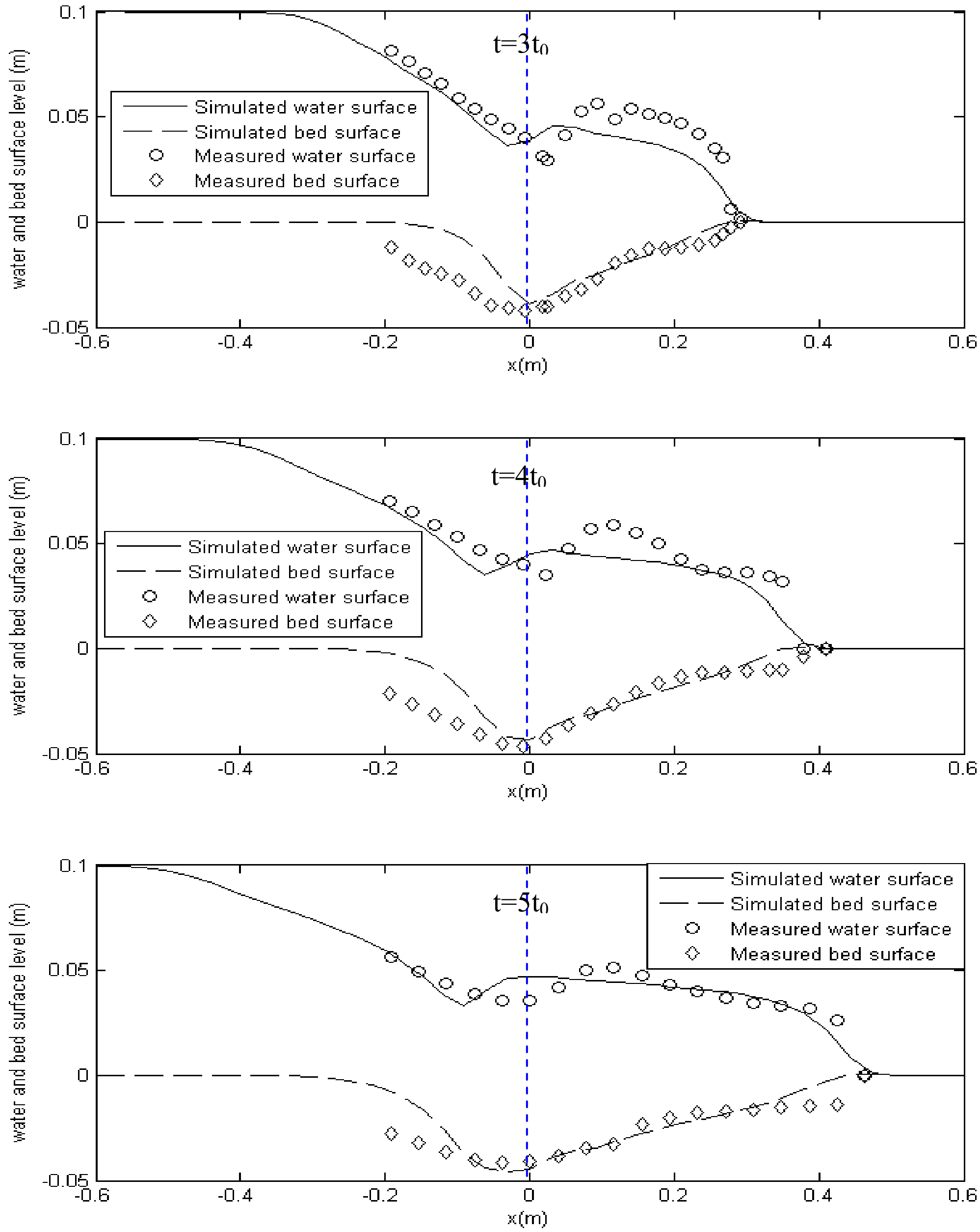

Figure **2-11**: Water and bed surface levels along the center line in the Taipei experiment (t_0 = 0.101 s). The blue dash line is the dam site.

Figure 2-12 shows the predicted sediment concentration profiles in both experiments at different times. PIHM-Hydro predicted sharp forefronts of the sediment concentration profile, which were caused by extremely high sediment concentrations in the dam break wave fronts.

Similar predictions were also made by several 1-D models [Fraccarollo and Capart, 2002; Wu and Wang, 2007] in the Taipei case at $4t_0$. In the Wu and Wang model, however, a small initial downstream flow depth was specified rather than the actual dry bed condition, which may have caused errors in mass balance and wave arrival time. By comparing Figures 2-12 (a) and (b), it is noted that the peak concentrations in the Taipei case were much higher than those in the Louvain case. The difference is due to the smaller density and lower settling velocity of sediment particles in the Taipei case which make erosion easier and deposition slower. It is also noted that the peak sediment concentration decreased with time in the Louvain case while it increased with time in the Taipei case. This difference is partly related to the different time scales of the two cases, where the Taipei experiment is run for a shorter duration than the Louvain experiment.

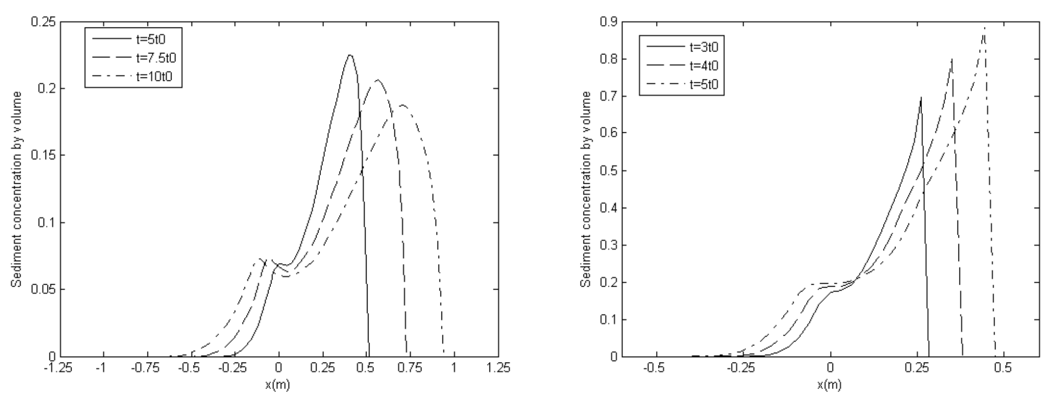

Figure **2-12**: Predicted sediment concentration profiles in Louvain (left) and Taipei (right) experiments.

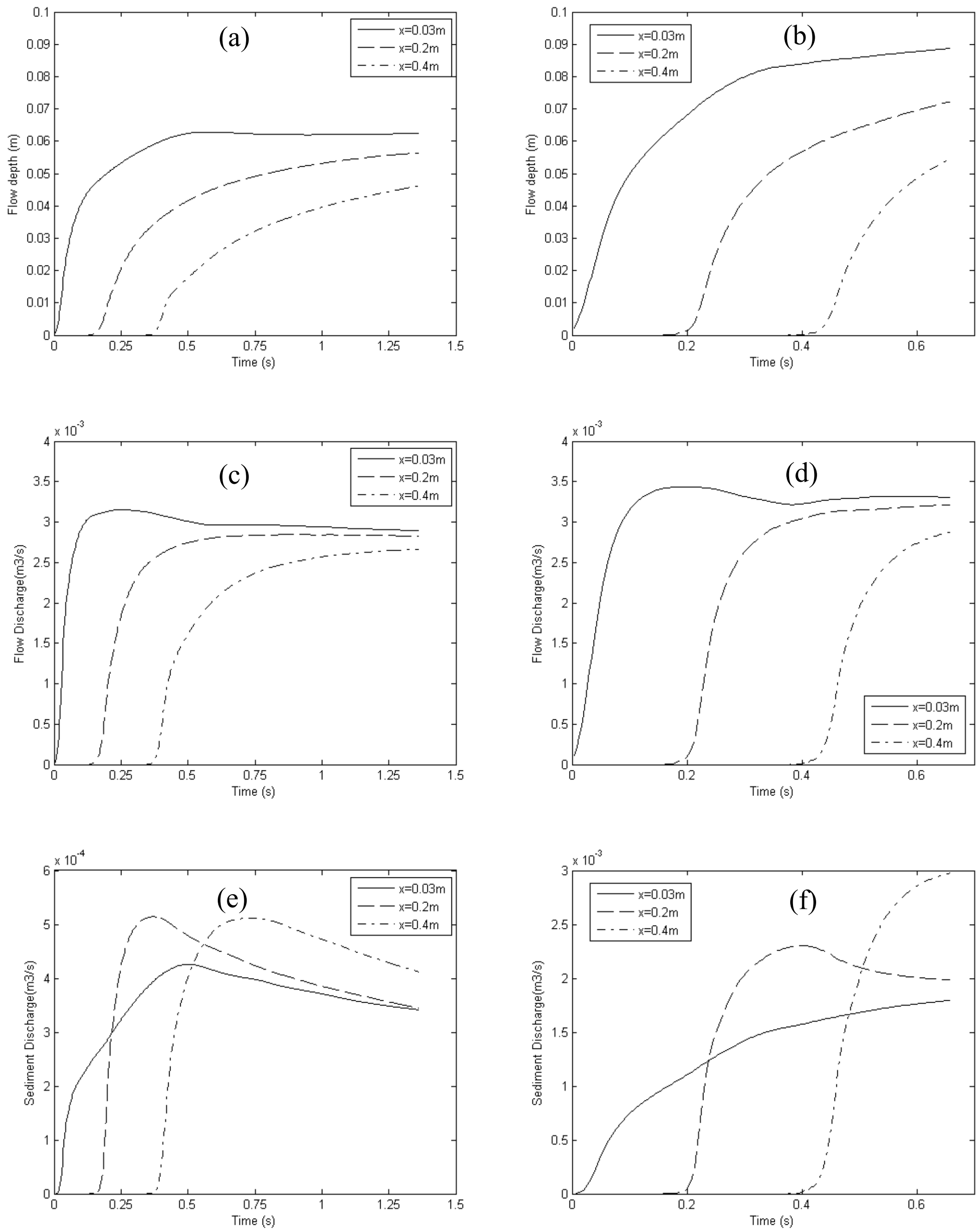

Figure **2-13**: Predicted temporal variations of flow depth ((a) and (b)), flow discharge ((c) and (d)), and sediment discharge ((e) and (f)) in Louvain (left) and Taipei (right) experiments.

Figure 2-13 illustrates the temporal variations of flow depths, flow discharge, and sediment discharge predicted by this model at x = 0.03 m, 0.2 m, and 0.4 m. One can observe that flow depth and flow/sediment discharge were all approaching some equilibrium values after a period of time. In Figures 2-12 and 2-13 it is also demonstrated that volumetric sediment concentration, flow depth and sediment discharge are very sensitive to particle size and density while discharge is not. As discussed above, that the volumetric sediment concentration is sensitive is due to the fact that the sediment particle properties influence the erosion and deposition. For the same reason, sediment discharge is also influenced by the sediment particle properties indirectly. The erosion/deposition will significantly change the bed surface which in turn influences the flow depth profile.

Mesoscale applications

River and floodplain dynamics during Malpasset dam break event

This test case is used to show the capability of PIHM-Hydro to predict the large-scale hydrodynamics over a dry bed with complex topography and boundary. The Malpasset dam was located in a narrow gorge of the Reyran river valley, about 12 km upstream of Frejus on the French Rivira. The maximum reservoir capacity was 55106 m^3. In December 1959, the dam failed explosively at night partly due to exceptionally heavy rain. The flood wave ran along the Reyran valley to Frejus and 433 casualties were reported. More detail can be found in Soares Frazao et al. [1999].

The topography of the computation domain is shown in Figure 2-14 with the location of dams, transformers, gauges, and police survey points. The overall dimensions are 175000×9000 m^2, with the sea included in the domain. The bottom elevation ranges from -20 m below sea level to 100 m. The domain was discretized into different-resolution meshes using the domain boundary and the 13541 topography survey points as the constraints. The 38208-triangle mesh and a close-up view of the computational mesh near the dam are presented in Figure 2-15. The mesh is much finer immediately downstream of the dam and along the river, where the fast and abrupt flow happened. The initial water level in the reservoir is 100 m above sea level and the bottom downstream of the dam is set dry (Figure 2-16). The solid boundary condition is imposed along all boundaries. The Strickler coefficient ranges from 30 $m^{1/3}s^{-1}$ to 40 $m^{1/3}s^{-1}$[e.g., Soares Frazao et al., 1999; Hervouet and Petitjean, 1999], corresponding to Manning's coefficient from 0.033 $s/m^{1/3}$ to 0.025 $s/m^{1/3}$. A uniform Manning coefficient of 0.033 $s/m^{1/3}$ was advised by other researchers [e.g., Goutal, 1999; Hervouet, 2000; Valiani et al., 2002]. The sensitivity of the model to the Manning's coefficient was first studied on a 26000-traingle mesh (Table 2-3). It shows that PIHM-Hydro does work best at n = 0.033 which is in agreement with the previous studies as well as the recommendation for winding natural rivers by Henderson [1966].

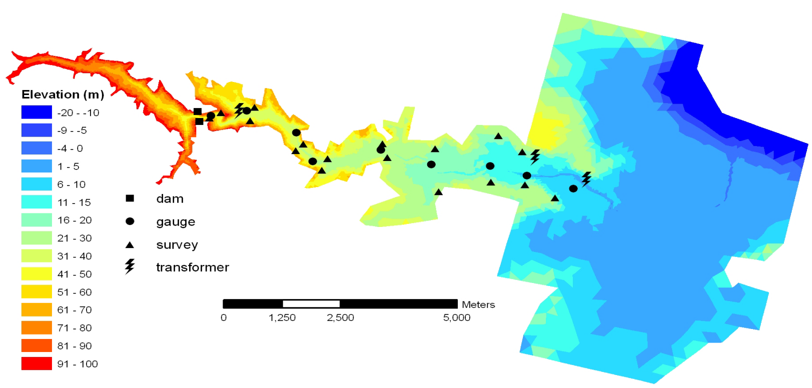

Figure **2-14**: Topography of the Reyran valley and coastal zone for Malpasset dam break event.

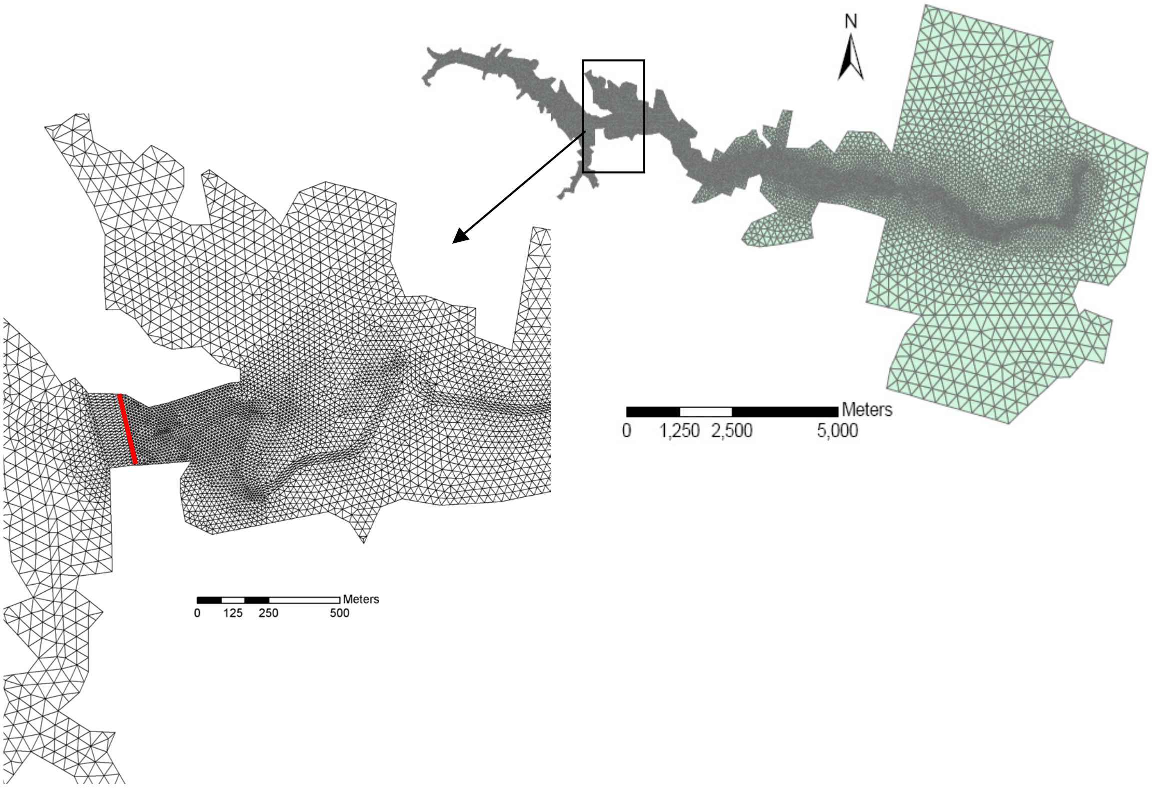

Figure **2-15**: Close-up view of the 38208-grid mesh near the dam for Malpasset dam break simulation.

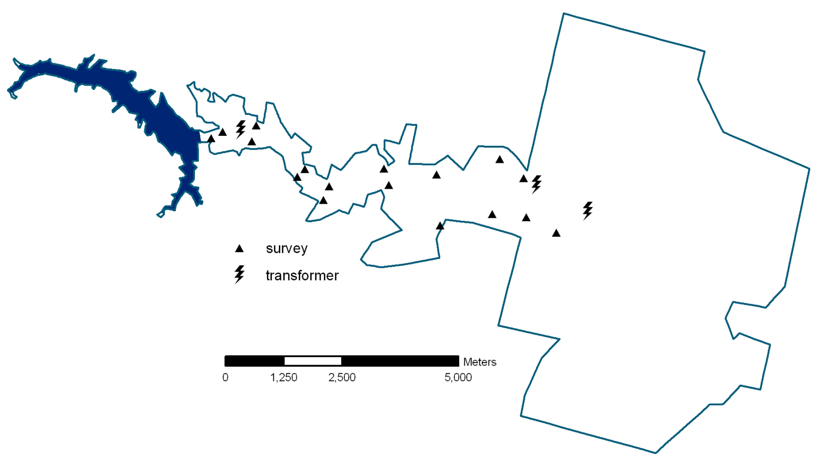

Figure **2-16**: River and floodplain dynamics during Malpasset dam break event: initial condition.

Table **2-3**: Flood arrival times at three electric transformers with different Manning's *n* on the 26000-grid mesh during Malpasset dam break event (unit: s).

No	Measured	*n*								
		0.033	0.032	0.031	0.03	0.029	0.028	0.027	0.026	0.025
A	100	**130**	132	135	139	142	143	144	145	146
B	1240	**1225**	1209	1191	1174	1156	1137	1119	1100	1079
C	1420	**1400**	1381	1361	1340	1319	1296	1275	1252	1227

Tables 2-4 and 2-5 show how the grid resolution or terrain resolution influences the numerical solutions. Due to the large magnitude of the water surface elevations, both NSE and RMSE (Root Mean Squared Error) are used here to quantitatively assess the prediction errors. It is evident that the finer spatial resolutions will result in more precise solutions. When the grid resolution reaches a threshold, say 38208 in this case, however, the accuracy does not improve much even if the grids get much finer. By comparing Table 2-4 and Table 2-5, we can see that the maximum water surface elevations (*H*) at the gauge points are more sensitive to the grid/terrain resolutions than those at the police survey points. This is due to the fact that the magnitude of the water depths (*h*) in the river are larger than the bed elevation (*z*) while at the banks the bed elevations are larger. From this analysis, we can say that the maximum water surface elevations are the better metric to assess the model accuracy. These two tables illustrate that when the grid number reach 26000 the prediction are already satisfactory at all of those measure locations (NSE>=0.97 and RMS<=3.99). A finer resolution to 38208 grids can still improve the solution remarkably. After that, the resolutions does not improve much even the resolution is significantly increased. Therefore the 38208-grid mesh with n = 0.033 is used to compare PIHM-Hydro with the others.

Table **2-4**: Maximum water level at the gauge points with Manning's $n = 0.033$ on different spatial resolutions during Malpasset dam break event (unit: m).

No	Measured	Grids number					
		5344	9100	18533	26000	**38208**	62549
6	79.15	58.66	60.14	59.80	88.89	**86.48**	86.42
7	87.2	54.84	56.93	57.30	52.76	**53.00**	53.00
8	54.9	46.42	45.69	47.30	53.51	**53.58**	53.84
9	38.6	46.27	39.07	46.00	48.52	**48.87**	48.77
10	31.9	32.22	31.48	35.64	37.68	**36.99**	37.20
11	24.15	23.24	24.61	24.34	25.54	**25.01**	25.17
12	24.9	16.72	15.63	17.61	18.07	**18.75**	18.86
13	17.25	8.99	10.38	15.25	18.35	**16.64**	16.78
14	14	11.39	12.02	13.08	12.66	**12.79**	13.11
NSE	0	0.78	0.8	0.81	0.97	**0.97**	0.97
RMSE	0	9.89	9.42	9.22	3.84	**3.55**	3.52

Table **2-5**: Maximum water level at the police survey points with Manning's $n = 0.033$ on different spatial resolutions during Malpasset dam break event (unit: m)

No	Measured	Grids number					
		5344	9100	18533	26000	**38208**	62549
1	79.15	77.36	80.13	74.96	88.09	**81.01**	80.60
2	87.2	70.23	68.88	75.67	84.99	**90.04**	91.00
3	54.9	52.29	56.84	56.52	52.92	**52.90**	52.27
4	64.7	67.79	61.64	57.80	56.98	**56.83**	60.72
5	51.1	58.00	55.04	47.93	47.61	**46.75**	44.92
6	43.75	42.81	42.22	41.46	45.67	**43.89**	45.18
7	44.35	43.19	43.56	42.93	42.49	**42.41**	41.76
8	38.6	34.18	36.03	34.18	31.73	**31.84**	32.22
9	31.9	31.70	31.75	32.01	33.10	**32.71**	32.99
10	40.75	34.31	38.30	36.54	37.70	**37.39**	38.10
11	24.15	21.26	22.94	23.11	23.77	**23.57**	24.82
12	24.9	26.59	27.70	26.91	28.23	**28.06**	26.93
13	17.25	21.85	21.83	21.82	21.82	**21.82**	21.82
14	20.7	21.36	21.23	21.21	21.28	**21.42**	21.31
15	18.6	18.89	17.48	18.37	19.36	**19.43**	18.60
16	17.25	20.10	20.83	19.99	20.20	**20.13**	20.15
17	14	16.27	15.68	15.66	15.87	**15.66**	15.94
NSE	0	0.94	0.95	0.96	0.97	**0.97**	0.98
RMSE	0	5.23	5.02	4.14	3.99	**3.44**	3.19

The predicted evolution of flood inundation is shown with the police-surveyed points in Figure 2-17. The cells with a water depth smaller than 0.01 m are considered dry. The police-surveyed points are the high-water marks which may also be considered as the flooded boundary. As can be seen from Figure 2-17, the boundary of the flooded area agrees with that survey by police quite well. To further demonstrate the advantage of PIHM-Hydro in predicting the flood wave, Table 2-6 compared the computed arrival times of the flood waves to the three electronic transformers with those from Hervouet and Petitijean [1999], Valiani et al. [2002], and Yoon and Kang [2004]. Hervouet and Petitijean's model is based on the finite element method (FE) on unstructured triangular grids while Valiani et al. and Yoon and Kang's models were developed by the HLL finite volume method (FV) on unstructured triangular and quadrilateral grids respectively. The exact arrival times of flood wavefront are unknown, and the measurements were affected by some uncertainties, e.g, in the rupture time of the dam. Therefore, in addition to the arrival times, the travel times of the flood wave between two points are also the important criterion for judging the performance of a model.

Table **2-6**: Flood arrival times at three electric transformers with Manning's $n = 0.033$ on the 38208-grid mesh during Malpasset dam break event (unit: s). FV and FE denotes the finite volume and finite element methods respectively. B-A is for the travel time of the flood wave from transformers to B, and C-B is for the travel time from C-B.

No	Measured	PIHM-Hydro	Hervouet & Petitijean (1999)	Valiani et al. [2002]	Yoon and Kang [2004]
A	100	98 (-2%)	111 (+11%)	98 (-2.0%)	103 (+3.0%)
B	1240	1226 (-1.1%)	1287 (+3.8%)	1305 (+5.2%)	1273 (+2.7%)
C	1420	1402 (-1.3%)	1436 (+1.1%)	1401 (-1.3%)	1432 (+0.8%)
B-A	1140	1128 (-1.1%)	1176 (+3.2%)	1207 (+5.9%)	1170 (+2.6%)
C-B	**180**	**176 (-2.2%)**	**149 (-17.2%)**	**96 (-46.7%)**	**159 (-11.7%)**
Method	N/A	FV	FE	FV	FV
Grid type	N/A	Triangle	Triangle	Quadrilateral	Triangle
Grid no.	N/A	38208	26000	10696	67719

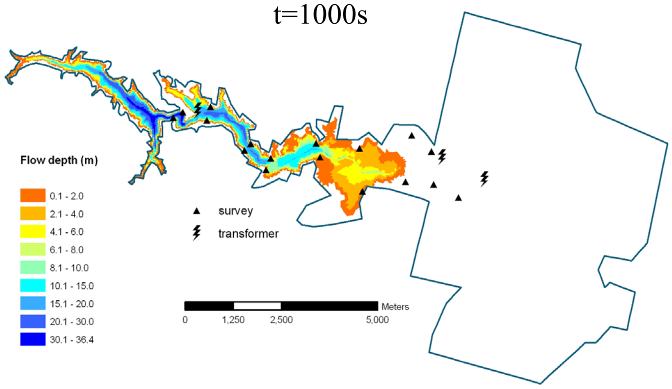
t=1000s
Flow depth (m)
0.1 - 2.0
2.1 - 4.0
4.1 - 6.0
6.1 - 8.0
8.1 - 10.0
10.1 - 15.0
15.1 - 20.0
20.1 - 30.0
30.1 - 36.4
survey
transformer
Meters
0
1,250
2,500
5,000

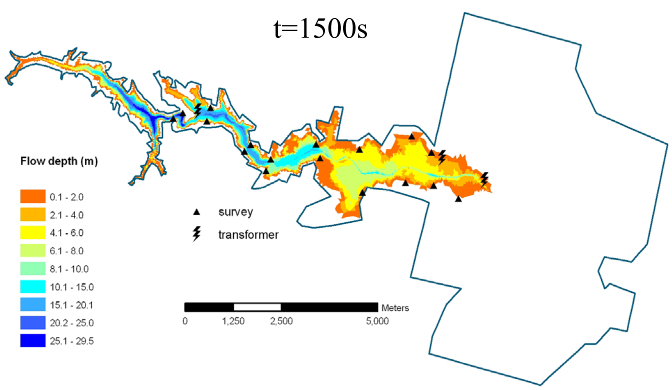
t=1500s
Flow depth (m)
0.1 - 2.0
2.1 - 4.0
4.1 - 6.0
6.1 - 8.0
8.1 - 10.0
10.1 - 15.0
15.1 - 20.1
20.2 - 25.0
25.1 - 29.5
survey
transformer
Meters
0
1,250
2,500
5,000

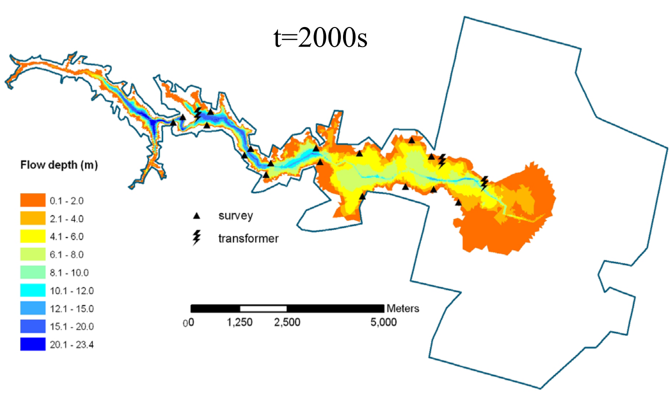
t=2000s
Flow depth (m)
0.1 - 2.0
2.1 - 4.0
4.1 - 6.0
6.1 - 8.0
8.1 - 10.0
10.1 - 12.0
12.1 - 15.0
15.1 - 20.0
20.1 - 23.4
survey
transformer
Meters
0
1,250
2,500
5,000

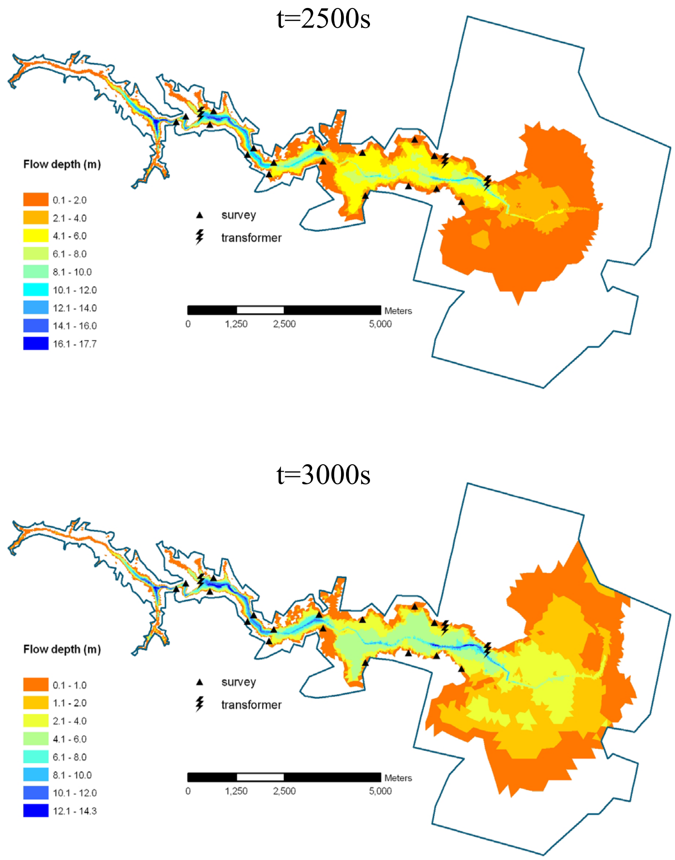

Figure **2-17**: Flood inundation map at different times during Malpasset dam break event with Manning's n = 0.033 on the 38208-grid mesh.

Firstly, from Table 2-6 we can see that the arrival times and travel times of the flood waves predicted by PIHM-Hydro are in excellent agreement with the measurement with the maximum error about 2%. More importantly, this model shows its advantage over the other models including both FE and FV-based ones with respect to these two criteria. For example, the transformers B and C are far away downstream of the dam. The travel time of the flood wave between them should be less affected by the rupture time of the dam. From Table 2-6, we can see that our model is way better than all the other models. Although it is impossible to directly compare the computational resources that these models consume due to the unavailability of the codes, we still can do some comparisons based on the grids number, grid type, and numerical methods. For example, compared to Yoon and Kang's FV model which used almost 7000 triangles, this model only about half of grids to achieve more accurate solutions.

The water level is another important criterion for judging whether a model reproduces flow phenomena accurately or not in addition to the arrival times and travel times of flood waves. Table 2-7 and Figure 2-18 present The comparisons between the predicted maximum water levels with the measured ones and the results calculated from the above-mentioned models are presented in Table 2-7 and Figure 2-18 for the gauge points in the river, and in Table 2-8 and Figure 2-19 for the police survey points at the left and right banks. As discussed above, the maximum water surface elevations in Table 2-7 are the better metric to assess model accuracy. According to Table 2-7, this model produced improved predictions than the other finite volume models with smaller RMSEs while achieved similar accuracy with the commercial finite-element model. Especially, the improvement is achieved by using much fewer grids than the Yoon and Kang's finite volume model. From both Tables 2-7 and 2-8, we can see that PIHM-Hydro perform very well in terms of stability, accuracy, and robustness on the complicated geometry and topography as well as intensive wetting/drying processes.

Table **2-7**: Maximum water level at the gauge points with Manning's n = 0.033 on the 38208-grid mesh during Malpasset dam break event (unit: m).

No	Measured	PIHM-Hydro	Hervouet &Petitijean (1999)	Valiani et al. [2002]	Yoon & Kang [2004]
6	84.2	86.48	81.98	88.35	80.85
7	49.1	53.00	53.86	54.44	55.8
8	54	53.58	53.8	53.26	53.54
9	40.2	48.87	48.39	47.93	48.68
10	34.9	36.99	36.88	36.52	37
11	27.4	25.01	25.54	25.38	25.7
12	21.5	18.75	18.48	19.14	19.23
13	16.1	16.64	17.43	17.66	17.12
14	12.9	12.79	12.6	12.76	12.86
NSE	0	0.97	0.97	0.97	0.96
RMSE	0	3.55	3.54	3.66	3.97

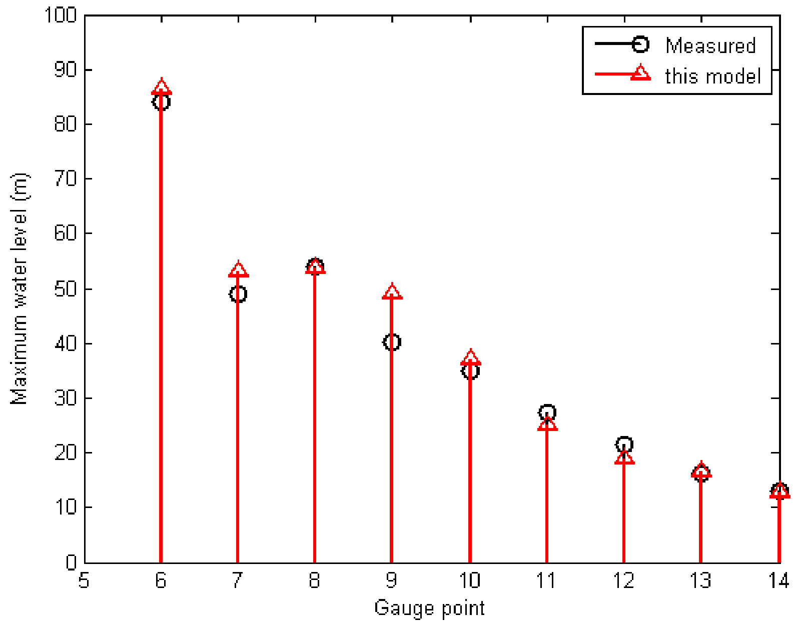

Figure **2-18**: Maximum water level at the gauge points with Manning's n = 0.033 on the 38208-grid mesh during Malpasset dam break event.

Table **2-8**: Maximum water level at the police survey points with Manning's n = 0.033 on the 38208-grid mesh during Malpasset dam break event (unit: m).

No	Measured	PIHM-Hydro	Valiani et al. (2002)	Yoon & Kang (2004)
1	79.15	81.01	75.96	75.13
2	87.2	90.04	89.34	87.38
3	54.9	52.90	53.77	55.09
4	64.7	56.83	59.64	57.41
5	51.1	46.75	45.56	47.11
6	43.75	43.89	44.85	45.74
7	44.35	42.41	42.86	40.47
8	38.6	31.84	34.61	32.58
9	31.9	32.71	32.44	33.16
10	40.75	37.39	38.12	38.29
11	24.15	23.57	25.37	25.16
12	24.9	28.06	27.35	25.96
13	17.25	21.82	23.58	24.41
14	20.7	21.42	23.19	20.58
15	18.6	19.43	19.37	19.08
16	17.25	20.13	20.39	17.04
17	14	15.66	14.23	16
NSE	0	0.97	0.98	0.97
RMSE	0	3.44	3.10	3.48

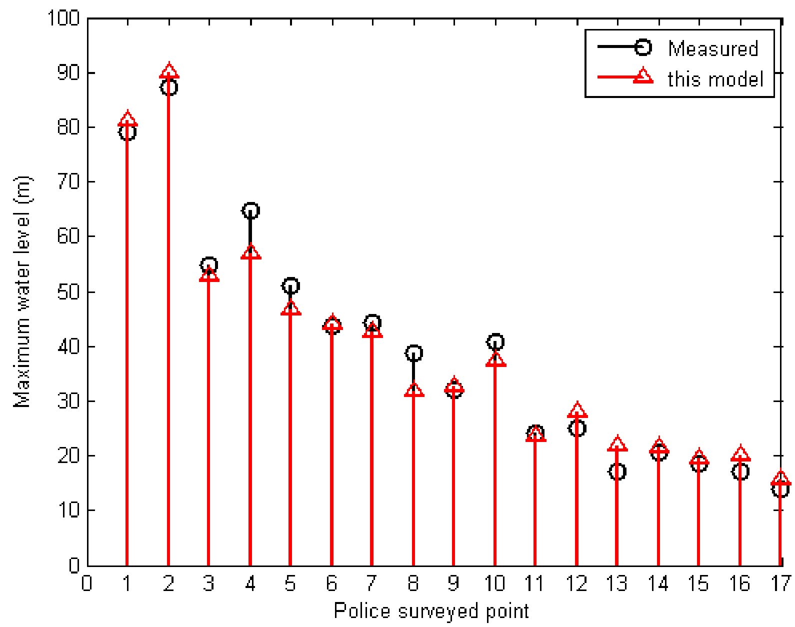

Figure **2-19**: Maximum water level at the police survey points with Manning's n = 0.033 on the 38208-grid mesh during Malpasset dam break event.

Mesoscale dam break and sediment dynamics

In a previous section PIHM-Hydro was applied to predict the small-scale water-sediment flow dynamics in the Louvain and Taipei experiments. To further examine the capability of the model in large-scale prediction, the model is applied to a hypothetical 2-D dam break in a wide river over a movable bed. A 1-D test case were simulated by Cao et al. [2004] and Wu and Wang [2007]. The river is 50 km-long and 1000 m-wide, and the dam was initially located at the middle of the channel. The initial water depths upstream and downstream of the dam are 40 m and 2 m respectively at static state. Initially the channel bed is horizontal, and composed of noncohesive uniform sediment with grain size 4 mm. The computational domain was discretized into 3329 triangles. According to Cao et al. [2004], the values are set as 0.045 for the critical Shields parameter (θ_c), 0.4 for the bed material porosity (p), 2.65 for the specific gravity of sediment particle, and 0.03 for the Manning's coefficient (n). The constant α was set as 8.5e-6. The entrainment/deposition equations (10) and (11) were also compared with Cao's [Cao et al., 2004] and their limited version proposed by Wu and Wang [2007].

The computed water surface elevation and bed elevation along the center line at different times after dam break are presented in Figure 2-20. Firstly one can see that the hypothetic dam-break flow caused serious erosion. The sediment transport process had significant impact on the flow dynamics such as the water surface profiles and wave speeds. The results show a similar feature in an early stage (e.g., t = 2 min) as observed in the small scale experiments. A hydraulic jump is formed near the dam site due to rapid bed erosion. However, this jump attenuates progressively as it propagates upstream and eventually disappears after about 8 minutes. Compared to the flow without sediment transport, the forward wave fronts with sediment transport move slowly at the early stage while the backward wave propagated essentially at the same speed, which were also observed by other researchers [Cao et al., 2004; Wu and Wang, 2007]. However, after a certain period of time, e.g., 20 min, the forward wave fronts using Equations (10) and (11) propagated at the same speed as those without sediment transport while the ones using Cao's and Wu's entrainment/deposition equations propagated faster.

At the early stage, the results based on Equations (10) and (11) are close to Wu's. After that, there is big difference between them especially with respect to the bed surface. From the simulation using Equations (10) and (11), an interesting feature of the PIHM-Hydro solution is the erosion-deposition which occurs just after the wave fronts passed, which is not observed in the other models. For example, Cao's model shows excessive erosion deposition occurs while Wu's model shows attenuated erosion near wave front. From Figure 2-20, it is also noted that only Cao's equations predicted a separate bore upstream of the wave front. This is caused by the over-prediction of sediment entrainment by Cao's equations [Wu and Wang, 2007].

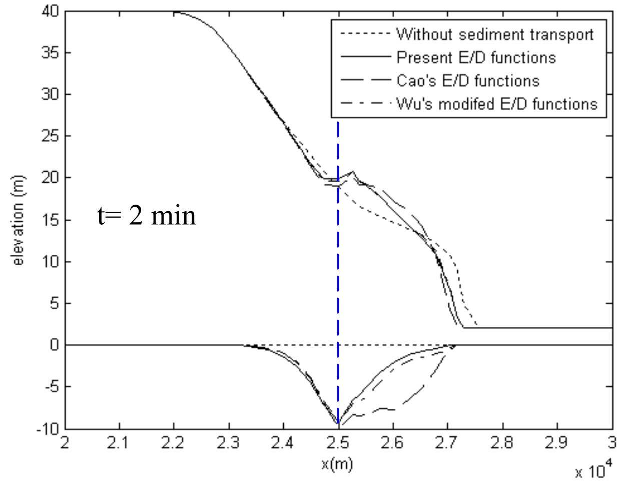
Without sediment transport
Present E/D functions
Cao's E/D functions
Wu's modifed E/D functions
t= 2 min
elevation (m)
x(m)
x 10^4

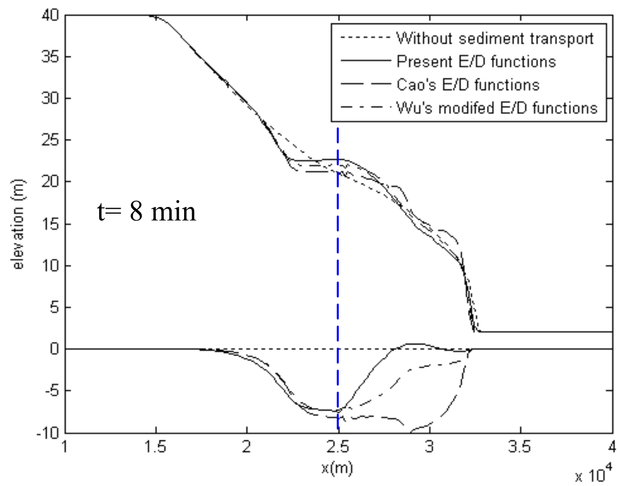
Without sediment transport
Present E/D functions
Cao's E/D functions
Wu's modifed E/D functions
t= 8 min
elevation (m)
x(m)
x 10^4

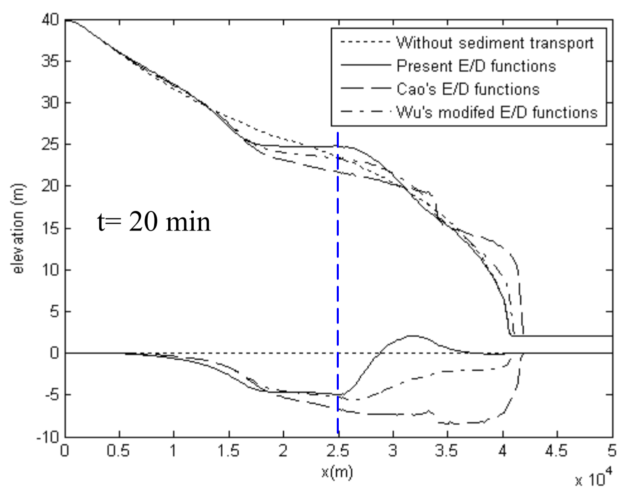
Without sediment transport
Present E/D functions
Cao's E/D functions
Wu's modifed E/D functions
t= 20 min
elevation (m)
x(m)
x 10^4

Figure **2-20**: Predicted water and bed surface levels along the center line in the large-scale wide river test case. The blue line represents the dam site.

Conclusions

In this study, the first 2-D high-order model (PIHM-Hydro) to fully couple shallow water flow, sediment transport and morphological evolution in the successful simulation of a real flow field is developed over a wide range of physical and numerical conditions. The sediment transport module simulates the non-equilibrium total-load sediment transport. New formulations for deposition and erosion are also proposed. A stable and second-order accurate numerical algorithm was implemented on unstructured grids using an upwind finite volume method combined with a multidimensional gradient reconstruction and slope limiter technique. This is the first 2-D high-order model to fully couple shallow water flow and sediment transport in the successful simulation of a real flow field. The NSE (Nash-Sutcliffe model efficiency coefficient) and RMSE (Root mean squared error) were used as a metric to examine the fit of the model to multiple-sale test cases of hydrodynamics and sediment transport.

The advantages of the present model are that (1) it can handle complicated geometry by using the Delaunay triangulation based on Shewchuk's algorithm; (2) it is capable of producing accurate and stable solutions over a wide range of spatial scales and hydrological events such as discontinuous flow and wetting/drying process by using the approximate Riemann solver and the semi-implicit time integration technique based on the CVODE; and (3) it can accurately simulate the interactions of hydrodynamics, sediment transport and morphological evolution by fully coupling these processes physically i.e., considering the multi-phase flow dynamics, and numerically.

The successful application of this model on the test cases across multiple scales is just the illustration of those advantages. The microscale Bellos experiment shows this model is accurate and stable to simulate the wetting/drying process and the supercritical flow. The rainfall-runoff experiment indicates that this model is very robust and mass-conservative in rainfall-driven overland-channel flow with intensive wetting/drying processes.

The model is further applied to a mesoscale flood event, Malpasset dam break accident, with complex topography and geometry as well as discontinuous rapid flow and wetting/drying processes. The results show this model is in excellent agreement with the measurement including the arrival times and travel times of flood wave, the maximum water surface at the river and the banks as well as the boundary of flood area. More importantly, this model shows its advantage over the other models in terms of accuracy. Comparison of this model to another finite volume model on unstructured triangular grids further indicates the computational efficiency of PIHM-Hydro.

The model was also applied to simulate the interactions of water flow, sediment transport and morphological evolution over different spatial scales. The microscale experiment of flow and sediment transport following dam break demonstrate the model predicted the interaction between hydrodynamics and sediment transport fairly well. Applications of PIHM-Hydro to both the microscale and mesoscale test cases show that (1) the hydraulic jumps are formed near the initial dam sites due to rapid bed erosion caused by heavy flood and propagated upstream; (2) the extremely high sediment concentrations in the dam break wave fronts lead to the sharp forefronts of the sediment concentration profile; and (3) after long time relative to the wave front duration (e.g. 20 minutes in the large river case) deposition occurs due to the very high sediment concentration in the water column, which was not observed in other models studied here.

References

[49] Abbott, M.B., J.A. Bathurst, P.E. and Cunge. 1986. An Introduction to the European Hydrological System-Systeme Hydrologicque Europeen “SHE” 2: Structure of a physically based distributed modeling system. Journal of Hydrology, 87: 61-77.

[50] Aizinger,V. and C. Dawson. 2002. A discontinuous Galerkin method for two-dimensional flow and transport in shallow water. Advances in Water Resources, 25: 67-84.

[51] Akanbi, A. and N.D. Katopodes. 1988. Model for flood propagation on initially dry land. Journal of Hydraulic Engineering, 114: 689-719.

[52] Alcrudo,F. and P. Garcia-Navarro. 1993. A high-resolution Godunov-type scheme in finite volumes for the 2D shallow-water equations. International Journal for Numerical Methods in Fluids, 16 (6): 489-505.

[53] Alcrudo, F. and E. Gil. 1999. The Malpasset dam break case study. The Proceeding of the 4th CADAM meeting, Nov. 18-19, Zaragoza, Spain.

[54] Ambrosi, D. 1995. Approximation of Shallow Water Equations by Roe’s Riemann Solver. Int. J. Num. Methods in Fluids, 20: 157–168.

[55] Anastasiou, K., and C. T. Chan. 1997. Solution of the 2D shallow water equations using the finite volume method on unstructured triangular meshes. International Journal for Numerical Methods in Fluids, 24: 1225-1245.

[56] Begnudelli, L. and B.F.Sanders. 2006. Unstructured Grid Finite Volume Algorithm for Shallow-Water Flow and Scalar Transport with Wetting and Drying. Journal of Hydraulic Engineering, 132(4): 371-384.

[57] Bellos, C. and V.Hrissanthou. 1998. Numerical Simulation of Sediment Transport Following a Dam Break. Water Resources Management, 12: 397-407.

[58] Bellos, C.V., J.V. Soulis, and J.G., Sakkas. 1992. Experimental investigation of two-dimensional dam-break induced flows. J. Hydraul. Res., 30 (1): 47-63.

[59] Bennett, J.P. 1974. Concepts of mathematical modeling of sediment yield. Water Resources Research, 10(3): 485-492.

[60] Bhatt,G.,M. Kumar, and C.J. Duffy. 2008. Bridging gap between geohydrologic data and Integrated Hydrologic Model: PIHMgis. In: iEMSs 2008: International Congress on Environmental Modelling and Software.

[61] Bradford, S.F. and B.F. Sanders. 2002. Finite-volume model for shallow-water flooding of arbitrary topography. Journal of Hydraulic Engineering, 128: 289-298

[62] Caleffi, V. A. Valiani, and A. Zanni. 2003. Finite volume method for simulating extreme flood events in natural channels. Journal of Hydraulic Research, 41 (2): 167-177.

[63] Cao, Z., G. Pender, S. Wallis, and P. Carling. 2004. Computational dam-break hydraulics over erodible sediment bed. Journal of Hydraulic Engineering, 130 (7): 689-703.

[64] Capart, H. and D.L.Young. 1998. Formation of a jump by the dam-break wave over a granular bed. Journal of Fluid Mechanics, 372: 165-187.

[65] Castro Diaz, M.J.,E.D. Fernandez-Nieto, and A.M. Ferreiro.2008. Sediment transport models in Shallow Water equations and numerical approach by high order finite volume methods. Computers &Fluids, 37: 299-316.

[66] Delanunay, B. 1934. Sur la sphere vide, Bull. Acad. Science USST VII: Class Sci. Mat. Nat., b, 793.

[67] diGiammarco, P., E. Todini, and P.Lamberti. 1996. A conservative finite elements approach to overland flow: the control volume finite element formulation. Journal of Hydrology, 175: 267-291.

[68] Fagherazzi, S. and T.Sun. 2003. Numerical simulations of transportation cyclic steps. Computers and Geosciences. 29: 1143-1154.

[69] Farshi, D. and S. Komaei. 2005. Discussion of "Finite Volume Model for Two-Dimensional Shallow Water Flows on Unstructured Grids" by Tae Hoon Yoon and Seok-Koo Kang. Journal of Hydraulic Engineering, 131 (12): 1147-1148.

[70] Fennema, R.J., and M. H. Chaudhry. 1990. Explicit methods for 2D transient free-surface flows. J. Hydraul. Eng., 116 (8): 1013-1034.

[71] Fraccarollo, L., H. CAPART, and Y. ZECH. 2003. A Godunov method for the computation of erosional shallow water transients.International Journal for Numerical Methods in Fluids, 41 (9): 951-976.

[72] Frink, N. T. 1992. Upwind scheme for solving the Euler equations on unstructured tetrahedral meshes. AIAA J., 30 (1): 70-77.

[73] Goutal, N. 1999. The Malpasset Dam Failure – An Overview and Test Case Definition. The Proceeding of the 4th CADAM meeting, Nov. 18-19, Zaragoza, Spain.

[74] Harten, A. andJ.M. Hyman. 1983. Self-adjusting grid for one dimensional hyperbolic conservation laws. Journal of Computational Physics, 50 (2): 235–269.

[75] Henderson, F.M. 1966. Open channel flow. MacMIllan Publishers, New York.

[76] Hervouet, J.M. 2000. A high resolution 2-D dam-break model using parallelization. Hydrological Processes, 14: 2211-2230.

[77] Hervouet, J. M., and A. Petitijean. 1999. Malpasset dam-break revisited with two-dimensional computations. J. Hydraul. Res., 37 (6): 777-788.

[78] Hindmarsh and Serban. 2005. User Documentation for cvode v2.3.0. Center for Applied Scientific Computing Lawrence Livermore National Laboratory, UCRL-SM-208108.

[79] Holmes,D. G. and S. D. Connell.1989. Solution of the 2D Navier–Stokes equations on unstructured adaptive grids. AIAA Pap. 89-1932 in Proc. AIAA 9th CFD Conference.

[80] Horritt, M.S. 2000. Calibration and validation of a 2-dimensional finite element flood flow model using satellite radar imagery. Water Resources Research, 36 (11): 3279-3291.

[81] Hubbard, M.E. 1999. Multidimensional slope limiters for MUSCL-type finite volume schemes on unstructured grids. Journal of Computational Physics, 155: 54–74.

[82] Hudson, J. and P.K. Sweby. 2003. Formulations for Numerically Approximating Hyperbolic Systems Governing Sediment Transport. Journal of Scientific Computing, 19: 225-252.

[83] Hudson,J. and P.K. Sweby. 2005. A high-resolution scheme for the equations governing 2D bed-load sediment transport.International Journal for Numerical Methods in Fluids, 47:1085-1091.

[84] Jawahar, P., and H. Kamath. 2000. A high-resolution procedure for Euler and Navier-Stokes computations on unstructured grids. Journal of Computational Physics, 164: 165-203.

[85] Katopodes, N. and T. Strelkoff. 1978. Computing two-dimensional dam-break flood waves. Journal of the Hydraulics Division, ASCE 104: 1269-1288.

[86] Leveque, R.J. 2002 Finite Volume methods for hyperbolic problems, Cambridge University Press.

[87] Loukili, Y. and A.Soulaimani. 2007. Numerical Tracking of Shallow Water Waves by the Unstructured Finite Volume WAF Approximation.International Journal for Computational Methods in Engineering Science and Mechanics,8 (2): 75-88.

[88] Martin, N and S.M. Gorelick. 2005. A MATLAB surface fluid flow model for rivers and streams.Computers and Geosciences, 31: 929-946.

[89] Molls, T. and M.H. Chaudhry. 1995. Depth averaged open channel flow model. Journal of Hydraulic Engineering, 121: 453-465.

[90] Moriasi, D. N. et al. 2007. Model Evaluation Guidelines for Systematic Quantification of Accuracy in Watershed Simulations. Transactions of the ASABE, 50:(3): 885–900.

[91] Nash, J. E. and J. V. Sutcliffe. 1970. River flow forecasting through conceptual models part I — A discussion of principles, Journal of Hydrology, 10 (3): 282–290.

[92] Ottevanger, W. 2005. Discontinuous finite element modeling of river hydraulics and morphology. Master's thesis. University of Twente.

[93] Qu, Y., and C. J. Duffy. 2007. A semidiscrete finite volume formulation for multiprocess watershed simulation, Water Resources Research, 43, W08419, doi:10.1029/2006WR005752.

[94] Roe, P. L. 1981. Approximate Riemann solvers, parameter vectors, and difference schemes. Journal of Computational Physics, 43: 357-372.

[95] Rosatti, G. and L.Fraccarollo. A well-balanced approach for flows over mobile-bed with high sediment-transport. Journal of Computational Physics, 2006, 220 (1): 312-338.

[96] Shewchuk, J.R. 1997. Delaunay refinement mesh generation, PhD Thesis, Carnegie Mellon University.

[97] Shu, C. W., and S. Osher. 1988. Efficient implementation of essentially non-oscillatory shock capturing schemes. J. Comput. Phys., 77: 439-471.

[98] Simpson, G. and S. Castelltort.2006. Coupled model of surface water flow, sediment transport and morphological evolution. Computers & Geosciences, 32: 1600-1614.

[99] Sleigh, P.A., M. Berzins, P.H. Gaskell and N.G. Wright. 1998. An unstructured finite-volume algorithm for predicting flow in rivers and estuaries. Computers and Fluids, 27 (4): 479-508.

[100] Soares Frazao, S., F. Alcrudo and N. Goutal. 1999. Dam-break test cases summary. The Proceeding of the 4th CADAM meeting, Nov. 18-19, Zaragoza, Spain.

[101] Tayfur, G., M.L.Kavvas, R.S.Govindaraju, and D.E.Storm. 1993. Applicability of St Venant equations for two-dimensional overland flows over rough infiltration surfaces. Journal of Hydraulic Engineering, 119 (1): 51-63.

[102] Toro, E.F. 1999. Riemann Solvers and Numerical Methods for Fluid Dynamics. Springer-Verlag.

[103] Toro, E.F. 2001. Shock-capturing Methods for Free-surface Shallow Flows. John Wiley & Sons: Chichester.

[104] Valiani, A., V. Caleffi, and A. Zanni. 2002. Case Study: Malpasset dam-break simulation using a two-dimensional finite volume method. Journal of Hydraulic Engineering,128 (5): 460-472.

[105] VanderKwaak, J. 1999. Numerical simulation of flow and chemical transport in integrated surface-subsurface hydrologic systems. Ph.D Thesis in Earth Sciences, University of Waterloo, Waterloo, Ontario, Canada.

[106] Voronoi, G. 1908. Nouvelles applications des parameters continues a la theorie des formes quadratiquess, dieuxiemememoire: researches sur les parallelloedres primitive. J. ReineAngew. Math., 134-198.

[107] Wang, J.W. and R.X. Liu.2000. A comparative study of finite volume methods on unstructured meshes for simulation of 2D shallow water wave problems. Math. Comput. Simul. 53: 171–184.

[108] Wu, W. and S.Wang. 2007. One-Dimensional Modeling of Dam-Break Flow over Movable Beds. Journal of Hydraulic Engineering, 133(1):48-58.

[109] Yoon,T.H. and Kang, S.K. 2004. Finite volume model for two-dimensional shallow water flows on unstructured grids. Journal of Hydraulic Engineering, 130(7):678-688.

[110] Zhao, D. H. and H. W. Shen, G. Q. Tabios III, J. S. Lai, andW. Y. Tan. 1994. Finite-volume two-dimensional unsteady-flow model for river basins. Journal of Hydraulic Engineering: 120 (7): 863-883.

Chapter 3

FULLY-COUPLED MODELING OF SHALLOW WATER FLOW AND POLLUTANT TRANSPORT ON UNSTRUCTURED GRIDS

Abstract

Understanding the space-time dynamics of pollutant transport remains an essential impediment to accurate prediction of impacts on the ecology of rivers and coastal areas and also for establishing efficient strategies for pollution control and environmental protection. Numerical models are a powerful tool to study the water flows and pollutant transport, and recently a new generation of models is being developed to simulate the coupled flow and pollutant transport in shallow water. In this paper, a two-dimensional fully-coupled model of shallow water flows and pollutant transport was developed using a triangular unstructured grid (TIN: triangular irregular network), which is also an important module of the PIHM-Hydro modeling system. The model is based on a cell-centered upwind finite volume method using the HLL approximate Riemann solver. A multidimensional linear reconstruction technique and multi-dimensional slope limiter was implemented to achieve a second-order spatial accuracy. In order to make the model efficient and stable, an explicit-implicit method was used in temporal discretization by an operator splitting technique. A test case of the pollutant transport in a square cavity is used to validate the model. Then the model was further applied to two pollutant transport scenarios: microscale pollutant transport following dam break and mesoscale pollutant transport driven by storm surge in Galveston Bay. The numerical results show that the model could accurately predict the flow dynamics and pollutant transport in extreme events such as a dam break and a storm surge.

According to the prediction of the model, the storm surge caused by the Hurricane Ike significantly extended the polluted area.

Introduction

Understanding the dynamics of pollutants and their impacts on water quality is essential to establishing scientifically justified and practically efficient management strategies for pollution control and environmental protection.

This paper examines a two dimensional representation of the shallow water equations and the advection-diffusion equation for the pollutant transport. Earlier approaches decouples the flow from the dynamics of contaminant transport assuming that flow is not influenced at low concentrations, and the non-conservative forms of the equations can be used by assuming the flow depth, velocities, and bed elevation vary smoothly in time and space [Murillo et al., 2005]. These approaches are inappropriate and lead to inaccurate solution in some practical situations, e.g., when the flow changes fast in time and/or space. Under these conditions it may be necessary to develop a fully coupled model in conservative form. According to Murillo et al. [2005] it is conditions of rapidly varying flow that can lead to numerical instabilities in the pollutant concentration, and therefore this system should be treated as a hyperbolic system with the diffusion term as the source term.

It is challenging to numerically solve this kind of hyperbolic equations within a system of coupled nonlinear partial differential equations. In many practical applications, the numerical solution is made even more difficult by the complexity of non-flat and rough bed forms. Numerous methods have been developed for solving the shallow water equations, including the method of characteristics [e.g., Katopodes and Strelkoff, 1978], finite difference [e.g., Molls and Chardhry, 1995], finite element [e.g., Aizinger and Dawson, 2002], and finite volume methods [e.g., Toro, 2001]. As discussed in Chapter 2, compared to the other methods, the finite volume method conserves the local and global masses, can be flexibly applied to irregular domains and unstructured grids, and require less memory. Therefore, the finite volume method is used in this paper.

Recently, several models were developed to simulate coupled flow and pollutant transport in shallow water using finite volume methods. Murillo et al. [2005] applied the first-order Roe's scheme to study the pollutant transport by a shallow water flow in a microscale test case did not verify the results against lab experiments or a real flow field. Another drawback is that this model is based on the Roe's scheme without an entropy fix which may produce nonphysical entropy-violating solutions for the critical and supercritical flows. Benkhaldoun et al. [2007] used a well-balanced finite volume non-homogeneous Riemann solver (SRNH). The principal drawback of this method is that one parameter must be evaluated by an empirical equation and it is also difficult to implement compared to the traditional approximate Riemann solvers. To solve these problems in existing models, the objective of this paper is to develop a two-dimensional fully-coupled model of shallow water flows and pollutant transport based on a cell-centered upwind finite volume method using the HLL approximate Riemann solver on unstructured triangular grids (TIN). This is also an important module of the PIHM-Hydro modeling system. Compared to the above methods, the HLL approximate Riemann solvers [Harten et al., 1983] modified by Toro [1999] are robust and produce excellent results for a wide range of flow conditions [Zopou and Roberts, 2003]. It also avoids the entropy violating solution and explicitly includes the contact discontinuity which is ignored in other Riemann solvers except Osher's [Osher and Solomen, 1982]. However, the HLL scheme is much simpler to implement compared to Osher's scheme. A multidimensional linear reconstruction technique and multi-dimensional slope limiter [Jawahar and Kamath, 2000] are implemented to achieve a second-order spatial accuracy. The technique introduced by Bradford and Sanders [2002] is adopted to mitigate the unbalanced approximation problems over bed slopes. In order to make the model efficient and stable, an explicit-implicit method is used in temporal discretization by an operator splitting technique, i.e., the advection part and non-stiff source terms are solved using explicit scheme while the diffusion term and the stiff source terms are handled by fully implicit scheme. A test case of the pollutant transport in a square cavity is first used to validate the model. In order to demonstrate its capability to provide accurate and efficient predictions for pollutant transport by shallow water flows, the model was further applied to two test cases over different scales including microscale pollutant transport following dam break and mesoscale pollutant transport driven by storm surge in Galveston Bay.

Methodology

Mathematical Formulation

The model is represented by the two-dimensional shallow water equations coupled with the advection-dispersion equation for pollutant transport. The 2-D shallow water equations are derived from the Navior-Stokes equations by assuming negligible velocity change and hydrostatic pressure distribution in vertical direction, and incompressibility of water [e.g., Tan, 1992; Liggett, 1994]. The shallow water equations written in conservative form are as follows:

$$\frac{\partial h}{\partial t}+\frac{\partial uh}{\partial x}+\frac{\partial vh}{\partial y}=S_p \tag{1}$$

$$\frac{\partial(uh)}{\partial t}+\frac{\partial\left(u^2h+gh^2/2\right)}{\partial x}+\frac{\partial(uvh)}{\partial y}=-gh\left(S_{ox}+S_{fx}\right)+f_c vh+\frac{1}{\rho}\left(\frac{\partial\left(hT_{xx}\right)}{\partial x}+\frac{\partial\left(hT_{xy}\right)}{\partial y}\right)+F_x \tag{2}$$

$$\frac{\partial(vh)}{\partial t}+\frac{\partial(uvh)}{\partial x}+\frac{\partial\left(v^2h+gh^2/2\right)}{\partial y}=-gh\left(S_{oy}+S_{fy}\right)-f_c uh+\frac{1}{\rho}\left(\frac{\partial\left(hT_{yx}\right)}{\partial x}+\frac{\partial\left(hT_{yy}\right)}{\partial y}\right)+F_y \tag{3}$$

In this two-dimensional model, the depth-averaged pollutant transport is of primary interest. The advection-dispersion equation is defined as:

$$\frac{\partial(\psi h)}{\partial t}+\frac{\partial(\psi uh)}{\partial x}+\frac{\partial(\psi vh)}{\partial y}=\frac{\partial}{\partial x}h\left(K_{xx}\frac{\partial c}{\partial x}+K_{xy}\frac{\partial c}{\partial y}\right)+\frac{\partial}{\partial y}h\left(K_{yx}\frac{\partial c}{\partial x}+K_{yy}\frac{\partial c}{\partial y}\right)+S_c \tag{4}$$

where t = time (T), x and y = horizontal coordinates (L), h = flow depth (L), u and v = depth-averaged flow velocity in x- and y-directions (L/T), ψ = depth-averaged volumetric pollutant concentration (L^3/L^3), g = gravitational acceleration (L/T^2), S_{0x} and S_{0y}= bed slopes in x-and y-directions (L/L), S_{fx} and S_{fy} = friction slopes in x-and y-directions (L/L), K_{xx}, K_{xy}, K_{yx}, and K_{yy} = empirical dispersion coefficients accounting for turbulent diffusion and shear flow dispersion (L^2/T), S_p= the additional source/sink including precipitation, infiltration etc., S_c= the additional source/sink for the pollutant, T_{xx}, T_{xy}, T_{yx}, and T_{yy} = depth-averaged turbulent stresses, ρ= the water density, F_x and F_y = the additional forces arising from wind stress, tidal potential, atmospheric pressure etc., f_c = the coefficient of the Coriolis force resulting from the earth's rotation (1/T) which is calculated from:

$$f_c = 2\Omega \sin\varpi \tag{5}$$

where Ω is the angular rotation rate of the Earth = π/12 radians/hour, and ω is the latitude. The wind stress and the diffusion of momentum caused by turbulence and viscosity are neglected in this model.

Traditionally, the shallow water equations and the pollutant transport equation were solved independently in a sequential form, i.e., solving the shallow water equations first and the pollutant transport equation next. To improve the accuracy and keep the conservation properties, these processes are fully coupled in a single system as:

$$\frac{\partial \mathbf{U}}{\partial t}+\frac{\partial \mathbf{E}}{\partial x}+\frac{\partial \mathbf{G}}{\partial y}=\mathbf{S} \tag{6}$$

Or conveniently it can be written as:

$$\frac{\partial \mathbf{U}}{\partial t}+\nabla\cdot\mathbf{F}=\mathbf{S} \tag{7}$$

where **U** is the vector of the conservative variables, **E** and **G** are the flux vectors in x- and y-direction, **S** is the vector of source terms, $\mathbf{F} = (\mathbf{E},\ \mathbf{G})^T$.

$$\mathbf{U} = \begin{pmatrix} h \\ uh \\ vh \\ \psi h \end{pmatrix}, \mathbf{E} = \begin{pmatrix} uh \\ u^2 h + gh^2/2 \\ uvh \\ \psi uh \end{pmatrix}, \mathbf{G} = \begin{pmatrix} vh \\ uv \\ v^2 h + gh^2/2 \\ \psi vh \end{pmatrix}, \mathbf{S} = \begin{pmatrix} S_p \\ -gh(S_{ox} + S_{fx}) + f_c vh \\ -gh(S_{oy} + S_{fy}) - f_c uh \\ \nabla \cdot (\mathbf{K} h \nabla \psi) + S_c \end{pmatrix} \tag{8}$$

with the empirical dispersion matrix

$$\mathbf{K} = \begin{pmatrix} K_{xx} & K_{xy} \\ K_{yx} & K_{yy} \end{pmatrix} \tag{9}$$

Bed slope is calculated using

$$S_{0x} = \frac{\partial z}{\partial x} \text{ and } S_{0y} = \frac{\partial z}{\partial y} \tag{10}$$

There are several equations available for friction slope calculation such as Darcy-Weisbach equation for laminar flow and Manning equation for turbulent flow. Here the friction slope is estimated by the Manning equation

$$S_{fx} = \frac{n^2 u \sqrt{u^2 + v^2}}{h^{4/3}} \tag{11}$$

$$S_{fy} = \frac{n^2 v \sqrt{u^2 + v^2}}{h^{4/3}} \tag{12}$$

with n = Manning coefficient.

The source term vector in the equations system (7) consists of three parts: bed slope $\mathbf{S_0}$, friction slope $\mathbf{S_f}$, pollutant diffusion $\mathbf{S_d}$, and the additional source/sink term $\mathbf{S_p}$:

$$\mathbf{S_0} = (0 \quad -ghS_{0x} \quad -ghS_{0y} \quad 0)^T$$

$$\mathbf{S_f} = (0 \quad -ghS_{fx} \quad -ghS_{fx} \quad 0)^T \tag{13}$$

$$\mathbf{S_d} = \begin{pmatrix} 0 & 0 & 0 & \nabla \cdot (\mathbf{K} h \nabla \psi) \end{pmatrix}^T$$

$$\mathbf{S_p} = \begin{pmatrix} S_p & f_c v h & -f_c u h & S_c \end{pmatrix}^T$$

Numerical Model

The domain decomposition method discussed in Chapter 2 is also used here to produce the unstructured triangular grids. Over each grid V_i, the system can be integrated as:

$$\int_{V_i} \frac{\partial \mathbf{U}}{\partial t} dV + \int_{V_i} \nabla \cdot \mathbf{F} dV = \int_{V_i} \mathbf{S} dV \tag{14}$$

Applying the Gauss theorem, the second integral on the left-hand side is replaced by a line integral around the control volume, which changes Equation (14) into:

$$\int_{V_i} \frac{\partial \mathbf{U}}{\partial t} dV + \oint_{\Gamma_i} \mathbf{F} \cdot \mathbf{n} d\Gamma = \int_{V_i} \mathbf{S} dV \tag{15}$$

with Γ =boundary of the control volume and $\mathbf{n} = (n_x \ n_y)^T$ = the unit outward vector normal to the boundary.

A cell-centered finite volume method is formulated for Equation (15) over a Delaunay-type triangle-shaped control volume, where the dependent variables of the system are stored at the center of the control volume and represented as piecewise constant. The association of these variables with the centers enables the implementation of a high-order interpolation scheme [Sleigh et al., 1998]. Using the mid-point rule to Equation (15), it can be rewritten as:

$$\frac{\partial \mathbf{U}_i}{\partial t} = -\frac{1}{V_i} \sum_{j=1}^{3} (\mathbf{F}_{ij} \cdot \mathbf{n}_{ij}) \Gamma_j + \mathbf{S}_i \tag{16}$$

with $\mathbf{U}_i$ being the average values over the control volume V_i, $\mathbf{S}_i = \frac{1}{V_i}\int_{V_i} \mathbf{S} dV$ being the numerical approximation of the source term, $\mathbf{n}_{ij}$ being the unit outward normal vector to the edge j, $\mathbf{F}_{ij}$ is the numerical flux vector through the edge j, which is calculated using the HLL approximate Riemann solver.

To solve the system in a fully-coupled mode using HLL scheme, the approach of Zoppou and Roberts [1999] is followed to manipulate the flux terms. The rotation matrix is introduced:

$$\mathbf{T_n} = \begin{pmatrix} 1 & 0 & 0 & 0 \\ 0 & n_x & n_y & 0 \\ 0 & -n_y & n_x & 0 \\ 0 & 0 & 0 & 1 \end{pmatrix} \tag{17}$$

The application of this matrix aligns the normal **n** with the x-axis. Using the rotational invariance property of the 2D shallow water equations, then:

$$\mathbf{F}(\mathbf{U}) \cdot \mathbf{n} = \mathbf{T}_n^{-1} \mathbf{E}(\mathbf{T}_n \mathbf{U}) \tag{18}$$

Applying Equation (18), Equation (15) becomes:

$$\int_{V_i} \frac{\partial \mathbf{U}}{\partial t} dV + \oint_{\Gamma_i} \mathbf{T}_n^{-1} \mathbf{E}(\mathbf{T}_n \mathbf{U}) d\Gamma = \int_{V_i} \mathbf{S} dV \tag{19}$$

Then Equation (16) becomes

$$\frac{\partial \mathbf{U}_i}{\partial t} = -\frac{1}{V_i} \sum_{j=1}^{3} \mathbf{T}_{n_{i,j}}^{-1} \tilde{\mathbf{E}}\left(\mathbf{T}_{n_{i,j}} \mathbf{U}_i, \mathbf{T}_{n_{i,j}} \mathbf{U}_j\right) \Gamma_j + \mathbf{S}_i \tag{20}$$

where $\tilde{\mathbf{E}}$ is the numerical flux vector through the edge j.

It is noted that the solution for h and u is unaffected by v and ψ, the complete solution of the Riemann problem for the conservative quantities h and uh in the 2D shallow water equations is identical o that for the 1D ones [Zoppou and Roberts, 1999; Toro, 2001]. The following formulations are used to calculate the normal fluxes for the conservative variables *h* and *uh*, which are also the first two components of the numerical flux $\widetilde{\mathbf{E}}$:

$$\widetilde{\mathbf{E}}_{1,2}(\mathbf{U}_L,\mathbf{U}_R)=\begin{cases}\mathbf{E}_L & \textit{if}\ \ S_L \geq 0\\ \dfrac{S_R\mathbf{E}_L - S_L\mathbf{E}_R + S_R S_L(\mathbf{U}_R - \mathbf{U}_L)}{S_R - S_L} & \textit{if}\ \ S_L \leq 0 \leq S_R\\ \mathbf{E}_R & \textit{if}\ \ S_R \leq 0\end{cases} \tag{21}$$

where $\mathbf{U}_L = \mathbf{T}_{n_{i,j}}\mathbf{U}_i$ and $\mathbf{U}_R = \mathbf{T}_{n_{i,j}}\mathbf{U}_j$, S_L and S_R are the wave speed estimates. Several formulations are available for calculation of S_L and S_R. The approach proposed by Toro [1992] is used here:

$$S_L = \begin{cases} min\left(u_L - \sqrt{gh_L}, u^* - \sqrt{gh^*}\right) & \text{if both sides are wet}\\ u_L - \sqrt{gh_L} & \text{if the right side is dry}\\ u_R - 2\sqrt{gh_R} & \text{if the left side is dry}\end{cases}$$

$$S_R = \begin{cases} min\left(u_R + \sqrt{gh_R}, u^* + \sqrt{gh^*}\right) & \text{if both sides are wet}\\ u_L + 2\sqrt{gh_L} & \text{if the right side is dry}\\ u_R + \sqrt{gh_R} & \text{if the left side is dry}\end{cases} \tag{22}$$

$$u^* = \frac{1}{2}(u_L + u_R) + \sqrt{gh_L} - \sqrt{gh_R}$$

$$h^* = \frac{\left(u_L - u_R + 2\left(\sqrt{gh_L} + \sqrt{gh_R}\right)\right)^2}{16g}$$

Finally, the normal flux for the conservative variable *uh* and ψh are calculated from:

$$\widetilde{\mathbf{E}}_3(\mathbf{U}_L,\mathbf{U}_R)=\begin{cases}\widetilde{\mathbf{E}}_1 v_L & \textit{if}\ \ u^* \geq 0\\ \widetilde{\mathbf{E}}_1 v_R & \textit{if}\ \ u^* < 0\end{cases} \tag{23}$$

and

$$\widetilde{\mathbf{E}}_4(\mathbf{U}_L, \mathbf{U}_R) = \begin{cases} \widetilde{\mathbf{E}}_1 \psi_L & if \;\; u^* \geq 0 \\ \widetilde{\mathbf{E}}_1 \psi_R & if \;\; u^* < 0 \end{cases} \tag{24}$$

where $\mathbf{E_1}$ is the normal flux calculated using (5) for the conservative variable *h*. $\mathbf{E_3}$and $\mathbf{E_4}$ are the third and fourth components of $\mathbf{E}(\mathbf{U_L}, \mathbf{U_R})$ respectively.

Source Terms

The source term vector consists of bed slope, pollutant diffusion, and friction slope. It is of great importance to correctly treat the source terms in order to obtain accurate results.

Bed Slope

For the treatment of bed slope, there have been a few discussions in the literature [e.g., Bermudez and Vazquez-Cendon, 1994; Bermudez et al., 1998; Leveque, 1998; Zhou et al., 2001; Bradford and Sanders, 2002; Delis, 20003]. In this paper, the triangular grids facilitate the computation of the bed slope. Denote (x_i, y_i, z_i) as local coordinates associated with vertex *i* of a certain triangle grid, where z_i is the bed elevation (Fig 2).The plane is defined by

$$\begin{vmatrix} x & y & z & 1 \\ x_1 & y_1 & z_1 & 1 \\ x_2 & y_2 & z_2 & 1 \\ x_3 & y_3 & z_3 & 1 \end{vmatrix} = 0 \tag{25}$$

or $z = ax + by + c$ in compact form with *a* and *b* = the coefficients. Now, the slopes of the triangular grid are simply calculated as:

$$S_{0x} = \frac{\partial z}{\partial x} = a = \frac{y_1(z_3 - z_2) + y_3(z_2 - z_1) + y_2(z_1 - z_3)}{x_3(y_1 - y_2) + x_1(y_2 - y_3) + x_2(y_3 - y_1)} \tag{26}$$

$$S_{0y} = \frac{\partial z}{\partial y} = b = -\frac{x_1(z_3 - z_2) + x_3(z_2 - z_1) + x_2(z_1 - z_3)}{x_3(y_1 - y_2) + x_1(y_2 - y_3) + x_2(y_3 - y_1)} \tag{27}$$

In order to alleviate the numerical errors in still water situations, a combination of two techniques is used. Firstly, the water surface elevation (*H*) instead of the water depth (*h*) is reconstructed. The water depth values at left and right sides of an edge are calculated by subtracting the corresponding bed elevation from water surface elevation. This can prevent the strong depth fluctuations due to the arbitrary bed geometry [Farshi and Komaei, 2004]. In next step, the approach suggested by Bradford and Sanders [2002] is used in the calculation of the bed slope term:

$$\int_{V_i} ghS_{0x} dV = \left(H \left.\frac{\partial z}{\partial x}\right|_i - \frac{1}{2} \left.\frac{\partial z^2}{\partial x}\right|_i \right) V_i \tag{28}$$

Diffusion Source Term

The integral of the diffusion term is modified by applying the Gauss theorem:

$$\int_{V_i} \nabla \cdot (\mathbf{K} h \nabla \psi) dV = \oint_{\Gamma_i} (\mathbf{K} h \nabla \psi) \cdot \mathbf{n} d\Gamma \tag{29}$$

This line integral is approximated by:

$$\oint_{\Gamma_i} (\mathbf{K} h \nabla \psi) \cdot \mathbf{n} d\Gamma = \sum_{j=1}^{3} (\mathbf{K} h \nabla \psi)_{ij} \cdot \mathbf{n}_{ij} \Gamma_j \tag{30}$$

$(\mathbf{K} h \nabla \psi)_{ij}$ can be approached by:

$$(\mathbf{K} h \nabla \psi)_{ij} = (\mathbf{K}(\nabla \psi h - \psi \nabla h))_{ij} \approx \frac{\mathbf{K}_L + \mathbf{K}_R}{2} \left((\nabla \psi h)_j - \min(\psi_L, \psi_R)(\nabla h)_j \right) \tag{31}$$

where $(\nabla \psi h)_j$ and is the face gradient calculated during the linear reconstruction. *h* is evaluated as $\min(\psi_L, \psi_R)$ in order to avoid diffusion in dry/wet edges.

Friction Slope

Friction slope is discretized in a point-wise manner, say, evaluated at the centroid.

Time Integration

If a purely explicit scheme is used to solve the equations system (20), the stability is determined by the combination of advection and diffusion. It is well known that the time step is restricted by Courant–Friedrichs-Lewy (*CFL*) number and the Peclet (*Pe*) number, so that

$$CFL + Pe \leq 1 \tag{32}$$

with

$$CFL = \frac{2\max\left(\left(\sqrt{u^2+v^2}+c\right)_i\right)}{\min\left(d_i\right)}\Delta t_{CFL} \tag{33}$$

$$Pe = \frac{\max\left(\mathbf{K}*\mathbf{n}\right)_{i,j}}{2\min\left(l_i^2\right)}\Delta t_{Pe} \tag{34}$$

where i is the cell index and j denotes the edge, d_i represents the whole set of distances between the ith centroid and the those of its neighboring cells, and $l_i = \min\left(V_i / \Gamma\right)_j$.

In order to reduce the numerical instabilities related to the friction slope when the water depth is very small and circumvent the time constraint by Peclet number, a semi-implicit method is used. The system can be split into two ordinary differential equations:

$$\frac{\partial \mathbf{U}_i}{\partial t} = -\frac{1}{V_i}\sum_{j=1}^{3}\left(\mathbf{F}_{ij}\cdot\mathbf{n}_{ij}\right)\Gamma_j + \mathbf{S}_{\mathbf{0}i} \tag{35}$$

$$\frac{\partial \mathbf{U}_i}{\partial t} = \mathbf{S}_{\mathbf{f}i} + \mathbf{S}_{\mathbf{di}} \tag{36}$$

The right hand side (RHS) of Equation (35) consists of advection and bed slope source term while the RHS of Equation (36) includes friction slope and pollutant diffusion source terms. In the first step, Equation (35) is solved by an explicit method as described below. In next step, using the values obtained from the first step as the initial conditions, Equation (36) is solved using an implicit method (BDF) provide by an advanced ODE solver CVODE [Hindmarsh and Serban, 2005].

The explicit time integration is performed by the first-order Euler method or a total variation diminishing (TVD) Runge-Kutta method [Shu and Osher, 1988] which have been used in many literatures thanks to its stability and high-order accuracy (third-order):

$$\begin{aligned} \mathbf{U}_1 &= \mathbf{U}^n + \Delta t \mathrm{f}\left(\mathbf{U}^n\right) \\ \mathbf{U}_2 &= \frac{3}{4}\mathbf{U}^n + \frac{1}{4}\mathbf{U}_1 + \frac{1}{4}\Delta t \mathrm{f}\left(\mathbf{U}_1\right) \\ \mathbf{U}^{n+1} &= \frac{1}{3}\mathbf{U}^n + \frac{1}{3}\mathbf{U}_2 + \frac{2}{3}\Delta t \mathrm{f}\left(\mathbf{U}_2\right) \end{aligned} \tag{37}$$

where f is the right hand side of Equation (35).

Since the explicit scheme is only applied to advection, the time step is limited by *CFL* condition. Therefore, an adaptive Δt is used in the model according to the formula

$$\Delta t \le \frac{\min\left(d_i\right)}{2\max\left(\left(\sqrt{u^2+v^2}+c\right)_i\right)} \tag{38}$$

Boundary Conditions

Two types of boundaries, open boundary and solid wall boundary, are considered in the model. Details of their implementation were discussed in Chapter 2.

Results and Discussion

In order to test the stability and accuracy of the model, it has been applied in three test cases. The first one solves a pollutant transport in a square cavity, which is used to validate model in simulating pollutant advection. The second test case involves a microscale pollutant transport scenario following an asymmetric dam break. The objective of this test case is to test the ability of the model in prediction pollutant transport by shocks or sharp fronts under different magnitude of diffusion. The third one is a mesoscale application, i.e., modeling pollutant transport by tidal flow and storm surge in Galveston Bay off the coast of Texas during hurricane Ike.

Advection of Pollutant in a Square Cavity

The first example is about the advection-dominant pollutant transport ($\mathbf{K} = \mathbf{0}$) in a square cavity with smooth topography [Komatsu et al., 1997], which is used to validate the model. The computational domain is a 9 kilometer by 9 kilometer square channel with the Manning's roughness of 0.025 s/m$^{1/3}$ and the bed slope $S_{0x} = S_{0y} = -0.001$. The domain was decomposed into 85264 triangles. Initially, the uniform flow conditions were imposed on the whole domain, i.e., $u = v = 0.5$ m/s and $h = 0.2485$ m. The initial pollutant concentration was given by the superposition of two Gaussian distribution:

$$\psi(0,x,y) = \psi_1 \exp\left(-\frac{(x-x_1)^2 + (y-y_1)^2}{\delta_1^2} \right) + \psi_2 \exp\left(-\frac{(x-x_2)^2 + (y-y_2)^2}{\delta_2^2} \right) \tag{39}$$

with $x_1 = y_1 = 1400$ m, and $x_2 = y_2 = 2400$ m, $\psi_1 = 10$ and $\psi_2 = 6.5$, and $\delta_1 = \delta_2 = 264$. The free outfall or transmissive flow conditions were applied at all the boundaries. Analytically the pollutant concentration moves along the diagonal ($x = y$) of the domain at the constant speed $u = v = 0.5$ m/s with its shape preserved.

Figure 3-1 shows the contour maps of pollutant concentration at three simulation times *t* = 1628, 5235, and 9600 s. The profiles of pollutant concentration are given in Figure 3-2. Close examination of the results indicates that the shape of pollutant plume was preserved fairly well. A further comparison with the published simulations of SRNH [Benkhaldoun et al., 2007] demonstrates the performance of this model is satisfactory with the error of -9.0% for the maximum concentration (Table 1). The accuracy of this model is almost same with that of SRNH on the fixed meshes. The advantage of this model is that it is easy to implement. The numerical results, however, are still affected by numerical diffusion as the simulation time increases. Overall, this simulation is convincing confirmation of the model's ability to predict advection of pollutant by shallow water flow.

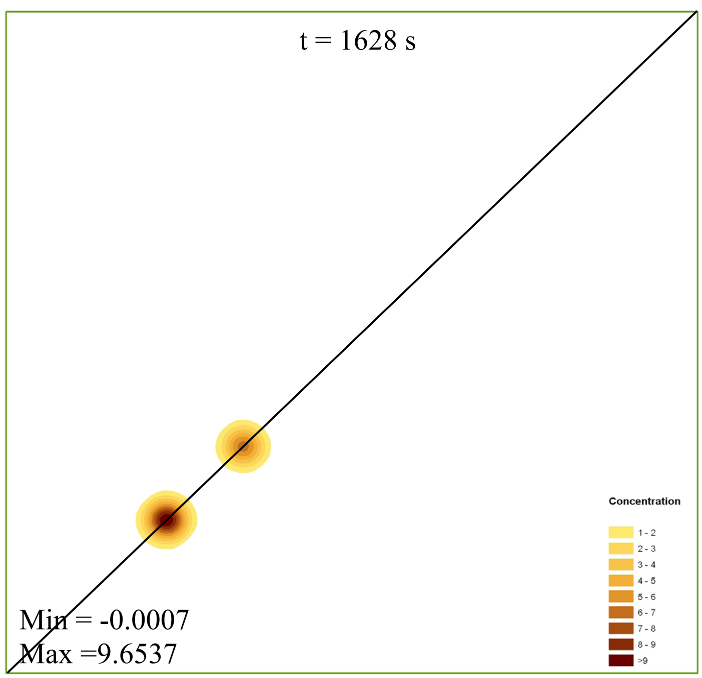

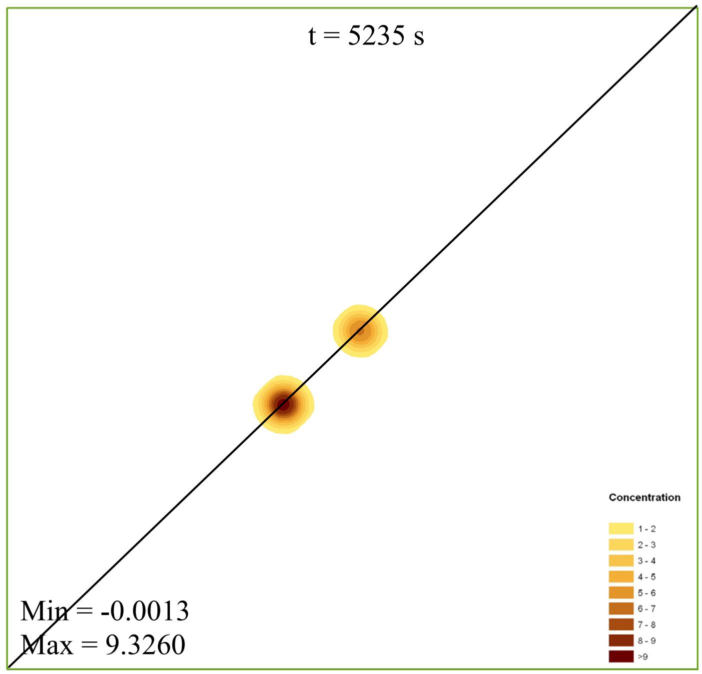

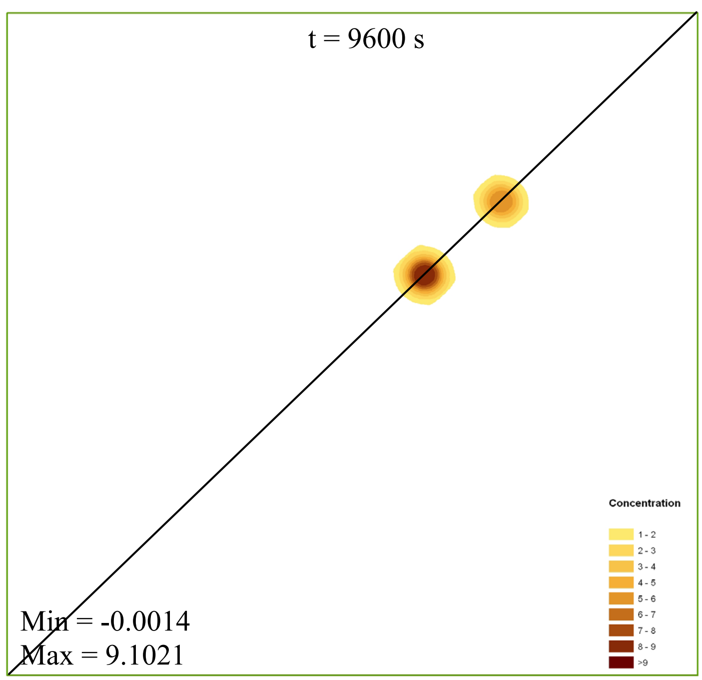

Figure **3-1**: Spatial distributions of pollutant concentration over the square cavity at three simulation times.

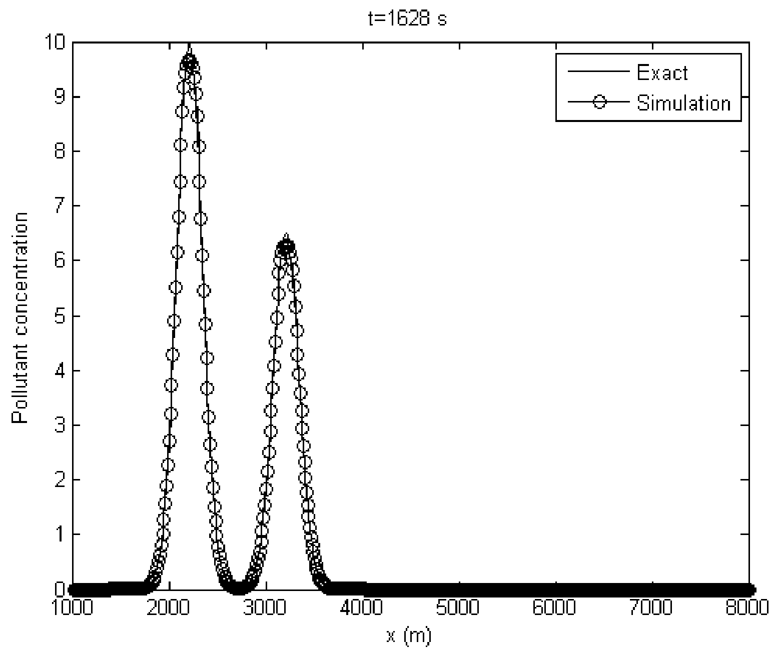
t=1628 s
Exact
Simulation
Pollutant concentration
x (m)
0
1
2
3
4
5
6
7
8
9
10
1000
2000
3000
4000
5000
6000
7000
8000

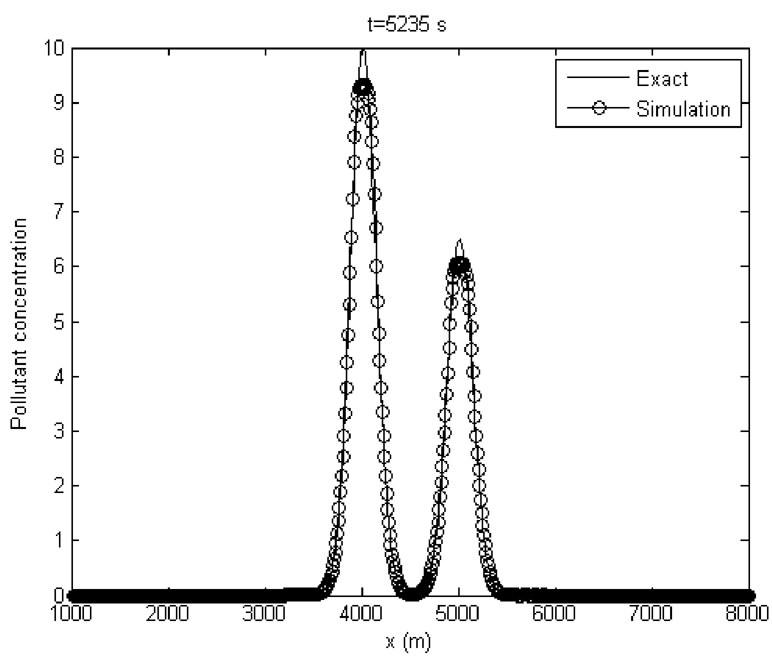
t=5235 s
Exact
Simulation
Pollutant concentration
x (m)
0
1
2
3
4
5
6
7
8
9
10
1000
2000
3000
4000
5000
6000
7000
8000

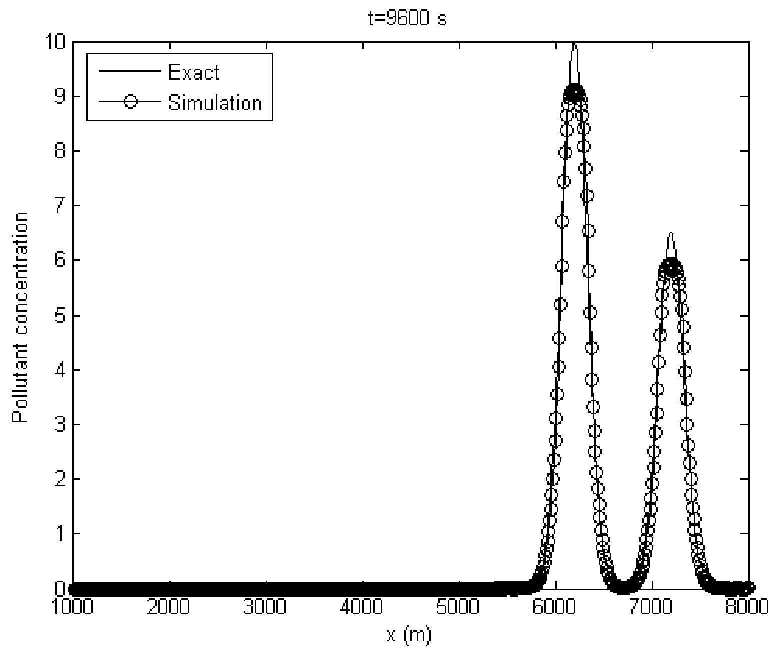

Figure **3-2**: Pollutant concentrations along the diagonal of the square cavity at three simulation times.

Table **3-1**: Comparison of this model with the exact solutions and the SRNH scheme with Van Albada limiter for the pollutant transport in a square cavity at t = 9600 s.

	Exact	SRNH	Model
# of elements		85504	85264
# of nodes		43073	42749
Minimum of concentration	0.0	-0.0054	-0.0014
Maximum of concentration	10.0	9.12 (-8.8%)	9.10 (-9.0%)

Pollutant Transport Following an Asymmetric Dam Break

This is a microscale test case used to demonstrate the capability of the model in predicting pollutant transport by shocks or sharp fronts under different magnitude of diffusion. This example was adapted from Murillo et al. [2005]. The laboratory set-up plan view is shown in Figure 3-3 with flat bed ($S_{0x} = S_{0y} = 0$) and a Manning roughness of 0.01 s/m$^{1/3}$. The computational domain was decomposed into 2330 triangles. Initially the flow depth was set to 0.5 m and 0.1 m respectively at the lower and upper half which were separated by a gate (dam) shown in Figure 3-3. Flow velocities were set to zero. The initial concentration is a circular step distribution around the gate, defined as:

$$\psi(x,y,0)=\begin{cases}2 & if\ \ r\geq r_0\\ 1 & if\ \ r<r_0\end{cases}\ \text{with}\ r=\left((x-1.97)^2+(x-1.35)^2\right)^{\frac{1}{2}}\ \text{and}\ r_0=0.65\ \text{m} \tag{46}$$

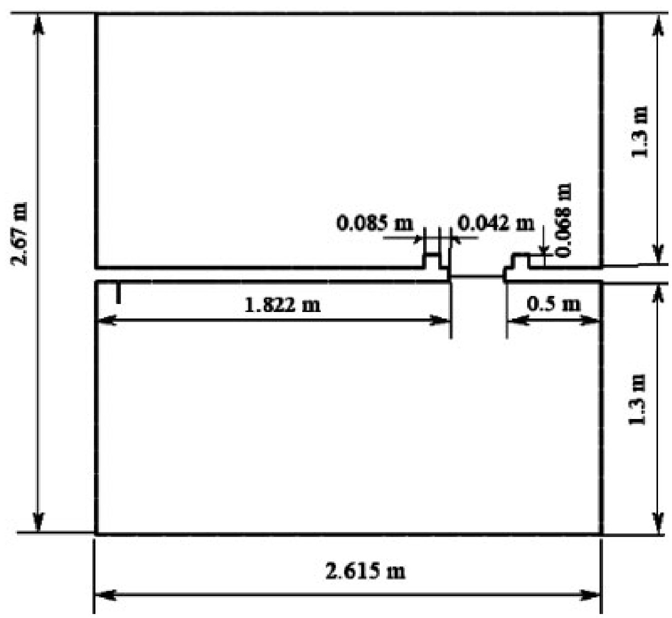

Figure **3-3**: Plan view of the laboratory set-up of the asymmetric dam break experiment (from Murillo et al. [2005]).

Three numerical experiments were conducted with different dispersion coefficients: (1) $\mathbf{K}=\begin{pmatrix}0 & 0\\ 0 & 0\end{pmatrix}$, (2) $\mathbf{K}=\begin{pmatrix}0.01 & 0\\ 0 & 0.01\end{pmatrix}$, and (3) $\mathbf{K}=\begin{pmatrix}1 & 0\\ 0 & 1\end{pmatrix}$. Figure 3-4 shows the numerical results. In the advection-dominant case (e.g., $\mathbf{K}=\mathbf{0}$), the pollutant concentration varies remarkably across the domain. At t = 15 s, the concentration varies from 1 to 1.9. In the second experiment, the dispersion effect is included. The spatial variations of pollutant concentration diminished. In the third test case where the dispersion was dominant, the pollutant concentration is almost same across the domain in a short period of time, say, $t = 5$ s. One advantage of this model is that the time step is not restricted by the Peclet number by implicit treatment of the diffusion term.

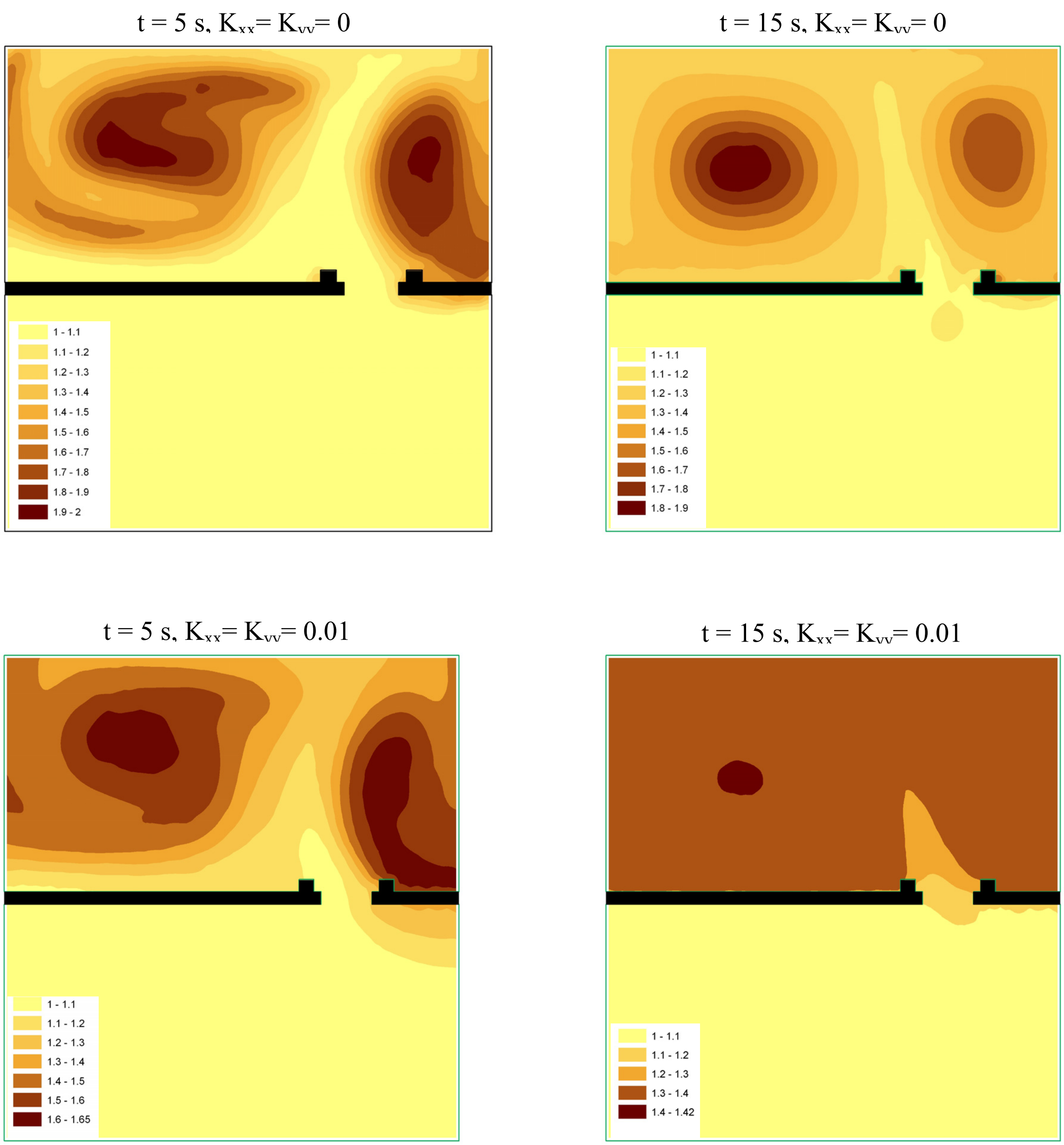

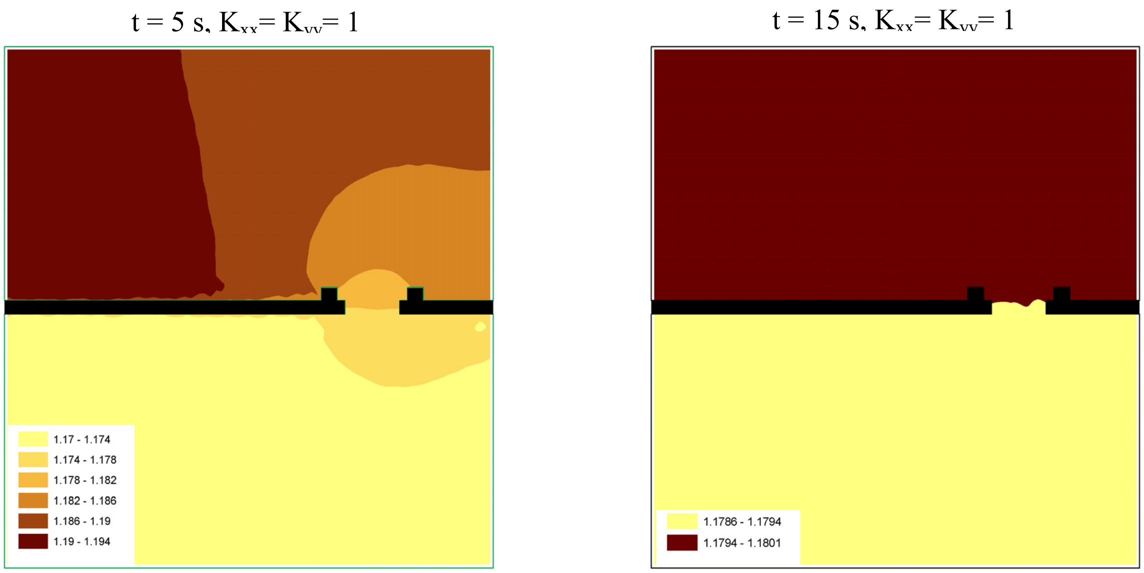

Figure **3-4**: Spatial distribution of pollutant concentration following an asymmetric dam break under different magnitude of dispersion.

Pollutant Transport in Galveston Bay

This test case involves a contamination scenario in Galveston Bay of Texas, which connects the Port of Houston and the Gulf of Mexico. It is used to demonstrate the capabilities of the model in predicting the mesoscale flow and pollutant dynamics driven by a storm surge and tidal flow. The area of the bay is about 2805 km^2 and its bathymetry is shown in Figure 3-5. The domain is quite complicated with respect to both geometry and topography. There are 17 islands included in the domain, and the bathymetry varies from very deep in the coastal area and the Houston ship channel to very shallow within the bay.

The domain is decomposed into 3397 triangles (Figure 3-5) with the structure slightly different from the one used in Aizinger and Dawson [2002]. Following Aizinger and Dawson [2002], the bottom friction coefficient was set as 0.004. The Coriolis parameter was 7.07E-5 according to Equation (5). The solid wall boundary condition was imposed on the land and island boundaries. An open boundary condition was applied at the interface between the bay and the Gulf of Mexico as shown in Figure 3-5. The measured tidal data from 0:00 of September 1 to 19:00 of September 15, 2008 (local time) at the Galveston Pleasure Pier, TX (http://tidesandcurrents.noaa.gov/) was used. The tidal elevations were influenced by Hurricane Ike during September 12 and 13 as can be observed in Figure 3-6. It is also noted that there were several unusually high spikes on September 8, 9 and 15 with very short duration, which may be caused by the measurement errors. At 19:00 of day 6, a pollutant source was placed at a point (3.28E+5, 3.25E+6) meters of the ship channel, with a steady rate of 500 m^3/s.

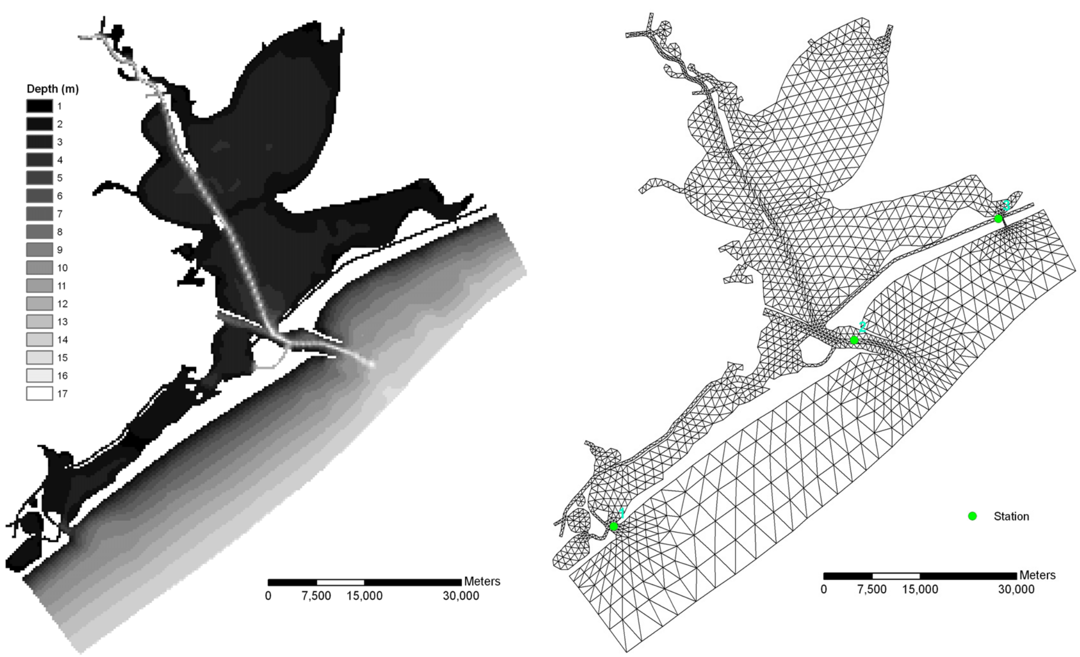

Figure **3-5**: The bathymetry (left) and computational mesh (right) of the Galveston Bay. The green points represent three stations where the simulation is done.

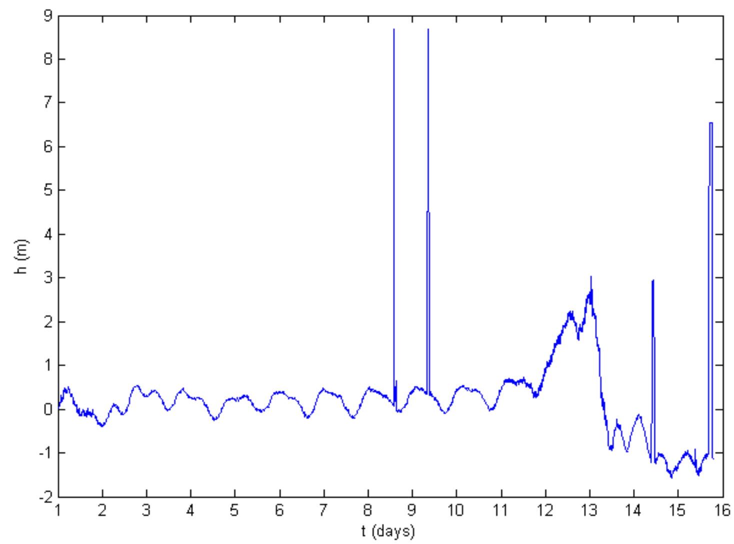

Figure **3-6**: Time series of water elevations at the open boundary. Note that the spikes are measurement errors since the NOAA tide gauge data was not verified at the time the model was developed and were not removed for the simulation

Figure 3-7 shows the predicted elevations and pollutant concentration from day 6 to day 15 at three locations, Station 1 (2.94E+5, 3.22E+6), Station 2 (3.31E+5, 2.25E+6), and Station 3 (3.53E+5, 3.27E+6) meters (Figure 3-5). Station 1 is located at the narrow inlet from the Gulf in the bottom left of the domain. Station 2 is at the inlet in the deep ship channel from Gulf to the Galveston Bay. Station 3 is located at a shallow narrow channel within the bay in the bottom right of the domain. The results indicate a phase lag of approximately 1.2 hours between the open boundary and the three locations, which is consistent to the observations by NOAA (http://tidesandcurrents.noaa.gov/). The phase lags between these three stations are negligible which are reasonable based on the uniform boundary conditions and the similar distances between the open boundary and the station.

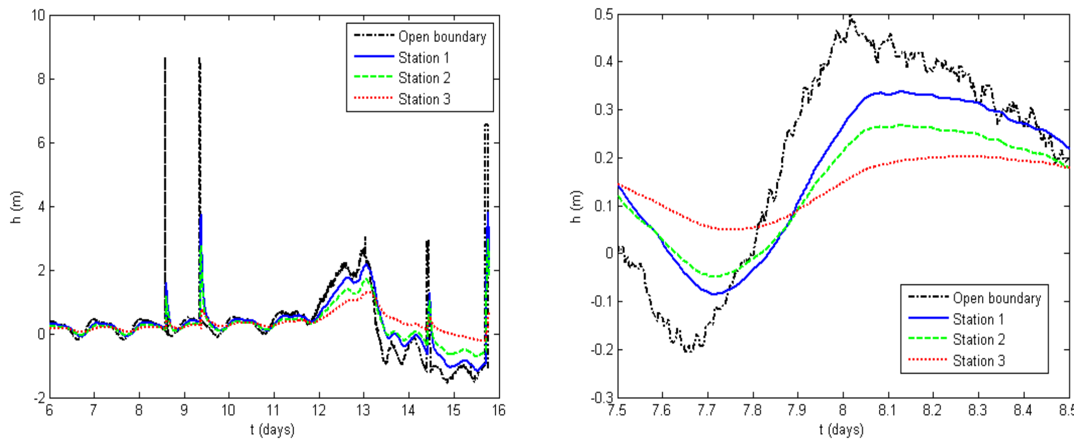

Figure **3-7**: Time series of predicted water elevations from day 6 to day 15 (left) at the 3 stations. The zoom-in figure on the right shows the temporal variation of water surface elevations in 1 day.

Additional insight into the flow dynamics is gained by considering the spatial distribution of water surface elevation and pollutant over the entire domain. Figures 3-8 (a), (b) and (c) show three snapshots of the water surface elevations at different computational times. Figure 3-8 (a) shows the middle of an ebb tide. The tides are relatively low out in the Gulf, somewhat higher in the middle part of the bay, and even higher in bottom left of the bay which is due to the narrow outlets to the other parts of the bay and the Gulf. The variation in tidal amplitude becomes fairly small within the bay. Figures 3-8 (b) and (c) are two snapshots of the tidal elevation at the middle and peak of a flood tide during the Hurricane Ike. The tidal waves were still progressing up into the bay, with the water surface elevation much higher than normal tidal cycles. As can be observed in Figure 3-8 (c), the water surface elevations were between 0.5 m to 1 m in most parts of the bay.

Corresponding to the times for the figures on the left of Figure 3-8, three snapshots are shown on the figures on the right to demonstrate the spread of pollutant caused by tidal flow. It is easy to see that the storm surge caused by the Hurricane Ike significantly extended the polluted area. The comparison between the polluted area before the Hurricane (Figure 3-9 (a)) and after

(Figures 3-9 (b) and (c)) indicates the storm surge propagated the pollutant much deeper into the Bay and out to the Gulf. The experiment shows that the model is very stable and robust in simulating the mesoscale flow dynamics and pollutant transport driven by storm surge.

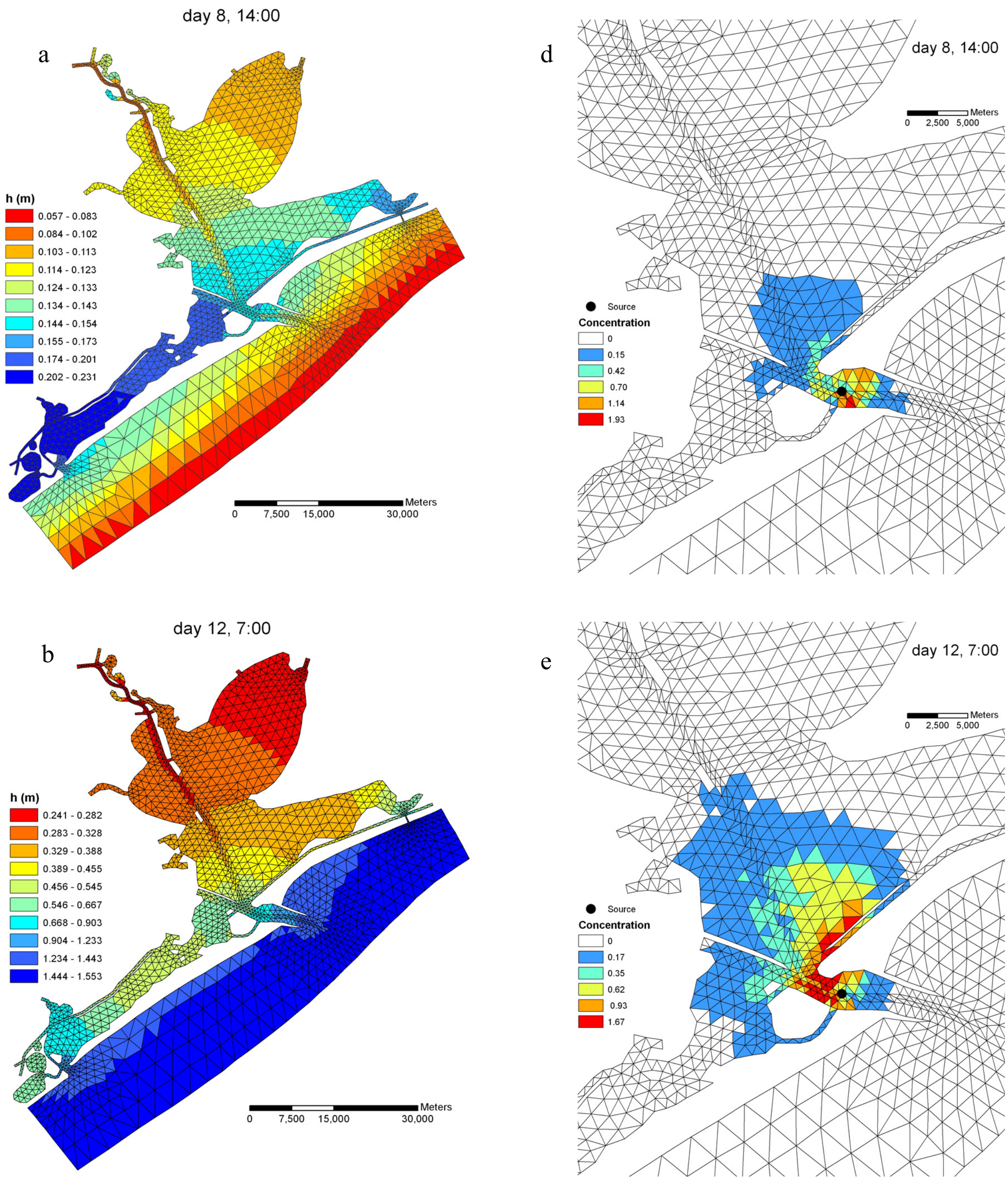

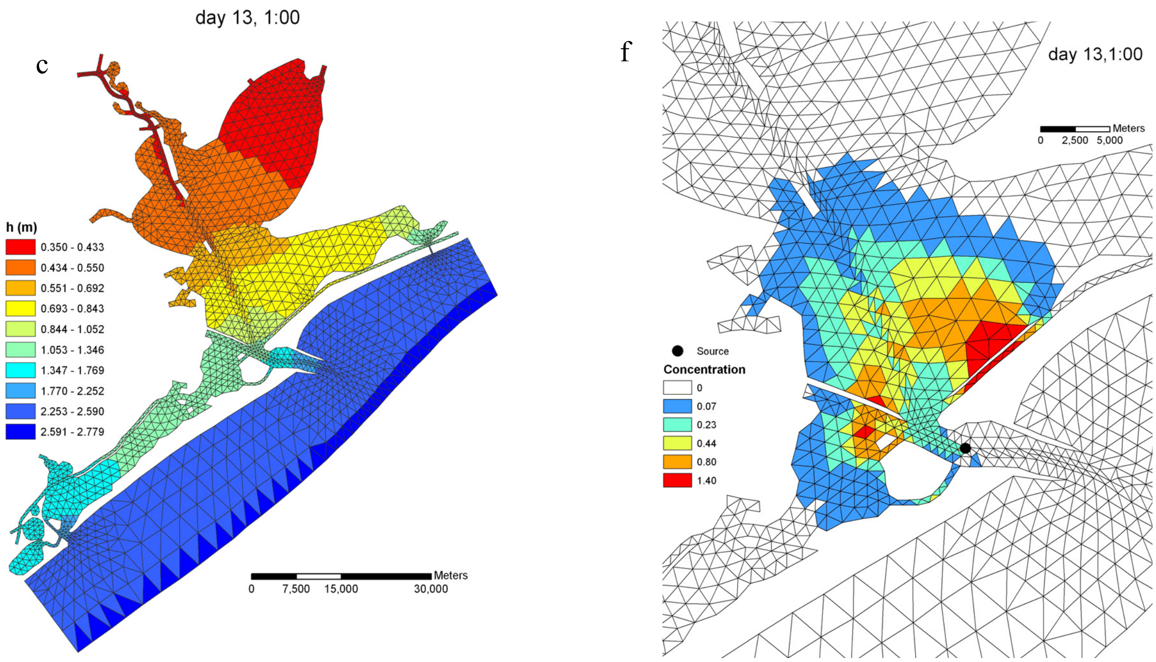

Figure **3-8**: Spatial distribution of predicted water elevations (left) and pollutant concentrations (right) over Galveston Bay at 3 computational times as indicated, i.e., before the storm surge and during storm surge.

Conclusions

In this study, a fully-coupled model of shallow water flow and pollutant transport was developed as an important module of PIHM-Hydro and tested over a range of physical and numerical conditions. The model is based on a cell-centered upwind finite volume method using the HLL approximate Riemann solver. The multidimensional linear reconstruction technique and multi-dimensional slope limiter discussed in Chapter 2 were also used here to achieve a second-order spatial accuracy.

The advantages of this model are that (1) it is capable of accurately simulating the pollutant transport by shallow water flow by fully coupling these processes physically and numerically; and (2) the time step is not restricted by the Peclet number by implicit treatment of the diffusion term. As a module of the PIHM-Hydro modeling system, this model also shows its advantages as discussed in Chapter 2 in terms of handling complicated geometry by using the Delaunay triangulation based on Shewchuk's algorithm, and producing accurate and stable solutions over a wide range of spatial scales and hydrological events such as dam break and storm surge stably by using the approximate Riemann solver and the semi-implicit time integration technique based on the CVODE.

The model has been applied to various cases across multiple scales. The test case of pollutant transport in a square cavity shows the model can predict advection of pollutant by shallow water flow very well. Application of the model in a microscale pollutant transport following dam break compared the effects of advection and dispersion on pollutant transport, and show the advantage of the model in that the implicit treatment of the diffusion term makes it stable and it time step restricted by the Peclet number. The model is further applied to a mesoscale experiment about pollutant transport in Galveston Bay. This test case shows that the model is very stable and robust in simulating the mesoscale flow dynamics and pollutant transport driven by storm surge. It also indicates that he storm surge caused by the Hurricane Ike significantly extended the polluted area.

References

[111] Aizinger,V. and C. Dawson. 2002. A discontinuous Galerkin method for two-dimensional flow and transport in shallow water. Advances in Water Resources, 25: 67-84.

[112] Akanbi, A.A. and N. D. Katopodes. 1988. Model for flood propagation on initially dry land. Journal of Hydraulic Engineering, 114 (7): 689-706.

[113] Benkhaldoun, F., I.Elmahi,and M.Seaid. 2007. Well-balanced finite volume schemes for pollutant transport by shallow water equations on unstructured meshes. Journal of Computational Physics, 226: 180-203.

[114] Bermudez, A. and M.E. Vázquez-Cendón. 1994. Upwind methods for hyperbolic conservation laws with source terms. Computers and Fluids, 23 (8):1049-1071.

[115] Bermudez, A., A. Dervieux, J.A. Desideri, and M.E. Vazquez. 1998. Upwind schemes for the two-dimensional shallow water equations with variable depth using unstructured meshes.Comput. Meth. Appl. Mech. Eng., 155: 49-72.

[116] Bradford, S.F. and B.F. Sanders. 2002. Finite-volume model for shallow-water flooding of arbitrary topography. Journal of Hydraulic Engineering, 128: 289-298

[117] Delis, A.I. 2003. Improved application of the HLLE Riemann solver for the shallow water equations with source terms. Commun. Numer. Meth. Eng., 19:59-83.

[118] Farshi, D. and S. Komaei. 2005. Discussion of "Finite Volume Model for Two-Dimensional Shallow Water Flows on Unstructured Grids" by Tae Hoon Yoon and Seok-Koo Kang. Journal of Hydraulic Engineering, 131 (12): 1147-1148.

[119] Harten, A., P. D. Lax, and B.van Leer. 1983. On upstream differencing and Godunov-type schemes for hyperbolic conservation laws. SIAM Rev., 25 (1): 35-61.

[120] Hindmarsh and Serban. 2005. User Documentation for cvode v2.3.0. Center for Applied Scientific Computing Lawrence Livermore National Laboratory, UCRL-SM-208108.

[121] Horritt, M.S. 2000. Calibration and validation of a 2-dimensional finite element flood flow model using satellite radar imagery. Water Resources Research, 36 (11): 3279-3291.

[122] Jawahar, P., and H. Kamath. 2000. A high-resolution procedure for Euler and Navier-Stokes computations on unstructured grids. Journal of Computational Physics, 164: 165-203.

[123] Katopodes, N. and T. Strelkoff. 1978. Computing two-dimensional dam-break flood waves. Journal of the Hydraulics Division, ASCE 104: 1269-1288.

[124] Komatsu, T., K. Ohgushi, and K. Asai, 1997. Refined numerical scheme for advective transport in diffusion simulation. J. Hydraulic Eng. 123: 41–50.

[125] LeVeque,R.J. 1998. Balancing source terms and flux gradients in high resolution Godunov methods, J Comput Phys, 146: 346-365.

[126] Liggett, J.A. 1994. Fluid Mechanics. McGraw-Hill.

[127] Loukili, Y. and A.Soulaimani. 2007. Numerical Tracking of Shallow Water Waves by the Unstructured Finite Volume WAF Approximation.International Journal for Computational Methods in Engineering Science and Mechanics,8 (2): 75-88.

[128] Molls, T. and M.H. Chaudhry. 1995. Depth averaged open channel flow model. Journal of Hydraulic Engineering, 121: 453-465.

[129] Murillo, J., J. Burguete, P. Brufau, abdP. García-Navarro. 2005. Coupling between shallow water and solute flow equations: analysis and management of source terms in 2D. International Journal for Numerical Methods in Fluids, 49 (3): 267-299.

[130] Osher, S., and F. Solomon. 1982. Upwind difference schemes for hyperbolic conservation laws. Math. Comput., 38: 339-374.

[131] Shu, C. W., and S. Osher. 1988. Efficient implementation of essentially non-oscillatory shock capturing schemes. J. Comput. Phys., 77: 439-471.

[132] Sleigh, P.A., M. Berzins, P.H. Gaskell and N.G. Wright. 1998. An unstructured finite-volume algorithm for predicting flow in rivers and estuaries. Computers and Fluids, 27 (4): 479-508.

[133] Tan, W.Y. 1992. Shallow Water Hydrodynamics, Elsevier, New York.

[134] Toro, E.F. 1992. Riemann problems and the WAF method for solving the two-dimensional shallow water equations. Philos. Trans. R. Soc. London, Ser. A, 338: 43-68.

[135] Toro, E.F. 2001. Shock-capturing Methods for Free-surface Shallow Flows. John Wiley & Sons: Chichester.

[136] Zhou, J.G., D.M. Causon, C.G. Mingham, and D.M. Ingram. 2001.The Surface Gradient Method for the Treatment of Source Terms in the Shallow-Water Equations. J Comput Phys,168: 1-25.

[137] Zoppou, C. and S. Roberts. 1999. Catastrophic collapse of water supply reservoirs in urban areas. Journal of Hydraulic Engineering, 125: 686-695.

Chapter 4

INTEGRATED MODELING OF HYDROLOGY AND SEDIMENT TRANSPORT AT WATERSHED SCALES

Abstract

The Penn State Integrated Hydrologic Model (PIHM) is a spatially-distributed physically-based hydrological modeling system for multi-process simulation [Qu and Duffy, 2007]. In this study, a physically-based non-equilibrium non-uniform sediment transport modeling component (PIHM-Sed) was developed and added to PIHM at the watershed scale. It integrates sediment transport for hillslope and channel processes, including the effects of surface/subsurface hydrological processes on hydrologic performance and sediment yield and the spatial distribution of erosion/deposition. At the hillslope scale (10-1000 m), the erosion processes by rain splash and overland flow, and sediment transport by overland flow are simulated; for the channel, the erosion of bed material and sediment transport by channel flow is simulated. An algorithm for bed armoring was also implemented in the channel component. In the model system, all hydrological and sediment transport processes are defined on discretized unit elements as a fully-coupled system of ordinary differential equations (ODEs) using a semi-discrete finite volume method (FVM) on unstructured grids. The implementation of PIHM-Sed has been performed on a hypothetical storm event at the Shale Hill watershed for demonstrating the capability of the model in multi-process simulation at watershed scale.

Introduction

From a physical point of view, sediment transport is a consequence of hydrologic processes operating over a wide range of time scales. In fact, the two processes are so interrelated that sediment transport cannot be modeled without flow modeling.

There has been considerable work studying the linkage between hydrology and erosion [Horton, 1945; Bennett, 1974; Kirkby, 1978; Wischmeier and Smith, 1978; Beasley et al., 1980; Knisel, 1980; Ross et al, 1980; Park et al., 1982; Simons et al., 1982; Storm et al, 1987; Lane et al., 1988; Woolhiser et al., 1990; Gerits et al., 1990; Wicks and Bathurst, 1996; Morgan et al., 1998; Merritt et al., 2003; Heppner et al., 2006, 2007] and not to mention a huge amount of research on in-stream sediment transport [Bennett and Nordin, 1977; Han, 1980; Chang, 1982; Thomas, 1982; Armanini and Di Silvio, 1988; Holly and Rahuel, 1990; Spasojevic and Holly, 1990; Wu et al., 2000; Cao et al., 2002; Wu, 2004; Wu et al., 2004].

With advance in technology and a deeper understanding in the physics of hydrology, new strategies to characterize hydrologic responses have been put forward. Of particular note is the integrated hydrologic modeling [Abbot, 1986a; Abbot, 1986b; VanderKwaak, 1999; Panday and Huyakorn, 2004; Qu and Duffy, 2007]. According to Heppner et al. [2006, 2007], subsurface flow not only contributes to the surface flow but also affects erosion. Where the hydrologic processes and the sediment transport processes interact so frequently and intensively, it is difficult if not impossible to understand and predict hydrologic behavior unless they are considered as parts of an integrated system. The Penn State Integrated Hydrologic Model (PIHM) provides an integrated modeling framework for multi-process multi-scale watershed simulation using the semi-discrete finite volume method [Qu and Duffy, 2007]. It provides better representation of hydrology and may improve the performance of modeling on both hydrology and sediment transport. Table 1 compares the PIHM-Sed with other physically-based hydrology and sediment transport models. It clearly shows that the PIHM provides a sound hydrologic modeling framework for sediment transport modeling. The primary objective of this paper is to develop a physically-based sediment transport modeling component (PIHM-Sed) for PIHM to predict erosion and sediment transport at the watershed scale. Table 4-1 briefly shows this framework that represents the processes and their interaction more faithfully by physical and numerical coupling. The model has been tested in a hypothetical storm event at the Shale Hill watershed.

Table **4-1**: Characteristics of selected physically-based models of hydrology and sediment transport. Notations: 1D (one dimension), 2D (two dimension), U (unsaturated), S (saturated), U/S (unsaturated/saturated), KW (kinematice wave), DW (diffusion wave), SQ (sequential), FO (first-order).

Model	Hydrologic Processes				Sediment Transport		Hydrology-Sediment Coupling
	Subsurface	Overland	Channel	Hydrological Coupling	Overland	Channel	
KINEROS2	1D, U	1D, KW	1D, KW	SQ	1D	1D	SQ
SHESED	1D, U; 2D, S;	2D, DW	1D, DW	SQ	2D	1D	SQ
InHM	3D, U/S	2D, DW	2D, DW	FO	2D	2D	SQ
PIHM-Sed	2D, U/S	2D, KW/DW	1D, KW/DW	FO	2D	1D	FO

Methodology

PIHM is a multi-process, multi-scale hydrologic model where the major hydrological processes are fully coupled using the semi-discrete finite volume method (FVM) on unstructured triangular grids (TIN) including evaporation, interception, snowmelt, overland flow, river flow, subsurface flow and macropore flow [Qu and Duffy, 2007]. PIHM has been successfully applied to watersheds of different scales [Qu and Duffy, 2007] and provides a sound hydrological framework for sediment transport modeling. The numerical coupling strategy is presented below, followed by the modeling framework.

Semi-Discrete FVM approach

PIHM uses a semi-discrete finite volume formulation for coupling hydrologic processes [Qu and Duffy, 2007]. It discretizes rivers into linear elements, and the watershed into Delauney triangular elements that are generated by the domain decomposition method discussed in Chapters 2 and 3. A general form of the mass conservation equation for an arbitrary scalar variable χ can be described by the partial differential equation (PDE):

$$\frac{\partial \chi}{\partial t} + \nabla \cdot (\chi \mathbf{U}) + \frac{\partial (\chi w)}{\partial z} = S_{\chi} \tag{1}$$

where χ denotes the mass fraction of storage (dimensionless). The velocity vector is divided into a horizontal component $\mathbf{U} = [u, v]^T$ and a vertical component w. By first integrating over the depth of a layer and then over the area of an arbitrary control volume V_i which is either a prismatic element or a linear element as described above, we obtain the semi-discrete finite volume form:

$$\frac{d\overline{\chi}}{dt} = \frac{1}{A_i}\left(\sum_{k}^{2} Q_k - \sum_{j} Q_j \right) \tag{2}$$

Or

$$\frac{d\overline{\chi}}{dt} = \sum_{k}^{2} q_k - \sum_{j} q_j \tag{3}$$

where $\overline{\chi}$ represents the average volumetric storage of χ per unit planimetric control volume area A_i, Q_k is the net volumetric flux across the upper and lower boundaries (k = 1, 2), and Q_j is the net volumetric flux through the horizontal sides. q_k and q_j are the volumetric fluxes Q_k and Q_j normalized by the area of the control volume respectively. The number of horizontal sides depends on the elements, i.e., j = 3 for prismatic elements and j = 6 for river elements (Figure 4-1).

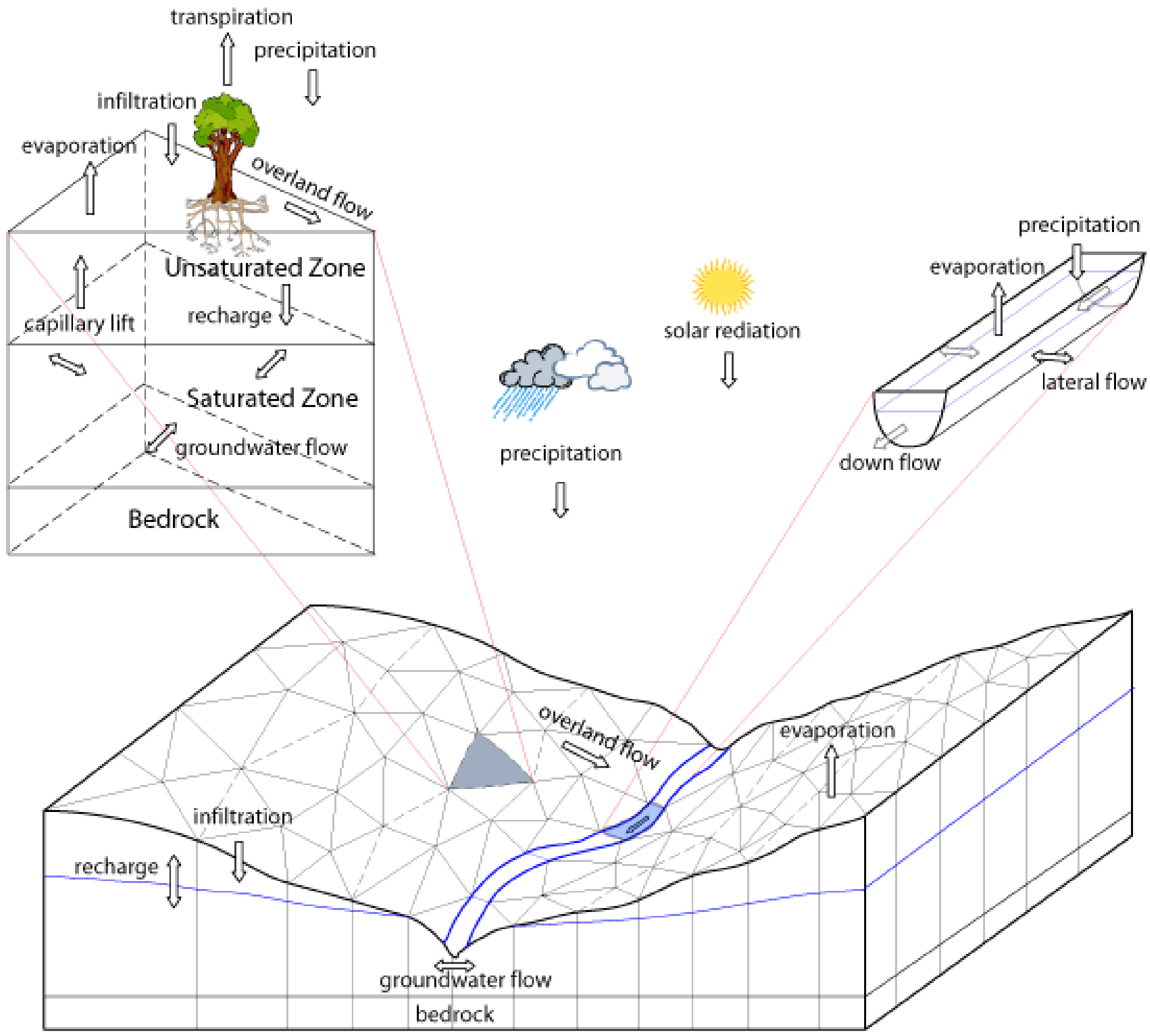

Figure **4-1**: Schematic view of the domain decomposition of a hillslope scale example. Basic prism element is shown to the left with multiple hydrological processes. Channel segment is shown to the right. The major hydrologic processes associated with elements and their connections are also shown [Qu and Duffy, 2007].

The vector form of equation (2) represents all processes $\bar{\boldsymbol{\chi}} = [\chi_1, \chi_1, \ldots, \chi_p]^T$ within the control volume and forms a fully coupled local ODE system through the vertical fluxes and lateral fluxes. The fluxes are evaluated by appropriate constitutive relationships for specific processes and applications. It is noted that the semi-discrete finite volume method used here can guarantee mass conservation [Leveque, 2002] and reduces all equations to a standard form [Qu and Duffy, 2007].

Model Kernel

As discussed above, the domain is decomposed into Delauney triangles for watershed and lines for rivers, forming prismatic volumes in 3D which are further subdivided into layers to account for the physical process equations and material layers (Figure 4-1). In each prism the semi-discrete FVM approach provides a convenient way to couple the mixtures of PDEs and ODEs for multiple hydrological processes. The PDEs are firstly reduced to ODEs by using this approach, and then all ODEs are associated with layers within a prism forming the "local system" (Figure 4-1). The prism and the local system of ODEs together are referred to as the kernel [Qu and Duffy, 2007]. Assembling the local systems over the entire domain leads to a "global" system which is solved with a state-of-the-art ODE solver. According to Qu and Duffy [2007], this approach is a flexible and efficient strategy for multi-process modeling in that (1) the model kernel represents all hydrological processes within the prism and can be easily modified for different applications or processes without altering the ODE solver and the domain decomposition for the data structure of PIHM is independent of the ODE solver; (2) the ODE system is solved in a fully-coupled way with no time lagging or iterative linking of processes.

Numerical Solver

In solving the global ODEs system, all state variables are solved simultaneously and advanced together temporally. The time step is adaptively determined by the fastest times scale of the interaction processes. Typically this ODEs system consists of very slow processes (e.g., groundwater flow) and very fast ones (e.g., overland flow and channel flow), which makes it stiff. It requires a stiff solver. The Newton-Krylov implicit solver is a typical choice for large non-linear stiff ODE systems [Jones et al., 2000; Jones et al, 2001]. CVODE [Cohen and Hindmarsh, 1994] from the SUNDIALS (SUite of Nonlinear and DIfferential/ALgebraic equation Solvers) is used here. For stiff non-linear systems, CVODE uses the Backward Differentiation Formula (BDF) combined with Newton iterations, which in turn requires solution of the linear system by a preconditioned Krylov solver, GMRES. It is noted that CVODE runs automatically with an adaptive time step and order-adjustment during simulation, adjusting the step size to meet the local error test. This algorithm provides stable and accurate solutions for the stiff system in the model.

Model Framework

The major hydrological and sediment transport processes along with governing equations in PIHM are presented below. A brief discussion of the hydrological processes is first given. Details can be found in Qu and Duff [2007]. Then the sediment transport processes are described in detail.

Hydrologic Processes

In this version of PIHM (2.0), we consider the following hydrological processes: two-dimensional (2-D) surface overland flow, 1-D channel flow, and 2-D subsurface flow, canopy interception, evapotranspiration along with their interactions. Snowmelt, macropore infiltration, and macroporous stormflow are not considered in this study.

Surface overland flow

The transient flow of water on the land surface is simulated by the diffusion wave approximation of the 2-D depth-averaged shallow water equations. The kinematic wave approximation is also available in PIHM but not considered in this study. In diffusion wave approximation, the friction slope is approximated by the Manning equation and the inertial force including local acceleration and convective acceleration is neglected [Gottardi and Venutelli, 1993]. It is given by

$$\frac{\partial h_o}{\partial t} = \frac{\partial}{\partial x}\left(h_o k_x \frac{\partial H}{\partial x}\right) + \frac{\partial}{\partial y}\left(h_o k_y \frac{\partial H}{\partial y}\right) + \sum_k q_k \tag{4}$$

with

$$k_x = \frac{h_o^{\frac{2}{3}}}{n_1}\left|\nabla_s H\right|^{-\frac{1}{2}} \text{ and } \quad k_y = \frac{h_o^{\frac{2}{3}}}{n_2}\left|\nabla_s H\right|^{-\frac{1}{2}} \tag{5}$$

where h_o is local flow depth, $H = h_o + z_s$ is the water surface elevation above an horizontal datum with z_s = elevation of overland surface of grid *i*, n_1 and n_2 are Manning roughness coefficients in the x and y direction, k_x and k_y are the conductivities in the *x* and *y* direction, $\nabla_s H$ is the gradient of surface overland flow head along the direction of maximum slope of the triangular plane *i,* and q_k are the layer top and bottom input/output. Applying the semi-discrete FVM approach to Equation (4) yields the semi-discrete ODE:

$$\frac{\partial h_o}{\partial t} = p - e^s - q^+ + \sum_{j=1}^{3} q_{ij}^s \tag{6}$$

where p , e^s and q^+ are through-fall precipitation, evaporation from the overland surface, and infiltration/exfiltration respectively. q_{ij}^s is the normalized lateral flow rate from the grid *i* to its neighbor *j*, calculated by:

$$q_{ij}^{s} = \left(k_s\right)_{ij}\left(\nabla_n H\right)_j \frac{\left(h_o\right)_i + \left(h_o\right)_j}{2} L_{ij}\left(A_i\right)^{-1} \tag{7}$$

where $\left(k_s\right)_{ij}$ is the harmonic mean of the conductivities between the grids *i* and its neighbor *j*, $\left(\nabla_n H\right)_j$ is the gradient between grids *i* and *j* along the normal direction of the edge *j*, L_{ij} is the length of edge *j*.

Channel flow

Flow through a network of rivers and channels is simulated by the diffusion wave approximation to the 1-D shallow water equations. The semi-discrete ODE for 1-D shallow water equations reduces to:

$$\frac{\partial h_c}{\partial t} = p - e^c - q^l + \sum_{j=1}^{2}\left(q_j^s + q_j^g\right) + q_{up}^c - q_{dn}^c \tag{8}$$

where h_c is the flow depth in the channel. e^c and q^l are evaporation from river and flux between river and sub-channel groundwater respectively. q_j^s and q_j^g are the lateral interaction terms for the aquifer and surface flow from each side of the channel. q_{up}^c and q_{dn}^c are the flow from/to upstream and downstream channel segments respectively, which are estimated using Equation (7).

Unsaturated zone

The subsurface layer is partitioned into two parts by groundwater table, unsaturated zone and saturated zone separated. The unsaturated zone is governed by gravitational and surface tension forces, while the saturated zone is governed by the gravitation alone. Generally, flow in a porous medium is much slower than surface flow. Water movement in an unsaturated zone is even slower than in a saturated zone. Applying the semi-discrete FVM approach to Richard's equation [Richard, 1931] leads to the ODE in the unsaturated zone:

$$\frac{\partial h_u}{\partial t} = q^{+} - q^{-} - e^{u} - e^{t} \tag{9}$$

where h_u is the equivalent depth of moisture storage in the unsaturated zone. q^{-} is the flux between saturated and unsaturated zones using Richard's equation, referred to as recharge to/from the water table. e^{u} and e^{t} represent the evaporation from upper soil layer and the transpiration respectively.

Groundwater flow

Applying the semi-discrete FVM approach to Richard's equation also yields the ODE for Darcy-type groundwater flow in the saturated zone:

$$\frac{\partial h_g}{\partial t} = q^{-} + \sum_{j=1}^{3} q_{ij}^{g} \tag{10}$$

where h_g is the equivalent depth of moisture storage in the saturated zone. q_{ij}^{g} is the normalized lateral groundwater flow rate from the grid *i* to its neighbor *j*, which can be calculated by an equation similar to (7):

$$q_{ij}^{s} = \left(k_g\right)_{ij} \left(\nabla_n H_g\right)_j \frac{\left(h_g\right)_i + \left(h_g\right)_j}{2} L_{ij} \left(A_i\right)^{-1} \tag{11}$$

where $\left(k_g\right)_{ij}$ is the harmonic mean of the hydraulic conductivities between the grids *i* and its neighbor *j*, $H_g = h_g + z_g$ is the water surface elevation above an horizontal datum with z_g =

elevation of datum of grid *i*, and $(\nabla_n H_g)_j$ is the gradient between grids *i* and *j* along the normal direction of the edge *j*.

Interception

A fraction of precipitation is intercepted by vegetation and canopy before it impacts the ground. Water intercepted by vegetation is a function of precipitation (p_v), evaporation from canopy (e^v), as well as through-fall and stemflow or effective precipitation to soil surface (p):

$$\frac{dh_v}{dt} = p^v - e^v - p \tag{12}$$

where h_v is the interception storage. p is estimated based on an exponential formulation [Rutter and Morton, 1977].

Infiltration

Infiltration is estimated based on the approach of Freeze [1978]:

$$q^+ = k_q \frac{(h_s + z_s) - (h_u + z)}{d} \tag{13}$$

where k_q is the hydraulic conductivity of the top soil layer and l_s is a specified vertical distance across which the head gradient is calculated. This formulation is based on continuity in hydraulic head across the surface skin thickness ($2l_s$).

Evapotranspiration

Actual evapotranspiration (ET) is the sum of transpiration (e^t), and evaporation from vegetation interception (e^v), overland flow (e^s), river surfaces (e^c), and upper soil layer (e^u). e^v, e^s and e^c are estimated using the Pennman Equation [Bras, 1990] while e^u is estimated using the modified Pennman Equation [Schmidt et al., 2005]. e^t is calculated based on the formulation of Blondin [1991]. Readers interested in detail are referred to Qu and Duffy [2007].

Surface overland flow to river

The surface flow across the bank is approximated by the formulation developed by Robertson [1986].

Unsaturated-saturated flux

The flux between the unsaturated and saturated zone is based on Richard's Equation by assuming a vertical exchange across a moving boundary (water table interface). The approximation equation developed by Duffy [1996] is used.

River-aquifer flux

The interaction items between aquifer and river in the vertical and lateral directions are calculated using the similar equation as (10).

Sediment Transport Processes

Sediment yield from a watershed is a result of erosion, transport, and deposition by water flow. Within a watershed these processes can be generally partitioned into those acting on hillslopes and those acting in channels. On hillslopes, the rainfall events are of major importance in determining sediment yield. Actually, it is the rainfall and runoff during rainfall events that causes the sediment transport. In channels, rainfall is of minor, even negligible, importance to sediment transport. Channel flow continuously transports sediment. For both hillslopes and channels, available sediment or erodible material is one of the important factors in determining sediment yield.

The principle sediment transport processes on hill slopes include (1) detachment by raindrop impact, (2) detachment by overland flow, and (3) overland sediment routing, which are also commonly incorporated in other physically-based sediment transport models [e.g., KINEROS2, SHESED, EUROSEM].

Overland sediment routing

Mass balance equation(s) can be used to represent the sediment dynamics in the water flow. There are two different approaches to sediment routing, one is to treat the bed material as a total load as, for example, in many physically-based models at the watershed scale[e.g., Kennedy, 1963; Simon et al., 1965; Bennett, 1972; Foster and Meyer, 1972; Kirkby, 1980; Knisel, 1980; Woolhiser et al., 1990; Flanagan and Nearing, 1995; Lane et al., 1995; Wicks and Bathurst, 1996; Morgan et al., 1998; Heppner et al., 2006, 2007]. The other approach is to differentiate the bed material into bed load and suspended load as is common in river simulations [Bennet and Nordin, 1977; van Rijn, 1984; van Rijn, 1986; van Rijn, 1987; Armanini and Di

Silvio, 1988; Celik et al., 1988; Rahuel et al., 1989; Holly Jr. and Rahuel, 1990; Spasojevic and Holly Jr., 1990; Kassem and Chaudhry, 1998; Wu et al., 2000; Fagherazzi and Sun, 2003; Wu, 2004]. The suspended-bed load approach can provide more information than the total load method but causes the additional cost of solving one more equation. It also introduces more parameters and may introduce extra errors since the sediment transport mechanism is so complicated that it is hard to tell what types of sediment should move in suspended form or in bed form. Moreover, it gets more difficult to solve the equation system due to the different time scales between bed deformation, bed load transport, and suspended load transport.

Based on this discussion the total load approach is adopted in this watershed-scale physically-based model. By neglecting diffusion, the mass balance equations for sediment transport can be written as

$$\frac{\partial(h_c)}{\partial t} + \frac{\partial(h_c u)}{\partial x} + \frac{\partial(h_c v)}{\partial y} = D_r + D_h \tag{14}$$

$$\frac{\partial z_s}{\partial t} = -\frac{(D_r + D_h)}{1 - p} \tag{15}$$

where h_c is the volume of sediment per unit area and p is the porosity of bed material. D_r and D_h are the detachment rates by raindrop splash and surface overland flow respectively. Equation (14) states that the temporal variation of sediment volume suspended in the water column is equal to the sum of the divergence of the sediment flux and the sediment entrainment/deposition while Equation (15) links the local variation in bed level to the sediment removed or accumulated at the bottom.

Applying the semi-discrete FVM approach to Equations (14) and (15) yields the ODE for sediment routing by surface overland flow:

$$\frac{dh_c}{dt} = \sum_{j=1}^{3} q_{ij}^{st} + D_r + D_h \tag{16}$$

$$\frac{dz_s}{dt} = -\frac{(D_r + D_h)}{1-p} \tag{17}$$

where q_{ij}^{st} is the normalized volumetric transport rate of sediment suspended in surface overland flow from the grid i to its neighbor j, calculated by:

$$q_{ij}^{st} = h_c(\mathbf{U} \cdot \mathbf{n}_{ij})L_{ij} \tag{18}$$

with $\mathbf{n}_{ij}$ being the unit outward normal vector to the edge j.

Detachment by raindrop splash

Raindrops contribute to the sediment transport by breaking the cohesive bonds between soil particles and making them available for transport by overland flow [Wicks and Bathurst, 1996]. Rainsplash detachment rate (D_r) may be a function of rainfall intensity [Meyer and Wischmeier, 1969; Woolhiser et al., 1990], momentum [Wicks and Bathurst, 1996], and kinetic energy [Morgan et al., 1998]. According to Kirkby (1980), the rainsplash detachment is commonly correlated to rainfall intensity although it may be related to storm energy and momentum. In this study, modeling this process is based on the relationships between splash erosion rate and the rainfall intensity.

$$D_r = e_r k(h_o) p^2 \tag{19}$$

in which e_r is a constant related to soil and surface properties, $k(h_o)$ is a reduction factor representing the reduction in splash erosion caused by increasing depth of water. The reduction function takes similar although a little bit different forms. One general form is:

$$k(h_o) = \exp(-e_d h_o) \tag{20}$$

with e_d being the damping effectiveness of surface water.

It is evident that the equations are mostly based on empirical work. A few assumptions are made about these equations (e.g., drop size distribution) [Wicks and Bathurst, 1996] and some parameters are hard to explain physically and be measured such as soil erodibility. Therefore calibration needs to be done to obtain the appropriate values of these parameters.

Detachment by surface overland flow

Overland flows typically consist of a combination of the shallow flows of large width (sheet flow) and the concentrated flows in small eroding channels (rills). The soil erosion process is described as the sequence of (1) detachment of soil particles by raindrop, (2) transport of the detached soil to rills by sheet flow, and (3) transport of soil particles by rill flow. The soil erosion model such as RUSLE (Foster et al., 1981), ANSWERS (Beasley et al., 1980), and WEPP (Nearing et al., 1989) differentiate between the rill and interrill detachment. Due to the element-based calculation of flow in PIHM, however, it is impossible to separate the subgrid processes of rill and sheet flows.

The detachment by flow (D_h) essentially consists of two continuous counteracting processes of erosion and deposition. One common approach to their cumulation is to relate the flow detachment to the difference between transport capacity concentration and current sediment concentration [e.g., Woolhiser et al., 1990; Morgan et al., 1998; Heppner et al., 2006, 2007]. It is based on the assumption that the ability of water flow to erode the river bed is independent of the sediment it carries and is only a function of energy expended by the flow:

$$D_h = e_h\left(c_m - c_s\right)h_0 \tag{21}$$

where e_h is a transfer rate coefficient, c_s is the current local sediment concentration, and c_m is the concentration at equilibrium transport capacity. Based on the analysis of Woolhiser et al. [1990] and Heppner et al. [2006, 2007], the following equation is used to calculate e_h:

$$e_h = \begin{cases} \zeta\omega_s & if\ c \geq c_m \\ \xi hu & if\ c < c_m \end{cases} \tag{22}$$

where ω_s is the settling velocity of sediment particle, ζ and ξ are the coefficients for deposition [-] and entrainment [L^{-1}] respectively.

The sediment discharge at the watershed outlet gives the sediment yield from the entire watershed. It is determined by the sediment availability and the transport capacity of the river flow. The sediment available at a river reach comes from the sediment input from overland flow, sediment inflow from upstream, detachment of local river bed by channel flow with bank erosion ignored in this version of model. Usually sediment particles are not uniform in natural rivers. Therefore the sediment size distribution is considered in calculation of sediment transport capacity and sediment routing. It makes the model capable of simulating the vertical variation in particle size distribution of the bed material, the bed armouring process. The principle sediment transport processes in channel are nearly the same as those for hillslope except that raindrop splash erosion is neglected in channel flow and the lateral inflow of sediment from overland surface flow is important.

Channel sediment routing

Sediment routing through a network of rivers and channels is simulated using the same approach on hillslope. The semi-discrete ODE for 1-D channel sediment routing reduces to:

$$\frac{dh_c}{dt} = q_{in}^{ct} - q_{dn}^{ct} + D_h \tag{23}$$

$$\frac{dz_s}{dt} = -\frac{D_h}{1-p} \tag{24}$$

where q_{up}^{ct} and q_{dn}^{ct} are the normalized volumetric transport rate of sediment suspended in channel flow from/to upstream and downstream channel segments respectively, which are estimated using Equation (18).

Detachment by channel flow

Detachment by channel flow is calculated based on the same equation (21) for surface overland flow.

Sediment transport capacity by surface overland flow and channel flow

There are numerous equations for sediment transport capacity, and most have been developed and tested for relatively deep and mildly sloping flow conditions, such as streams and flumes [Woolhiser et al., 1990]. Overland flow transport capacity is influenced by many factors including runoff rate, flow velocity, slope steepness, transportability of detached soil particles, and even the raindrop impact [Tayfur, 2002]. Typical formulations can be divided into shear stress-based, stream power-based, and unit stream power-based.

According to the experimental work by Alonso et al. [1981], Julien and Simons [1985], and Govers [1990], the transport capacity equation of Engelund-Hansen [1967] is appropriate for overland flow as for example in KINEROS2 [Woolhiser et al., 1990], SHESED [Wicks and Bathurst, 1996], and InHM [Heppner et al., 2006, 2007]:

$$c_m = 0.05 \frac{\sqrt{u^2 + v^2}\, u_*^3}{g^2 dh(\gamma_s - 1)^2} \tag{25}$$

where $u_* = \sqrt{ghS_f}$ is the shear velocity with S_f the energy slope, d is the sediment particle diameter, and $\gamma_s = \rho_s / \rho_w$ is the sediment specific gravity.

For a channel, there are a large number of sediment transport equations. All of them contain some empirical components and no single equation yielded good results for all river and sediment conditions. However, according to White et al. [1975], Alonso [1980], and Bathurst et al. [1987], the Engelund-Hansen [1967] total load equation (25) is one of those that appear more generally applicable. Therefore, Equation (25) is used to calculate transport capacity for both surface overland flow and channel flow.

Bed Armoring Process

This model considers a sediment size distribution, thereby enabling simulation of the bed armoring process. This process is important in river and channel sediment transport modeling, especially for gravel-bed rivers. In this model the river bed is divided into layers and the bed armoring is done by transporting the sediment by size fraction. This leads to vertical variations in particle size distribution in river bed material [e.g., Bennett and Nordin, 1977].

In this model, the available bed depth is divided into two or three layers depending on erosion or deposition: active layer and parent layer, or active layer, middle layer, and parent layer. The active layer is set to $2d_{50}$ of the parent layer particle distribution, where $2d_{50}$ is the particle diameter for which 50% of the bed material is finer. The algorithm is described as follows:

(1) Initial condition: the bed is divided into two layers, i.e., active layer and parent layer.

(2) If erosion occurs at time step t_i, the flow will detach the sediment from the active layer according to the residual transport capacity (RTC) for different size classes, where the RTC denotes the difference between the existing sediment suspended in the water column and the

transport capacity. At the end of t_i, if any size of sediment still exists, the active layer will exist even if the RTC for a certain particular size is larger than the available in the active layer. Otherwise, jump to step (4).

(3) If the active layer still exists, the corresponding lost volume of sediment fills the active layer from the lower layer (middle layer or parent layer depending on two or three layers) with the same composition as that layer.

If there is not enough sediment in the lower layer: for the case of two layers all available sediment fills the active layer and the parent layer vanishes; for the case of three layers, the middle layer vanishes, the sediment of parent layer also comes into the active layer, and if there is still not enough sediment, the parent layer vanishes. When there is not enough sediment from below to replenish the active layer, the thickness of the active layer will be less than $2d_{50}$.

(4) If the active layer is eroded away, a thickness of lower layer equal to $2d_{50}$ will become the active layer if there is enough in the lower layer. If there is not enough in all the lower layer(s), the thickness of the active layer will be less than $2d_{50}$. Then steps 2 to 4 are repeated.

(5) In the case of deposition occurring at time step Δt_i, if the thickness of active layer is less than $2d_{50}$, the composition of the active layer will change and there is no further action; otherwise if the deposition depth is less than $2d_{50}$, then a part of active layer will turn into the middle layer, and the rest of the active layer and the deposited sediment will be mixed as the new active layer ($2d_{50}$ thick) ; otherwise if the deposition depth is greater than $2d_{50}$, then all the active layer and part of the deposited layer will turn into the middle layer, and the rest of the deposited sediment becomes the new active layer ($2d_{50}$ thick).

Results and Discussion

Next we apply the model to a hypothetical rainfall event in the Shale Hills watershed. The objective of this example is to demonstrate the capability of the model in a multi-process simulation at watershed scale. The Shale Hills watershed is 19.8 acres in area in the Valley and Ridge physiographic province of central Pennsylvania (Figure 4-2). The elevation ranges from 258.2 m to 310.2 m (Figure 4-2). The watershed is decomposed into 566 triangles and the river is discretized into 21 segments (Figure 4-3). A 60-minute hypothetical rainfall event is designed as shown in Figure 4-4.

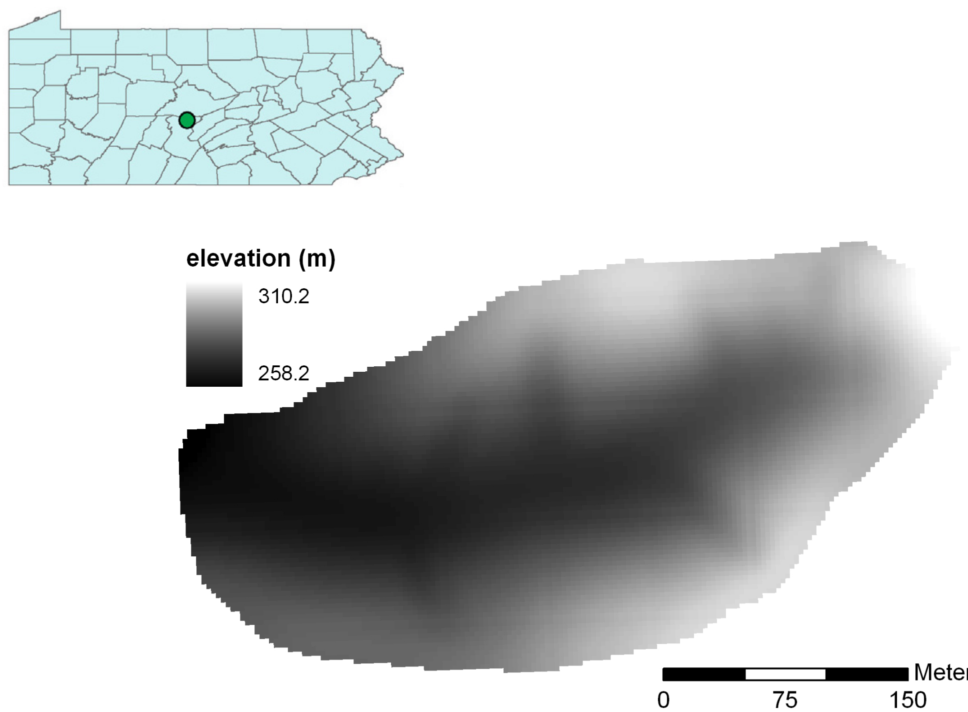

Figure **4-2**: The DEM (digital elevation map) of the Shale Hill watershed.

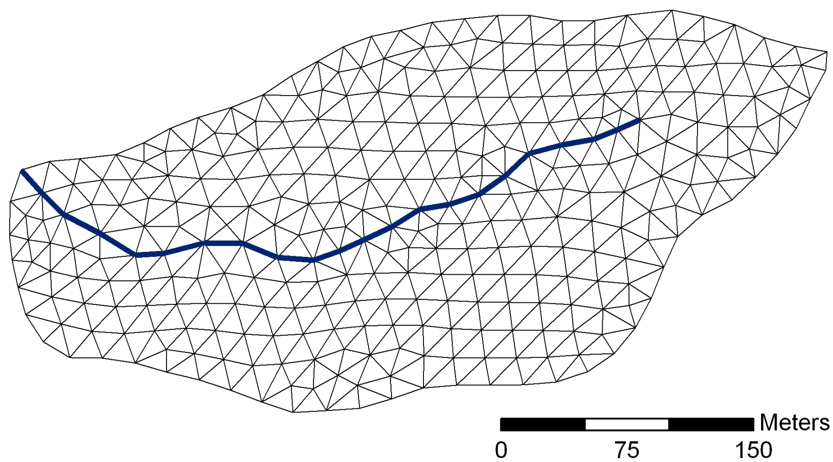

Figure **4-3**: Domain decomposition of the Shale Hill watershed.

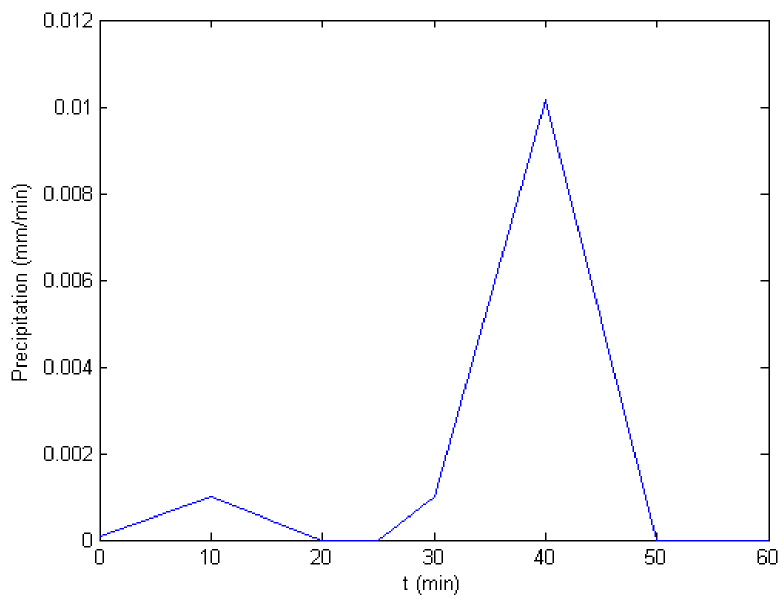

Figure **4-4**: A hypothetical rainfall event for the Shale Hill watershed experiment.

The initial conditions for ground water table, unsaturated soil moisture equivalent depth, surface overland flow depth, stream flow depth, and sediment load are 0.30 m, 0.08 m, 0.000001 m 0.000001 m, and 0 respectively. No-flow boundary conditions are forced on the surface flow, subsurface flow, and sediment flow around the watershed perimeter. The zero-depth-gradient boundary condition is set at the stream outlet. The bed material is assumed composed of 60% of coarse silt (0.0004 m), 30% of coarse sand (0.002 m), and 10% of shale chips (0.02 m).

Figure 4-5 shows the hydrograph and sedigraph at the outlet. Comparison of the Figure 4-4 (a) and (b) illustrates how the water flow controls the sediment discharge. The water discharge and sediment discharge increase from early times to the time of peak flow, converging on the channel, and then decrease thereafter. The temporal variations in sediment discharge follow those in water discharge. Another interesting phenomenon is that although the first period of rainfall is very small, it doe increase the antecedent moisture preceding the second intense rainfall event. It makes more rainfall in the second event quickly turn into runoff and produces more severe erosion as will be discussed next.

Figure 4-6 shows areas of cumulative erosion and deposition at t=60 min. It is evident that erosion occurs in most area of the watershed due to the intense short-duration rainfall. Apparently the spatial distribution of cumulative erosion and deposition follows a certain pattern. By comparing Figure 4-6 and the bed slope in Figure 4-7, we can see that the spatial distribution of cumulative erosion and deposition follows the one of the bed slope. Erosion occurs on where the slope gradient is high while sediment deposits in the areas near the stream where the slope gradient is small and sediment concentration in the water flow is high.

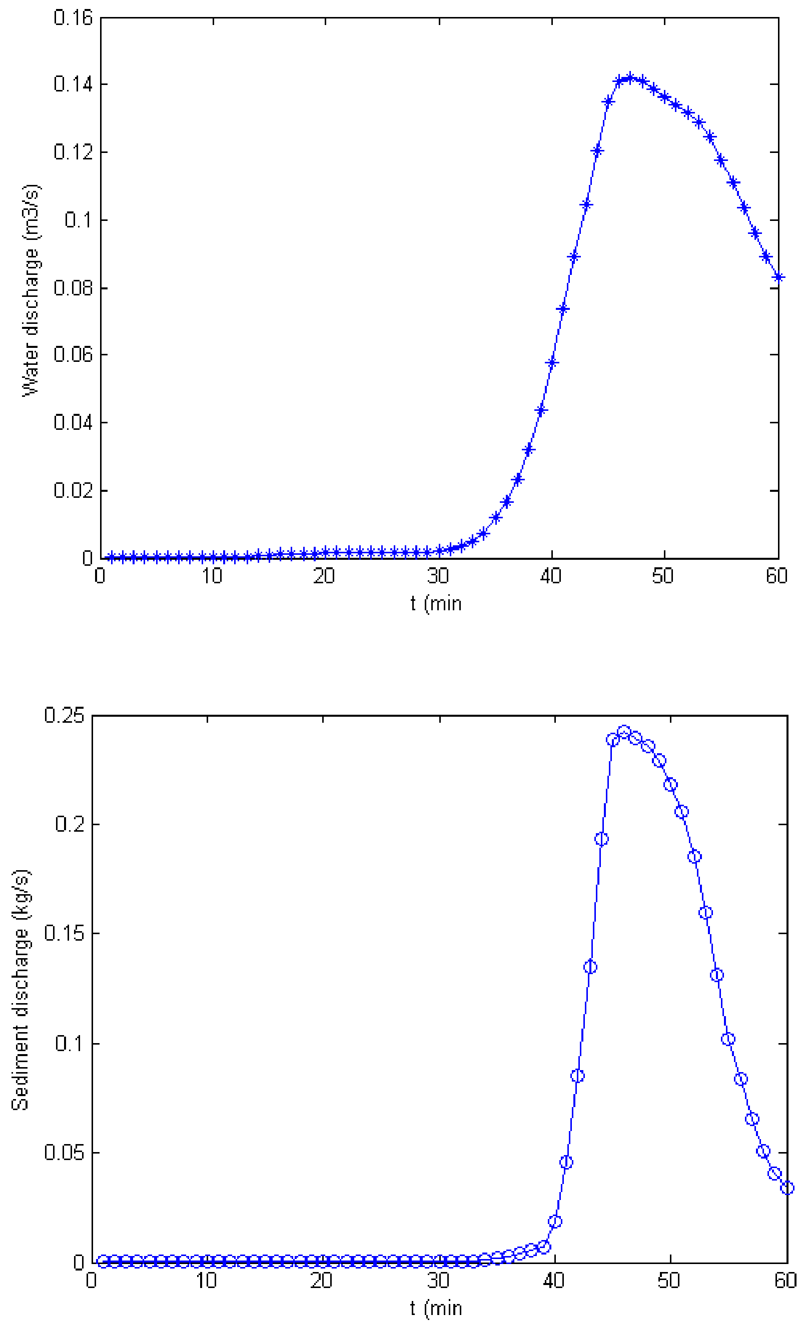

Figure **4-5**: The hydrograph and sedigraph at the outlet of the Shale Hills watershed.

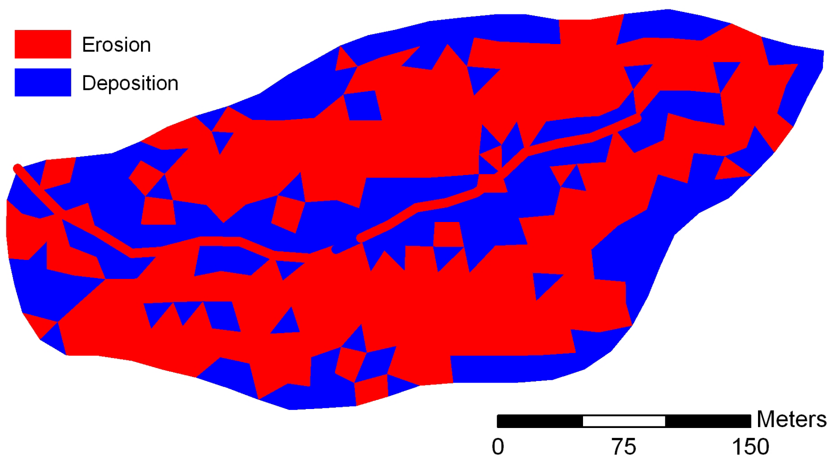

Figure **4-6**: The spatially variable sediment transport process over the watershed.

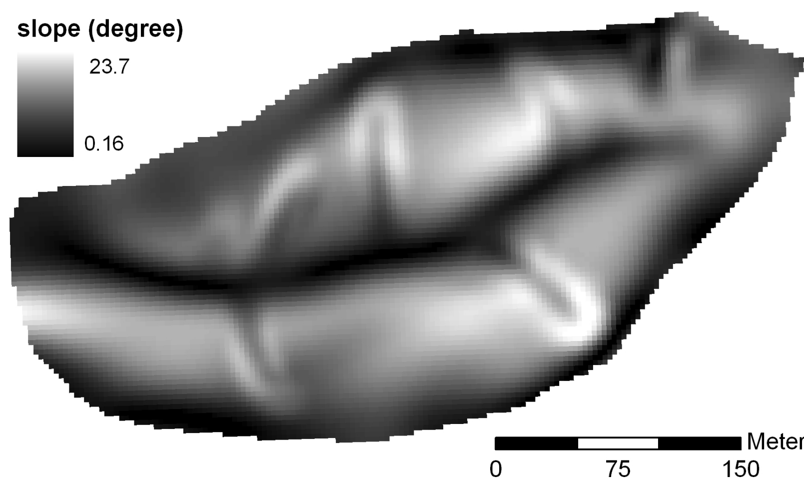

Figure **4-7**: The slope gradient (degree) of the Shale Hills watershed.

Conclusions

In this study, PIHM-Sed, a spatially-distributed, physically-distributed sediment transport component at the watershed scale, is developed and fully coupled with the hydrological processes in the PIHM modeling system. It makes a unique contribution to sediment transport modeling in that for the first time PIHM-Sed "fully-couples" hydrology and sediment transport physically and numerically. It integrates sediment transport for hillslope and channel processes, including the effects of surface/subsurface hydrological processes on hydrologic performance and sediment yield and the spatial distribution of erosion/deposition. PIHM, a pioneer work of Qu and Duffy [2007], integrates the major hydrological processes at the watershed scale using the semi-discrete finite volume method, providing a sound hydrologic modeling framework for sediment transport modeling.

A preliminary testing of PIHM-Sed has been done using a hypothetical storm event at the Shale Hill watershed. This example shows how this model captures the dynamics of multiple processes including hydrology and sediment transport at the watershed scale.

This is only the first step in the development of PIHM-Sed. Future efforts will rigorously test PIHM-Sed in simulating multiple processes against the field measurement at the different scales of watersheds such as small-, meso- and large-scale. It is doubtless that there are very few data sets appropriate to such tests. It was very difficult to find one when this study presented here was done. With the continuing evolution of the PIHM modeling system, PIHM-Sed, as one of its component, will be integrated with the new-version of hydrology model so that its capability in sediment transport modeling will be enhanced.

References

[138] Abbott, M.B., J.A. Bathurst, P.E. and Cunge. 1986. An Introduction to the European Hydrological System-Systeme Hydrologicque Europeen "SHE" 2: Structure of a physically based distributed modeling system, Journal of Hydrology, 87, 61-77.

[139] Alonso, C.V., Neibling, W.H. and Foster, G.R. 1981. Estimating sediment transport capacity in watershed modeling. Trans. ASAE, 24(5): 1211-1220, 1226.

[140] Armanini, A., and Di Silvio, G. 1988. A one-dimensional model for the transport of a sediment mixture in non-equilibrium conditions. J. Hydraul. Res., 26 (3): 275–292.

[141] Beasley, D.B., Huggins, L.F., Monke E.J. 1980. ANSWERS: a model for watershed planning. Trans Am Soc Agric Eng, 23: 938–44.

[142] Bennett, J.P. 1974. Concepts of mathematical modeling of sediment yield. Water Resources Research, 10(3): 485-492.

[143] Bennett, J.P. and Nordin, C.F. 1977. Simulation of sediment transport and armouring. IAHS Hydrol. Sci. Bull., 22(4): 555-569.

[144] Blondin ,C. 1991. Parameterization of land-surface processes in numerical weather prediction, in Land Surface Evaporation; Measurements and Paramrleizuliun, edited by T.J. Schmugge and J.C. Andre, pp. 31-54, Springer-Vedag, New York.

[145] Bras, R.L., 1990. Hydrology, An introduction to hydrologic science. Addison-Wesley publishing company.

[146] Celik, I., and Rodi, W. 1988. Modeling suspended sediment transport in non-equilibrium situations. J. Hydr. Engrg., ASCE, 114(10), 1157–1191.

[147] Chang, H. H. 1982. Mathematical model for erodible channels. J. Hydraul. Div., Am. Soc. Civ. Eng., 108(5): 678–689.

[148] Cohen, S.D., and A.C. Hindmarsh. 1994. CVODE User Guide, Numerical Mathematics Group, LLNL. UCRL-MA-118618.

[149] Duffy, C.J. 1996. A two-state integral-balance model for soil moisture and groundwater dynamics in complex terrain. Water Resources Research, 32 (8): 2421–2434.

[150] Engelund, F. and Hansen, E. 1967. A monograph on sediment transport in alluvial streams. TekniskForlag, Copenhagen.

[151] Fagherazzi, S. and Sun, T. 2003. Numerical simulations of transportation cyclic steps. Computers and Geosciences. 29: 1143-1154.

[152] Flanagan, D.C. and M.A. Nearing, eds. 1995. USDA-Water Erosion Prediction Project: Technical Documentation. NSERL Report No. 10. West Lafayette, Ind.: USDA-ARS-NSERL.

[153] Foster, G.R. and Meyer, L.D. 1972. A closed-form soil erosion equation for upland areas. In: Sedimentation (ed. H.W. Shen), pp. 12.1–12.17. Colorado State University, Fort Collins, CO.

[154] Foster, G. R., Lane, L. J., Nowlin, J. D., Laflen, J. M. and Young, R. A. 1981. Estimating erosion and sediment yield on field-sized areas, Transactions of the American Society of Agricultural Engineers, 24, 1253–1263.

[155] Gerits, J..J.P, de Lima, J.L.M.P., van den Broek, T.M.W. 1990. Overland flow and erosion. In: Anderson, Burt, editors. Process studies in hillslope hydrology. Chichester, West Sussex, England: John Wiley and Sons Ltd.

[156] Gottardi, G. and M. Venutelli. 1993. A control-volume finite-element model for two-dimensional overland flow, Advances in Water Resources, 16: 277-284.

[157] Govers, G. 1990. Empirical relationships on the transporting capacity of overland flow, International Association of Hydrological Sciences, Publication 189, 45–63.

[158] Hindmarsh and Serban. 2005. User Documentation for cvode v2.3.0. Center for Applied Scientific Computing Lawrence Livermore National Laboratory, UCRL-SM-208108.

[159] Han, Q. W. 1980. A study on the nonequilibrium transportation of suspended load. Proc., 1st Int. Symp. on River Sedimentation, Beijing.

[160] Heppner, C.S., Ran, Q., VanderKwaak, J.E., Loague, K. 2006. Adding sediment transport to the integrated hydrology model (InHM): Development and testing. Advances in Water Resources, 26: 930-943.

[161] Heppner, C.S., VanderKwaak, J.E., Loague, K. 2007. Long-term InHM simulations of hydrologic response and sediment transport for the R-5 catchment. Earth Surf. Process. Landforms 32: 1273-1292.

[162] Holly, Jr., F. M., and Rahuel, J. L. 1990. New numerical/physical framework for mobile-bed modeling, Part I: Numerical and physical principles. J. Hydraul. Res., 28(4): 401–416.

[163] Horton, R. E. 1945. Erosional development of streams and their drainage basins: hydrophysical approach to quantitative morphology. Bull Geol Soc Am: 275–370.

[164] Jones, J.E. and C.S. Woodward. 2000. Preconditioning Newton–Krylov methods for variable saturated flow. In: Bentley LR, Sykes JF, Brebbia CA, Gray WG, Pinder GF, editors.Computational methods in water resources, Vol. 1. Rotterdam: Balkema: 101-106.

[165] Jones, J.E. and C.S. Woodward. 2001. Newton–Krylov-multigrid solvers for large-scale, highly heterogeneous, variably saturated flow problems. Adv Water Resour, 24: 763-774.

[166] Julien, P.Y. and Simons, D.B., 1985. Sediment transport capacity of overland flow. Trans. ASAE, 28(3): 755-162.

[167] Kassem, A., and Chaudhry, M. H. 1998. Comparison of coupled and semicoupled numerical models for alluvial channels. J. Hydraul. Eng., 124(8), 794–802.

[168] Kennedy, J.F., The mechanics of dunes and antidunes in erodible bed channels, J. Fluid Mech., 16, 521-524, 1963.

[169] Kirkby, M. J. 1978. Implications for sediment transport. In: Kirkby, editor. Hillslope hydrology. Chichester, West Sussex, England: John Wiley and Sons Ltd.

[170] Kirkby, M. J. 1980. Modelling water erosion processes, in Kirkby, M. J. and Morgan, R. P. C. (Eds), Soil Erosion, Wiley, Chichester,183–216.

[171] Knisel, W. G. 1980. CREAMS: a field scale model for chemicals, runoff and erosion from agricultural management systems. US Department of Agriculture, Conservation Research Report No. 26.

[172] Lane, L.J., Shirley, E.D., Singh, V.P. 1988. Modeling erosion on hillslopes. In: Anderson, editor. Modellinggeomorphological systems. Chichester, West Sussex, England: John Wiley and Sons Ltd.

[173] Leveque, R.J. 2002 Finite Volume methods for hyperbolic problems, Cambridge University Press.

[174] Merritt, W.S., Letcher, R.A., Jakeman, A.J. 2003. A review of erosion and sediment transport models. Environ Model Software, 18: 761–99.

[175] Morgan, R.P.C., Quinton, J.N., Smith, R.E., Govers, G., Poesen, J.W.A., Auerswald, K., Chisci, G., Torri, D., Styczen, M.E. 1998.The European soil erosion model (EUROSEM): a process-based approach for predicting sediment transport from fields and small catchments. Earth Surface Processes and Landforms 23, 527–544.

[176] Nearing, M. A., Foster, G. R., Lane, L. J. and Finckner, S. C. 1989. A process-based soil erosion model for USDA-Water Erosion Prediction Project technology, Transactions of the American Society of Agricultural Engineers, 32, 1587–1593.

[177] Panday, S., Huyakorn, P.S. 2004. A fully coupled physically-based spatially-distributed model for evaluating surface/subsurface flow. Advances in Water Resources 27, 361-382.

[178] Park, S.W., Mitchell, J.K. and Scarborough, J.N. 1982. Soil erosion simulation on small watersheds: a modified ANSWERS model. Trans. ASAE, 25: 1581-1588.

[179] Qu, Y., and C. J. Duffy. 2007. A semidiscrete finite volume formulation for multiprocess watershed simulation, Water Resources Research, 43, W08419, doi:10.1029/2006WR005752.

[180] Richards, L.A. 1931. Capillary conduction of liquids in porous mediums. Physics 1: 318–333.

[181] Roberson JA, Crowe CT.1985. Engineering fluid mechanics. third ed. Boston: Houghton Mifflin Company.

[182] Ross, B.B., Shanholtz, V.O. and Contractor, D.N., 1980. A spatially responsive hydrologic model to predict erosion and sediment transport. Water Resour. Bull., 16(3): 538-545.

[183] Schmidt, M., M. Kerschgens, H. Hübener, and M. Sogalla. 2005. Simulating evapotranspiration in a semi-arid environment, Theoretical and Applied Climatology, 80: 153-167.

[184] Simons, D.B., E.V. Richardson, and C.F. Nordin, 1965. Bedload equation for ripples and dunes, U.S. Geol. Surv. Prof. Pap. 462-H, 9 pp.

[185] Simons, D.B., Li, R-M., Ward, T.J. and Shiao, L.Y., 1982. Modeling of water and sediment yields from forested drainage basins. US For. Serv. Pac. Northwest For. Range Exp. Stn. Rep. PNW-141: 24-38.

[186] Spasojevic, M. and Holly Jr, M.. 1990. 2-D evolution in natural watercourses-new simulation approach. Journal of Waterway, Port, Coastal, and Ocean Engineering, 116(4): 425-433.

[187] Storm, B., Jorgensen, G.H. and Styczen, M. 1987. Simulation of water flow and soil erosion processes with a distributed physically-based modelling system. IAHS Publ. 167, pp. 595-608.

[188] Tayfur, G. 2002. Applicability of Sediment Transport Capacity Models for Nonsteady State Erosion from Steep Slopes. J. Hydrol. Eng., 7(3): 252-259.

[189] Thomas, W. A. 1982. Chapter 18: Mathematical modeling of sediment movement. In R. D. Hey et al., eds., Gravel-bed rivers, Wiley, New York.

[190] VanderKwaak, J., 1999. Numerical simulation of flow and chemical transport in integrated surface-subsurface hydrologic systems. Ph.D Thesis in Earth Sciences, University of Waterloo, Waterloo, Ontario, Canada, 217pp.

[191] van Rijn, L. C. 1984. Sediment transport, Part III: Bed forms and alluvial roughness. J. Hydr. Engrg., ASCE, 110(12), 1733–1754.

[192] van Rijn, L. C. 1986. Mathematical modeling of suspended sediment in nonuniform flow. J. Hydr. Engrg., ASCE, 112(6), 433–455.

[193] van Rijn, L. C. 1987. ‘‘Mathematical modeling of morphological processes in the case of suspended sediment transport.’’ Delft Hydr. Communication No. 382.

[194] White, W.R., Milli, H. and Crabbe, A.D. 1975. Sediment transport theories: a review. Proc. Inst. Civ. Eng., Part 2, 59: 265-292.

[195] Wicks, J.M. and Bathurst, J.C. 1996. SHESED: a physically based, distributed erosion and sediment yield component for the SHE hydrological modeling system. Journal of Hydrology, 175: 213-238.

[196] Wischmeier, W.H., Smith, D.D., 1978. Predicting Soil Erosion Losses: A Guide to Conservation Planning. USDA Agricultural Handbook No. 537, 58 pp.

[197] Woolhiser, D. A., Smith, R. E. and Goodrich, D. C. 1990. KINEROS: A kinematic runoff and erosion model: documentation and user manual, USDA Agricultural Research Service ARS-77.

[198] Wu, W. 2004. Depth-Averaged Two-Dimensional Numerical Modeling of Unsteady Flow and Nonuniform Sediment Transport in Open Channels. J. Hydraul. Eng., 130(10): 1013-1024.

[199] Wu, W., Rodi, W., and Wenka, T. 2000. 3-D numerical modeling of water flow and sediment transport in open channels. J. Hydraul. Eng., 126 (1): 4–15.

[200] Wu, W., Vieira, D. A., Wang, S.S.Y. 2004. One-Dimensional Numerical Model for Nonuniform Sediment Transport under Unsteady Flows in Channel Networks. J. Hydraul. Eng., 130 (9): 914–923.

Chapter 5

SUMMARY AND FUTURE WORK

Summary

Accurate prediction of the hydrodynamics, sediment and pollutant transport over a wide range of spatial scales and the extreme hydrological events (e.g., inland flood, storm surge) has been a challenge and has been receiving more attention given the potential occurrence of extreme hydrological events caused by climate change and their catastrophic nature which has caused huge loss of life and wealth. To solve this challenge, the overall goal of this study is to develop a modeling system to predict the hydrodynamics, sediment and pollutant transport in rivers, floodplains, coastal areas and their watersheds. The main conclusions obtained from this study are summarized below.

In Chapters 2 and 3, a two-dimensional (2-D) finite volume model (PIHM-Hydro) was developed to fully couple the hydrodynamics, sediment and pollutant transport at the scale of river, floodplain, and coastal area. This is the first 2-D high-order model to fully couple shallow water flow and sediment transport in the successful simulation of a real flow field. The model is based on standard upwind finite volume methods using approximate Riemann solvers on unstructured triangular grids. A multidimensional linear reconstruction technique and multidimensional slope limiter were implemented to achieve second-order spatial accuracy. Model efficiency and stability are treated using an explicit-implicit method for temporal discretization with operator splitting. PIHM-Hydro is capable of handling complicated geometry, producing accurate and stable solutions over a wide range of spatial scales and hydrological events, and simulating accurately the interactions of hydrodynamics, sediment and pollutant transport. These advantages of PIHM-Hydro have been illustrated by its successful application on the test cases where multiscale physical processes are dominant over a wide range of spatial scales.

In Chapter 4, I developed a spatially-distributed physically-based sediment transport modeling component at the watershed scale (PIHM-Sed) which is fully coupled with the hydrological processes within the Penn State Integrated Hydrologic Model system (PIHM). This is the first spatially-distributed physically-based model to “fully-couple” hydrology and sediment transport in terms of physical and numerical coupling. It integrates the hillslope and channel processes, and is capable of predicting major surface/subsurface hydrological processes, sediment yield as well as spatial distribution of erosion/deposition. In the model system, all hydrological and sediment transport processes are defined on discretized unit elements as a fully-coupled system of ordinary differential equations (ODEs) using a semi-discrete finite volume method (FVM) on unstructured grids. Application of PIHM-Sed to a hypothetical storm event at the Shale Hill watershed illustrates its capability in multi-process simulation at watershed scale.

In addition to the three papers presented in this dissertation, two C codes named PIHM-Hydro and PIHM-Sed have been developed to implement these models. The PIHM-Hydro is the implementation for the first two papers while PIHM-Sed is corresponding to the third papers.

Future Work

In the light of the main findings in this dissertation, some suggestions are given as follows for improvement of the existing works:

(1) A comprehensive comparisons need to be done in future. First, PIHM-Hydro needs be compared with other numerical methods such as finite element methods and finite difference methods such as MacCormack method and composite method. Second, the performance of the

numerical methods needs to be compared on the unstructured grids and structured grids. Third, PIHM-Hydro needs to be compared the approximation methods or hydrologic routing methods including diffusion, kinematic approximation, Muskingum etc.

(2) The source code of PIHM-Hydro needs to be further examined to test its stability and robustness. A more user-friendly version of PIHM-Hydro should be developed and further embedded in PIHMgis.

(3) PIHM-Hydro should be applied to more gauged rivers and estuaries to test its performance in prediction of sediment and pollutant transport in natural flow fields.

(4) The transport capacity equations for channel flow should be further explored in PIHM-Sed works.

(5) PIHM-Sed should be applied to some gauged watersheds to test its performance.

VITA

SHUANGCAI LI

EDUCATION

PhD, Civil Engineering, December 2008, The Pennsylvania State University, University Park, PA

MS, Physical Geography, July 2003, Beijing Normal University, Beijing, China

BS, Geography, July 2000, Beijing Normal University, Beijing, China

Experience

2005 – 2008, Research Assistant, Department of Civil and Environmental Engineering, The Pennsylvania State University, University Park, PA

2004 – 2005, Research Assistant, School of Natural Resources, University of Missouri, Columbia, MO

2003 – 2004, Research Assistant, Institute of Remote Sensing and GIS, Beijing University, Beijing, China

2000 – 2003, Research Assistant, Department of Resources and Environmental Science, Beijing Normal University, Beijing, China

Selected Papers

Shuangcai Li and Christopher J. Duffy. A finite volume model for multi-scale shallow water flow and sediment transport (PIHM-Hydro) (In preparation).

Shuangcai Li and Christopher J. Duffy. Fully-coupled modeling of shallow water flow and pollutant transport on unstructured grids (In preparation).

Shuangcai Li and Christopher J. Duffy. Integrated modeling of hydrology and sediment Transport at watershed scale (In preparation).

Shuangcai Li, LifangLuo, and Keli Zhang. 2004. Simulation on effects of land use change on soil erosion on the loess plateau. Journal of Soil and Water Conservation, 18 (1): 74-77, 81.